MULTIFUNCTIONAL OPTOMECHANICAL DYNAMICS IN INTEGRATED SILICON PHOTONICS

A DISSERTATION

SUBMITTED TO THE FACULTY OF

UNIVERSITY OF MINNESOTA

BY

HUAN LI

IN PARTIAL FULFILLMENT OF THE REQUIREMENTS

FOR THE DEGREE OF

DOCTOR OF PHILOSOPHY

MO LI

FEBRUARY, 2015

Acknowledgements

Why does the section of Acknowledgements appear at the very beginning in a doctoral dissertation, which is supposed to focus on objective research? I had never seriously thought about this question until when I actually started writing this dissertation. I do not intend to do rigorous research to trace back to the first doctoral dissertation that adopted this convention and find out why. Nevertheless, from what I feel when reading others' Acknowledgements and writing my own, I believe this special section, along with the Dedication that immediately follows, reminds both the authors and readers to back off from the objective research for a moment and instead focus on the vivid humans that are involved in the research, either directly or indirectly. Furthermore, writing Acknowledgements is a good chance for an emotional wrap-up (before the technical one) because the authors have to look all the way back to the beginning of their Ph.D. years to gratefully recollect the journey between milestones.

I have been so fortunate to have a great advisor, mentor and friend – Prof. Mo Li. In retrospect, I cannot imagine how I could have accomplished anything without him. In the summer of 2010, Mo started his new group in U of M with only two students and I was fortunate enough to be one of them. Back then, other than my enthusiasm, I knew very little about silicon photonics and NOMS, while Mo was a fresh and ambitious assistant professor, with abundant invaluable novel ideas, knowledge and hands-on experience in this new research field. Thanks to him, my Ph.D. research has been so exciting and

rewarding. Mo provided the opportunities for me to walk through every single step in the entire cycle of research workflow, including literature research, theoretical derivation, simulation, fabrication recipe development, device fabrication, experiment design, lab setup, device measurement, data analysis, publication, presentation and even advising. I had this wonderful feeling that I had always been learning new knowledge and skills, meeting and overcoming new challenges.

I was also so fortunate to have the opportunity to assist Prof. James Leger and Prof. Anand Gopinath to teach the undergraduate course – Signals and Systems. I have learned a lot from them and gained invaluable teaching experience. Much more than that, although I only worked with them for one semester, they have always been a great source of advice and strong support for me ever since, which I sincerely appreciate and can never thank them enough for.

I am also very grateful to Prof. Sang-Hyun Oh and Prof. Heiko Jacobs for their advice and support at the early stage of my Ph.D. studies. Actually, it was Prof. Oh that first suggested me to inquire Mo about research positions, and recommended me to Mo. Prof. Oh turned out to be the perfect "match maker".

I would like to thank Prof. James Leger (again), Prof. Rusen Yang, Prof. Joey Talghader, Prof. Murti Salapaka and Prof. Sang-Hyun Oh (again) for their time and effort serving as committee members of my preliminary and/or final oral exams.

I would like to thank Prof. Steven Koester for the collaborative work on graphene photonics. Although this work is out of the scope of this dissertation hence is not included

here, it was great experience to work with and learn from him, who is an expert researcher on semiconductor material and device.

I would like to thank all my colleagues (including but not limited to all of our group members) for their selfless support, inspiring discussions and efficient collaborative work. I am especially obliged to Dr. Yu Chen, Dr. Jong Wook Noh, Yoska Anugrah, Dr. Nathan Lindquist and Dr. Antoine Lesuffleur.

I would like to thank Director of Graduate Studies, Prof. Randall Victora and Graduate Advisor, Linda Jagerson for their help and support on my successful application for the Doctoral Dissertation Fellowship. Linda was of great help in the revision of my research statement for the application.

I would like to thank Communications Specialist and Undergraduate Advisor Roopa Sukumaran-Berzins for her enormous help in the revision of my manuscript "Playing with a nanoscale see-saw" for the journal of Nature Nanotechnology. She did a wonderful job when she was also hectic with advising undergraduate students as the semester began. She made the manuscript a much better one. I was very much impressed and grateful.

I would like to thank Computer Support Carlos Soria, Chimai Nguyen and Dale Swanson, and Building Manager Jim Aufderhar for all their help and support in our offices and labs, the excellent staff in the Minnesota Nano Center for their essential effort to support our nano-fabrication needs, Ryan Wyse and Andrew Gustafson from Minnesota

Supercomputing Institute for their tireless effort to support my numerical simulations, and ECE Depot Coordinator Dan Dobrick for all his help and funny jokes.

Furthermore, I wish to thank all the professors, teachers and anyone who have passed on to me their knowledge, experience and philosophy in my life. What they have given me are invaluable assets of the entire human society, which I feel responsible to pass on.

Finally, I wish to express my gratitude to those who have made indispensable contributions to my research in various indirect ways. I have really enjoyed the fun with all my friends and appreciated the help and support from them and the local churches. I must thank my wife for taking care of all the mundane housework and lightening my life every day. I also owe my deep appreciations to Mr. Chuyuan Mao, who has been a great mentor and friend for life since my childhood. Over the years, my family, especially my mother, have gone through great difficulties in life and made many sacrifices to unconditionally support me. Without their support and inspiration, I could not have gone nearly as far. Thank you again.

Dedication

This dissertation is dedicated to my family, especially my mother, and also Mr. Chuyuan Mao.

Abstract

Light can generate forces on matter. The nature of these forces is electromagnetic force, or Lorentz force. The emergence and rapid progress of nanotechnology provided an unprecedented platform where the very feeble optical forces began to play significant roles. The interactions between light and matter in nanoscale has been the focus of almost a decade of active theoretical and experimental investigations, which are still ongoing and constitute a whole new burgeoning branch of nanotechnology, nano-optomechanical systems (NOMS).

In such context, the general goal of my research is to generate, enhance and control optical forces on silicon photonics platforms, with a focus on developing new functionalities and demonstrating novel effects, which will potentially lead to a new class of silicon photonic devices for a broad spectrum of applications.

In this dissertation, the concept of optical force and the general background of the NOMS research area are first introduced. The general goal of the silicon photonics research area and the research presented in this dissertation is then described. Subsequently, the fundamental theory for optical force is summarized. The different methods to calculate optical forces are enumerated and briefly reviewed.

Integrated hybrid plasmonic waveguide (HPWG) devices have been successfully fabricated and the enhanced optical forces experimentally measured for the first time. All-optical amplification of RF signals has been successfully demonstrated. The optical force

generated by one laser is used to mechanically change the optical path and hence the output power of another laser. In addition, completely optically tunable mechanical nonlinear behavior has been demonstrated for the first time and systematically studied. Optomechanical photon shuttling between photonic cavities has been demonstrated with a "photon see-saw" device. This photon see-saw is a novel multicavity optomechanical device which consists of two photonic crystal nanocavities, one on each side of it. Pumping photons into one cavity excites torsional optomechanical self-oscillation, which shuttles photons to the other empty cavity during every oscillation cycle in a well-regulated fashion.

Last but not least, the effort made to develop reliable fabrication processes for NOMS devices is summarized.

Table of Contents

Acknowledgements i

Dedication v

Abstract vi

Table of Contents viii

List of Tables xiii

List of Figures xiv

Chapter 1. Introduction 1

1.1. Optical Force 1

1.2. Background of the NOMS Research Area 1

1.3. NOMS on Silicon Photonics Platforms 5

1.4. Dissertation Outline and Collaborative Work 6

Chapter 2. Optical Force Theory 9

2.1. Direct Calculation Methods 10

2.2. Momentum Methods 11

2.3. Energy Methods 12

Chapter 3. Enhanced Optical Forces in Integrated Hybrid Plasmonic Waveguides [35] 14

3.1. Introduction 14

3.2. Device structure and theoretical analysis 17

3.2.1. Hybrid plasmonic modes (HPM) and their optical force 18

3.2.2. Multimode vibrational theory for doubly clamped beam (DCB) 24

3.2.3. Frequency response of the Si beam driven by optical force 27

3.3. Device fabrication 29

3.4. Optical characteristics 31

3.5. Optomechanical characteristics 33

3.5.1. Transduction gain factor calibration by thermomechanical noise measurement 33

3.5.2. Optical force measurement by driven response 34

3.6. Conclusion and discussion 37

Chapter 4. Multichannel Cavity Optomechanics for All-Optical Amplification of Radio Frequency Signals [34] 38

4.1. Introduction 39

4.2. Multichannel Design of a Cavity Optomechanical Device 41

4.3. Controllable Optomechanical Nonlinearity 46

4.4. Optomechanical Signal Amplification 50

4.5. Device Fabrication and Measurement Scheme 54

4.6. Theoretical Analysis of Nonlinear Optical Force 56

4.7. Theoretical Analysis of Tunable Duffing Nonlinearity 62

4.8. Calibration of Displacement Measurement 65

4.9. Cantilevered Signal Waveguide Design 69

4.10. Experimental Calibration of g Factor 71

4.11. Theoretical Calculation of g Factor 72

Chapter 5. Optomechanical Photon Shuttling Between Photonic Cavities [29] 75

5.1. Introduction 75

5.2. Photon See-Saw Oscillator 78

5.3. Impulse Response Experiment 82

5.4. Dynamics of the Cavity Resonance Frequencies During Oscillation 85

5.5. Photon Shuttling Experiment 88

5.6. Temporal Coupled Mode Theory of Two Coupled Photonic Crystal Cavities .. 93

5.7. Cavity Optomechanical Coupling 98

5.8. Photonic Crystal Nanobeam Cavity Design 100

5.9. Mechanical Modes of the Photonic Crystal Nanobeam 100

5.10. Special Precautions for the Wet Etch Releasing Process 101

5.11. Scanning Electron Microscope (SEM) Observations of the Suspended Structures 102

5.12. Transmission Spectrum Measurement and Determination of Cavity Parameters 104

5.13. Main Experimental Setup 106

5.14. Thermomechanical Noise and Cavity Optomechanical Dynamical Backaction Experiments 107

5.15. Impulse Response Experiment (More Details) 108

5.16. Dynamics of the Cavity Resonance Frequencies During Oscillation (More Details) 112

5.17. Photon Shuttling Experiment (More Details) 118

Chapter 6. Fabrication Process Development 121

6.1. Silicon Structure Fabrication 122

6.2. Silicon Structure Releasing 126

Chapter 7. Conclusion 134

Bibliography 136

Appendix A. EBL and Dry Etching Processes 148

Appendix B. Photolithography and Wet Etching Processes 151

List of Tables

Table 3.1. Definitions of the terms of optical forces. 21

Table 4.1. Parameters used to calculate the theoretical values. 60

Table 4.2. Parameters used to calculate the theoretical values. 72

Table 5.1. Summary of the mechanical modes. 101

Table 5.2. Summary of the cavity parameters. 105

Table 5.3. Summary of the optomechanical parameters. 115

Table 6.1. Calibrated measurement results by SEM imaging. 125

Table 6.2. Comparison of the pros and cons of the etchants for SiO2 substrate. 127

List of Figures

Fig. 3.1. HPWG structure and optical modes. 18

Fig. 3.2. 2D FDTD simulation of the mode evolution between fundamental TE SWM and HPM. 19

Fig. 3.3. HPWG local optical force and mechanical properties. 21

Fig. 3.4. Optical force comparison. 22

Fig. 3.5. Fabrication process diagram of the HPWG device. 29

Fig. 3.6. Images of the fabricated HPWG device. 30

Fig. 3.7. Optical characteristics of the fabricated HPWGs. 32

Fig. 3.8. Optomechanical measurements of the HPWG. 35

Fig. 4.1. A multichannel cavity optomechanical device. 41

Fig. 4.2. Transmission spectra of the device. 42

Fig. 4.3. Optical force and optical spring effect. 45

Fig. 4.4. Controllable optomechanical nonlinearity. (Part 1.) 48

Fig. 4.5. Controllable optomechanical nonlinearity. (Part 2.) 50

Fig. 4.6. All-optical signal amplification and wavelength multiplexing. (Part 1.) 51

Fig. 4.7. All-optical signal amplification and wavelength multiplexing. (Part 2.) 53

Fig. 4.8. Schematic of the measurement setup. 55

Fig. 4.9. Optical microscope image of the device measured in the experiment. 56

Fig. 4.10. Coordinate system defined in the theoretical calculation. 57

Fig. 4.11. Nonlinear behavior of the optical force. 59

Fig. 4.12. Static optical force and optical spring constant. 61

Fig. 4.13. Quadratic and cubic nonlinear coefficients. 63

Fig. 4.14. Transmission and displacement noise PSD. 66

Fig. 4.15. Time-domain traces of the transmitted signal in the signal waveguide. 68

Fig. 4.16. FDTD simulation results for the cantilevered signal waveguide design. 70

Fig. 5.1. Photon see-saw oscillator. 77

Fig. 5.2. Photonic crystal cavity simulation results. 79

Fig. 5.3. Transmission spectra of the two cavities. 81

Fig. 5.4. Impulse response and photon see-saw effect. (Part 1.) 82

Fig. 5.5. Impulse response and photon see-saw effect. (Part 2.) 84

Fig. 5.6. Time-domain traces of the probe laser transmission. 86

Fig. 5.7. Stroboscopic snapshots of the cavity resonances. 87

Fig. 5.8. The resonance frequencies of the two cavities. 88

Fig. 5.9. Optomechanical photon shuttling between two cavities. (Part 1.) 89

Fig. 5.10. Optomechanical photon shuttling between two cavities. (Part 2.) 90

Fig. 5.11. Temporal coupled mode theory model for our device. 93

Fig. 5.12. SEM images of the suspended structures. 103

Fig. 5.13. Main experimental setup. 106

Fig. 5.14. Standard cavity optomechanical experiments. 107

Fig. 5.15. Waveforms of the pump pulse. 109

Fig. 5.16. FEM simulation results for the impulse response contributed by the temperature rise and thermo-optic effect of silicon. 111

Fig. 5.17. Supplementary time-domain traces pertaining to the dynamics of the cavity resonance frequencies during oscillation. 114

Fig. 5.18. The dynamics of cavity resonance..... 117

Fig. 6.1. SEM images of the grating coupler on the dose test sample. 123

Fig. 6.2. SEM images of the photonic crystal slab on the dose test sample. 124

Fig. 6.3. SEM images of the dry etched sidewalls. 126

Fig. 6.4. SEM images of the defective released devices..... 127

Fig. 6.5. SEM image of typical released torsional optomechanical devices..... 132

Fig. 6.6. SEM image of typical released torsional optomechanical devices..... 133

Fig. 6.7. SEM image of typical released torsional optomechanical devices..... 133

Chapter 1. Introduction

1.1. Optical Force

Light can generate forces on matter. The nature of these forces is electromagnetic force, or Lorentz force. They originate from the forces exerted on the charges (electrons and nuclei) that constitute the matter by the electric and magnetic fields in light. Optical forces may manifest themselves in drastically different ways, including (but not limited to) pushing, pulling, squeezing or expanding, determined by the particular interactions between light and matter. Consequently, in different contexts and situations, different terminologies for optical forces are used, including gradient force, optical dipole force, and, perhaps the most commonly known, radiation pressure.

1.2. Background of the NOMS Research Area

Although the first conception of radiation pressure dates back to as early as 1619, when Johannes Kepler attempted to explain the observation that a tail of a comet always points away from the sun [1], it was not until late 1980s that optical force found its first remarkable and widespread application – optical tweezers [2]. Experimentally demonstrated and reported by A. Ashkin et al. in 1986 for the first time [3], optical tweezers use optical forces to trap and manipulate biological cells or mesoscale particles micron or nanometer sized. From then on, the emergence and rapid progress of nanotechnology provided an unprecedented platform where the very feeble optical forces began to play significant roles.

On one hand, nanoscale structures can be engineered to tightly confine light near or below the diffraction limit, which greatly enhances the light field, hence the optical force. On the other hand, nanoscale objects possess small mass and generally low structural rigidity, therefore can be easily moved or deformed by the optical forces. Conversely, the motion or deformation of these nanoscale objects can change the propagation and/or frequency of light.

In 2005, the interactions between the light field inside a Fabry-Perot (F-P) cavity and a movable cavity mirror predicted in V. B. Braginsky et al.'s theoretical work [4], [5] were experimentally observed and reported for the first time by T. J. Kippenberg et al. [6], [7]. Instead of an F-P cavity, this experiment was conducted with a micro-toroid ultrahigh quality factor (Q) optical cavity accessed by a fiber taper, which turned out to be an excellent experimental platform for cavity optomechanics [8]–[10]. The circulating light field inside the micro-toroid cavity exerts distributed optical force that tends to expand the toroid. The resonance frequency of the micro-toroid cavity red-shifts when the circumference of the toroid increases, leading to change of the intracavity light field. Due to the ultrahigh resonator Q, the change of the intracavity light field, hence that of the optical force, is delayed from the mechanical deformation. These dynamical interactions [9] modify the effective spring constant and damping coefficient of the mechanical mode, resulting in intriguing phenomena such as optical spring and optomechanical heating (also known as amplification) [7] and cooling [11], [12] of the Brownian motion.

The aforementioned breakthrough was followed immediately by almost a decade of active theoretical and experimental investigations up to now, which are still ongoing and constitute a whole new burgeoning branch of nanotechnology, nano-optomechanical systems (NOMS). Although the research scope of NOMS is now much wider than that of cavity optomechanics, the latter has always been the most important part of NOMS so far. The major experimental milestones in the development of NOMS should include the following, sorted by the time of their publication in peer reviewed journals.

In 2005 and 2006, cavity optomechanical heating (or amplification) and cooling were demonstrated, respectively, in silica micro-toroid optical cavities [7], [11]. Also in 2006, the same phenomena were demonstrated in an F-P cavity with a microscale movable mirror [13], [14].

In 2008, two more NOMS experimental platforms were proposed and implemented. One is a high-finesse optical F-P cavity with a silicon nitride micromechanical membrane inside, which is parallel to the cavity mirrors and of nanoscale thickness [15]. The other is nanoscale suspended silicon photonics waveguides fabricated on silicon on insulator (SOI) wafers [16]. The former platform is implemented with high quality free-space optics, while the latter is completely integrated on a SOI chip.

In 2009, three more NOMS experimental platforms were proposed and implemented. One is the "zipper" cavities, which consist of a pair of specially patterned nanoscale silicon beams to support co-localized photon and phonon modes that realize large per-photon optical forces [17]. Another is optomechanical crystals, which are one-

dimensional (1D) nanoscale periodic suspended silicon structures, whose photonic and phononic band gaps and defects are engineered to support co-localized photon and phonon modes that strongly interact [18]. The third is vertically stacked silicon nitride double disk resonators, whose optical response can be efficiently statically controlled using attractive and repulsive optical forces [19].

In 2009, tunable attractive and repulsive optical forces exerted on two coupled parallel nanoscale optical waveguides were demonstrated on an integrated silicon photonics platform [20].

In 2010, the tunable nonlinear optomechanical coupling in a low-loss system, which consists of an F-P cavity with a membrane of nanoscale thickness inside, was systematically explored [21].

In 2010 and 2011, optomechanically induced transparency (OMIT) was demonstrated with a micro-toroid [22] and an optomechanical crystal [23], respectively.

In 2011, laser cooling of a nanomechanical oscillator into its quantum ground state was achieved in an optomechanical crystal device [12].

In 2011, a non-volatile mechanical memory element fully integrated on an SOI chip was demonstrated, in which bits are written and reset by using optomechanical backaction [24]. The bistability (buckling up or buckling down) of a suspended silicon nano-beam with compressive stress is used to represent “0” or “1”.

In 2012, optomechanical synchronization of two dissimilar vertically stacked silicon nitride double disk oscillators was demonstrated. The two oscillators are coupled through optical cavity field [25].

In 2012, quantum-coherent coupling of a mechanical oscillator to an optical cavity mode was achieved in a micro-toroid cavity optomechanical system [26].

In 2013, squeezed light from a silicon micromechanical resonator was demonstrated with the "zipper" cavity [27].

In 2014, optically mediated hybridization between two mechanical modes was demonstrated in an F-P cavity with a membrane of nanoscale thickness inside [28].

In 2014, optomechanical photon shuttling between photonic cavities was demonstrated with a "photon see-saw" device fully integrated on an SOI chip [29]. (This work is part of this dissertation.)

1.3. NOMS on Silicon Photonics Platforms

One of the many prongs of the aforementioned NOMS research effort is to integrate NOMS on silicon photonics platforms [16], [20], [24]. The general goal of silicon photonics [30]–[33] is to "siliconize photonics", or in other words, to implement photonics components, circuits and functionalities on an integrated silicon platform, in a manner similar to silicon electronics. Typically, SOI wafers with thick (3 μm) buried oxide (BOX) layer and mid-inferred light (1550 nm wavelength) are used. The top silicon layer can be patterned into photonics components and circuits including waveguides, resonators, photonics crystals,

grating couplers, etc., while the BOX layer functions as a cladding layer. The combination of NOMS and silicon photonics benefits from the years of accumulated knowledge and experience of silicon photonics device design, fabrication and characterization. Also, the integrated nature of silicon photonics is desirable for potential future commercialization. Meanwhile, the NOMS holds great promise for bringing new functionalities to conventional silicon photonics.

In such context, the general goal of my research is to generate, enhance and control optical forces on silicon photonics platforms, with a focus on developing new functionalities and demonstrating novel effects, which will potentially lead to a new class of silicon photonic devices for a broad spectrum of applications.

1.4. Dissertation Outline and Collaborative Work

In Chapter 1, the concept of optical force and the general background of the NOMS research area are first introduced. The general goal of the silicon photonics research area and the research presented in this dissertation is then described.

Subsequently, in Chapter 2, the fundamental theory for optical force is summarized. The different methods to calculate optical forces are enumerated and briefly reviewed.

What follows the introduction and the theory review is the revised compilation of the author's selected published research work [29], [34], [35].

In 2013, integrated hybrid plasmonic waveguide (HPWG) devices have been successfully fabricated and the enhanced optical forces experimentally measured for the

first time [35]. When light interacts with metal in close proximity, the generated optical forces are enhanced by 1 or 2 orders of magnitude, compared with the cases where no metal is present. This work is presented in Chapter 3. Jong Wook Noh and Yu Chen made major contributions to the fabrication of the integrated HPWG devices used here.

In 2012, all-optical amplification of RF signals has been successfully demonstrated [34]. The optical force generated by one laser is used to mechanically change the optical path and hence the output power of another laser. In addition, completely optically tunable mechanical nonlinear behavior has been demonstrated for the first time and systematically studied. This work is presented in Chapter 4. Jong Wook Noh and Yu Chen made major contributions to the fabrication of the multichannel micro-disk devices used here. Semere Ayalew Tadesse contributed to the numerical modeling.

In 2014, optomechanical photon shuttling between photonic cavities has been demonstrated with a "photon see-saw" device [29]. This photon see-saw is a novel multicavity optomechanical device which consists of two photonic crystal nanocavities, one on each side of it. Pumping photons into one cavity excites torsional optomechanical self-oscillation, which shuttles photons to the other empty cavity during every oscillation cycle in a well-regulated fashion. This work is presented in Chapter 5.

Last but not least, the effort made to develop reliable fabrication processes for NOMS devices is summarized in Chapter 6, including Appendix A and Appendix B. The various considerations and requirements of this fabrication process development are briefly reviewed. Different fabrication process options are presented and compared.

Finally, the research presented in the entire dissertation is summarized and the future perspectives are discussed in Chapter 7.

Chapter 2. Optical Force Theory

Light can generate forces on matter. The nature of these forces is electromagnetic force, or Lorentz force. They originate from the forces exerted on the charges (electrons and nuclei) that constitute the matter by the electric and magnetic fields in light. Optical forces may manifest themselves in drastically different ways, including (but not limited to) pushing, pulling, squeezing or expanding, determined by the particular interactions between light and matter. Consequently, in different contexts and situations, different terminologies for optical forces are used, including gradient force, optical dipole force, and, perhaps the most commonly known, radiation pressure.

To calculate any force, there are in general three methods – calculating the force directly, calculating the time derivative of momentum and calculating the space derivative of energy (or work). All these three methods apply to optical force calculations. Within each method, light can be modeled in quantum mechanical approaches, as photons, or in classical approaches, as electromagnetic waves. In certain cases semi-classical approaches may also be used.

Before the methods of optical force calculations are briefly reviewed, it is worth emphasizing that, to obtain correct and meaningful results, caution must be exercised when using any of the following methods. The applicability and subtle implications of the methods must be carefully checked. Microscopic and macroscopic quantities, such as charge, current, fields sometimes need to be clearly differentiated. Any medium that is

anisotropic, inhomogeneous, lossy or dispersive may need special treatment. Calculations of the electromagnetic field momentum inside medium, the optical force distribution inside medium, or the total optical force exerted on a partial volume of medium, may lead to ambiguous results. The readers will be referred to dedicated literature for more details.

2.1. Direct Calculation Methods

When calculating optical forces directly, the expression for Lorentz force density [36] should be used and light is modeled as electromagnetic waves.

$$\mathbf{f}^{\mathrm{L}} = \rho\mathbf{E} + \mathbf{J} \times \mathbf{B} \tag{2.1}$$

Oftentimes the charge density and current density are further expressed in terms of electric and magnetic fields according to Maxwell's equations, leading to the following two distinct expressions for the force density [36], [37].

$$\mathbf{f}^{\mathrm{c}} = -\left(\nabla \cdot \mathbf{P}\right)\mathbf{E} + \dot{\mathbf{P}} \times \mathbf{B} \tag{2.2}$$

$$\mathbf{f}^{\mathrm{d}} = \left(\mathbf{P} \cdot \nabla\right)\mathbf{E} + \dot{\mathbf{P}} \times \mathbf{B} \tag{2.3}$$

Generally, the electric and magnetic fields of the light inside the medium volume of interest should be calculated first before Eq. (2.1), Eq. (2.2) or Eq. (2.3) is used to calculate the optical force density. The total optical force is the integration of the force density over the medium volume of interest. For more details and subtleties the readers are referred to the following literature [36]–[39].

2.2. Momentum Methods

When calculating optical forces as the time derivative of light momentum, light can be modeled as photons or electromagnetic waves. In either case, the total optical force should be calculated from the net momentum flow into a closed surface that surrounds the medium volume of interest.

Generally, for simple cases concerning only monochromatic plane waves in vacuum, reflected or absorbed by a flat surface, it is very convenient and intuitive to model light as photons, the momentum carried by each of which is h/λ, according to the de Broglie relations.

For more complicated cases, it is more convenient to model light as electromagnetic waves that carry momentum. In practice, Maxwell's stress tensor [40] $\mathbf{T}$ defined in Eq. (2.4) is often used to quantify the linear momentum flux (rate of flow of momentum per unit area) of electromagnetic waves.

$$T_{ij} = \varepsilon_0 \left[E_i E_j + c^2 B_i B_j - \frac{1}{2} \delta_{ij} \left(\mathbf{E} \cdot \mathbf{E} + c^2 \mathbf{B} \cdot \mathbf{B} \right) \right] \tag{2.4}$$

The total optical force can be found by the integration of the normal component of $\mathbf{T}$ over the closed surface that surrounds the medium volume of interest.

$$\mathbf{F} = \oint_S \mathbf{n} \cdot \mathbf{T} da \tag{2.5}$$

For more details and subtleties, especially about the momentum of light in medium, the readers are referred to the following literature [40]–[43].

2.3. Energy Methods

When calculating optical forces as the space derivative of light energy (or the work done by the light), closed systems and open systems need to be treated differently.

The simpler case is the closed systems, which in this context means a perfect cavity where light is forever trapped inside. Light is conveniently modeled as photons. Assume that the cavity, whose angular resonance frequency is ω_0, very slowly undergoes an infinitesimal mechanical displacement along a generalized coordinate q. Due to the optical force exerted on the cavity, photons inside the cavity do work and their energy (hence frequency) changes according to the shift of the cavity angular resonance frequency. Therefore the optical force along the same generalized coordinate q satisfies Eq. (2.6), where U is the total photon energy and N is the total photon number.

$$F_q(q) = -\frac{dU}{dq} = -N\hbar\frac{d\omega_0(q)}{dq} \tag{2.6}$$

This conclusion is generally a very good approximation for any real-world high quality cavities excited on or near resonance. However, many real-world NOMS devices cannot be approximated as closed systems and have to be treated as open systems, which light can flow into and out of. In this case, the Response Theory of Optical Forces (RTOF) [44] should be used. RTOF is a semi-classical approach that relates the work done by the photons transiently stored in the system to the phase changes of the light waves, when the system very slowly undergoes an infinitesimal mechanical displacement along a generalized coordinate q. For a lossless one-port system driven at a single frequency, the

optical force along the generalized coordinate q satisfies Eq. (2.7), where Φ is the photon flux (rate of flow of photon number) and ϕ is the phase of the output light wave. For more details and subtleties the readers are referred to the following literature [44], [45].

$$F_q(q) = \Phi\hbar\frac{d\phi(q)}{dq} \tag{2.7}$$

Chapter 3. Enhanced Optical Forces in Integrated Hybrid Plasmonic Waveguides [35]

We demonstrate gradient optical forces in metal-dielectric hybrid plasmonic waveguides (HPWG) for the first time. The magnitude of optical force is quantified through excitation of the nanomechanical vibration of the suspended waveguides. Integrated Mach-Zehnder interferometry is utilized to transduce the mechanical motion and characterize the propagation loss of the HPWG. Compared with theory, the experimental results have confirmed the optical force enhancement, but also suggested a significantly higher optical loss in HPWG. The excessive loss is attributed to metal surface roughness and other non-idealities in the device fabrication process.

3.1. Introduction

Nano-optomechanical system, or NOMS, is a burgeoning field that combines nanophotonic and nano-electromechanical (NEMS) devices seamlessly in an integrated system [9], [16], [17], [19], [46]. By utilizing near-field optical forces generated in nanophotonic structures, NOMS exploits the interaction between the mechanical degrees of freedom in NEMS and the optical functionalities of photonic devices. For fundamental research, the optomechanical effects represent a new form of light-matter interaction that can be rationally engineered in nanophotonic systems, leading to many unprecedented physical

phenomena in both classical and quantum regimes [11], [47], [48]. For practical applications, NOMS enables ultrahigh measurement sensitivity in NEMS-based sensors [19], [46], [49], [50], opens up new possibilities to implement non-volatile mechanical memory operation [24], all-optical signal processing [34], tunable or reconfigurable optical circuits [51], and potentially brings even more novel device functionalities to nanophotonics.

During the past a few years, significant advances have been made in NOMS devices based on all-dielectric nanophotonic systems, such as those implemented with silicon [16], [20], [24], [34], [51], silica [26], [46], silicon nitride [17], [19], [51] or aluminum nitride [52]. In the meantime, optical forces and optomechanical effects in another important category of nanophotonic devices, namely plasmonics [53], [54], have become a new research focus which has been under active theoretical investigation [55]–[57]. Nevertheless, few relevant experimental studies [58], [59] have been published so far, primarily due to the challenges in the device fabrication and experimental characterization.

Theoretical analysis based on energy conservation and closed or open system assumptions [44], [60], [61] both lead to a simplified and generalized expression of the optical forces that can be applied to all kinds of nanophotonic structures consisting of linear and lossless media:

$$f_{\mathrm{o}}\left(\omega_{\mathrm{o}}, q\right) = \frac{1}{c} \frac{\partial \operatorname{Re}\left[n_{\mathrm{eff}}\left(\omega_{\mathrm{o}}, q\right)\right]}{\partial q}. \tag{3.1}$$

Although Eq. (3.1) does not take into account of loss, it is nevertheless a good approximation for systems with low loss. Here f_o is the optical force per unit length normalized to the optical power, ω_o is the optical angular frequency, q is a generalized coordinate corresponding to the mechanical degree of freedom that is under consideration, $n_{eff}(\omega_o,q)$ is the effective index of optical mode and c is the speed of light in vacuum. This expression reveals that any dispersive dependence of n_{eff} on a positional coordinate (q) corresponds to an optical force along that coordinate direction. The stronger the dependence (i.e. $\partial n_{eff}/\partial q$), the larger the corresponding optical force is. Such a position dependence of optical mode index can be found in almost all nanophotonic structures—generally their optical modal profile are sensitive to mechanical displacement or deformation. Therefore, the existence of optical forces is ubiquitous in photonic systems. This is more the case in nanophotonic devices because the optical fields therein interact and couple more strongly in the near-field, in a way highly dependent on the distance between the coupled structures. This implies the existence of strong optical forces at the nanoscale. With this fundamental understanding of its mechanism, optical forces and optomechanical effects can be effectively generated in many nanophotonic systems, including both dielectric and metallic plasmonic devices, as well as the hybrids of them.

In this work we experimentally demonstrate optical forces in integrated metal-dielectric hybrid plasmonic waveguides (HPWG), which is one of the most widely investigated plasmonic structures [55], [57], [58], [62]. As far as we are aware of, this is the first experimental characterization of optical forces in HPWG. Compared with all-

metallic surface plasma polariton waveguides and all-dielectric waveguides, their hybrids, HPWG, exhibits lower loss than the former [58], [62] and deeper sub-wavelength optical mode confinement than the latter, which leads to optical forces that are enhanced by an order of magnitude or more [55], [57]. This enhanced optical force has been experimentally confirmed and quantified in this work. The propagation loss in HPWG, however, is significantly higher than theoretical expectations, as a result of the roughness of metal surfaces [63] and other non-idealities in the fabrication processes. Nevertheless, many fabrication methods [63]–[65] have been reported to achieve ultra-smooth metal surfaces and they can be applied in HPWG to reduce scattering loss. Thus, the plasmonic optomechanical systems demonstrated here have a great potential in leading to optical force mediated adaptive photonic devices and sensors.

3.2. Device structure and theoretical analysis

The HPWG structure employed in this work is shown schematically in Fig. 3.1a. On a standard silicon-on-insulator (SOI) substrate, a metal patch is placed in parallel with a strip Si waveguide of equal thickness. The gap between the metal patch and the Si strip is less than 100 nm. A section of the Si waveguide is suspended by removing the SiO_2 layer underneath and is free to move in-plane. The optical, mechanical and optomechanical properties of this HPWG structure will be theoretically analyzed in this section.

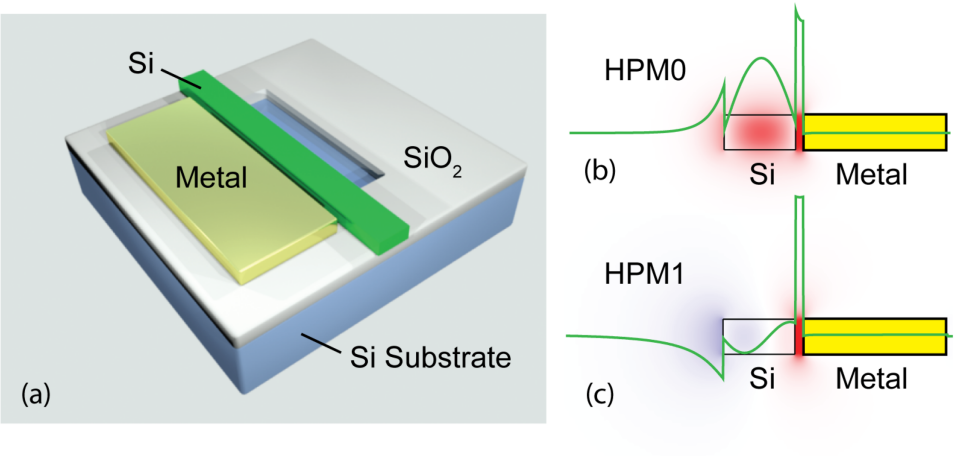

Fig. 3.1. HPWG structure and optical modes.

(a) HPWG structure illustration. (b) and (c) Transverse electric field component of the HPM0 and HPM1, respectively, with the overlaid green curves showing the cross-sectional profile of the transverse electric field.

3.2.1. Hybrid plasmonic modes (HPM) and their optical force

In this structure, the transverse electric (TE) optical modes, with electric field predominantly in the plane of Si waveguide and metal patch, exhibit the features of both the Si waveguide mode (SWM) and the surface plasma polariton mode, hence the name "hybrid plasmonic mode" (HPM).

The fundamental (or zeroth order) and first order TE modes of the HPWG (HPM0 and HPM1) are simulated with finite element method (FEM) and shown in Fig. 3.1b and Fig. 3.1c, respectively. Here the Si waveguide is 450 nm wide. Both the Si waveguide and the metal are 220 nm thick. The gap between them is 50 nm wide. The vacuum optical wavelength is 1550 nm. The refractive indices used for Si and metal (gold) are 3.45 and

0.524+10.742*i* [66], respectively. The simulation results clearly show the strongly enhanced transverse electric field in the gap region, compared with the field in the silicon waveguide. For a given HPWG thickness, the number of HPMs supported is primarily determined by the width of the Si waveguide. In the case of 220 nm thickness, when the Si waveguide is narrower than 350 nm, only HPM0 can be supported. If the Si waveguide is wider than 450 nm, second or higher order HPMs can also be supported. However, in the devices fabricated in the present experimental work, only the fundamental mode is excited, due to the following two reasons. First, the Si waveguides we fabricated are no more than 450 nm wide so second or higher order HPMs are not supported. Second, in our devices,

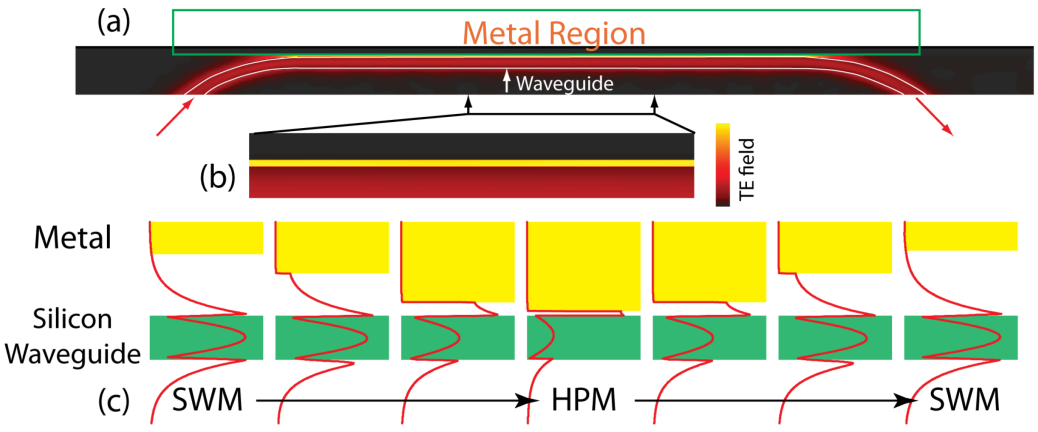

Fig. 3.2. 2D FDTD simulation of the mode evolution between fundamental TE SWM and HPM.

(a) The overview of the simulated HPWG structure overlaid by the transverse electric field component. The red arrows indicate where the SWM enters and exits. (b) A close-up view of the enhanced transverse electric field component in the nano gap. (c) Mode evolution from SWM to HPM, and then back to SWM again. The red curves show the cross sections of the transverse electric field component in the evolving mode.

HPMs are excited by launching the fundamental TE mode of silicon waveguide (TE SWM) into the hybrid region, as shown in Fig. 3.2a. Compared with the HPM0, the HPM1 has a negligible mode overlap with the fundamental TE SWM. Therefore the coupling efficiency for the HPM1 is negligibly small compared with that for the HPM0.

This qualitative analysis on mode evolution between SWM and HPM has been confirmed by 2D finite difference time domain (FDTD) simulations shown in Fig. 3.2. In this simulation, a Si slab waveguide approaches a metal wall gradually, becomes parallel with the metal wall with a nano-sized gap, and then gradually leaves the metal wall. The fundamental TE SWM enters into the Si slab waveguide on the left side, and exits from the right side. From the simulation result, it is evident that the fundamental TE SWM evolves predominantly into HPM0 only, while as expected, HPM1 cannot be excited. Although the HPWG and the silicon waveguide in practice are 3D structures, the 2D simulation shown here is sufficient to demonstrate the features of the mode evolution between them.

Because HPM is inevitably lossy due to Ohmic loss in the metal, the power of optical mode decays exponentially while propagating in HPWG: $P(x) = P(0)e^{-\alpha x}$, where x axis is defined along the HPWG, $P(x)$ is the optical power as a function of position x and α is the decay constant. Using the imaginary part of the HPM complex mode index n_{eff}, which is calculated by FEM simulation, α can be expressed as $\alpha = 2\omega_o|\text{Im}(n_{\text{eff}})|/c$.

Because the local optical force for a certain mode is always proportional to the local optical power, the lossy nature of HPWG results in exponential decay of the generated optical force $p(x)$ as the optical mode propagates, as depicted in Fig. 3.3a. (See Table 3.1

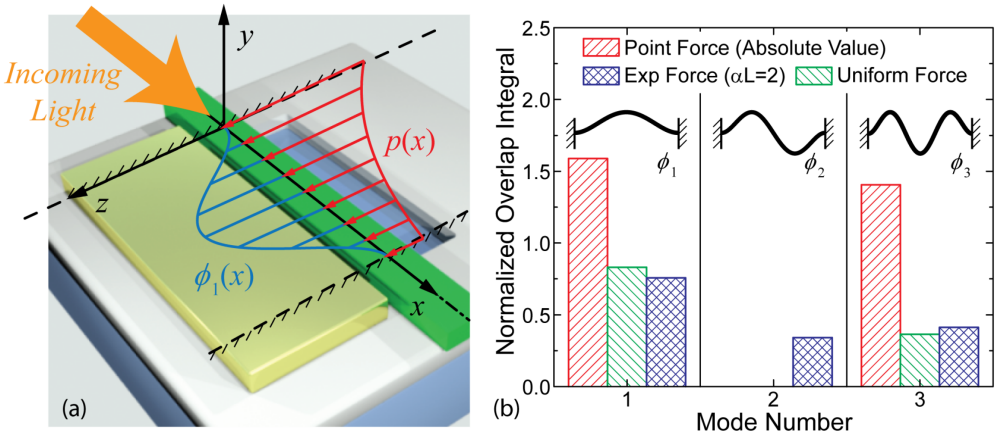

Fig. 3.3. HPWG local optical force and mechanical properties.

(a) Local optical force and beam mechanical in-plane mode profile. (b) Comparison of the excitation of the mechanical modes by different force distributions.

for definitions of symbols, which are used consistently throughout the paper.) Such exponential decay of the optical force distribution $p(x)$ leads to a nonlinear relationship between F_n, the total optical force normalized by the input optical power $P(0)$, and L, the length of HPWG, as is shown in Eq. (3.2). In contrast, in low-loss dielectric waveguide,

Table 3.1. Definitions of the terms of optical forces.

Term	Notation	Definition	Unit
Local optical force (or optical force distribution)	$p(x)$	Optical force per unit waveguide length at coordinate x.	N/m
Total optical force	F	The integral of $\|p(x)\|$ over the entire waveguide.	N
Normalized local optical force	p_n	Normalized $p(x)$ to **local** optical power $P(x)$. Independent of x.	N/(m·W)
Normalized total optical force	F_n	Normalized F to **input** optical power $P(0)$.	N/W

the normalized total optical force F_n is considered to be proportional to the waveguide length [44], [60], [61].

$$F_n = \frac{\int_0^L |p(x)|dx}{P(0)} = p_n \int_0^L e^{-\alpha x} dx = \frac{p_n}{\alpha}\left(1 - e^{-\alpha L}\right). \tag{3.2}$$

This difference is demonstrated in Fig. 3.4, where the dependence of F_n on the waveguide length is compared, for different waveguide structures reported in the literature [16], [20], [51], [55], [57], [60] and the HPWG in this work. Instead of Eq. (3.1), the method of Maxwell Stress Tensor (MST) [40], [43] is used to calculate the optical forces

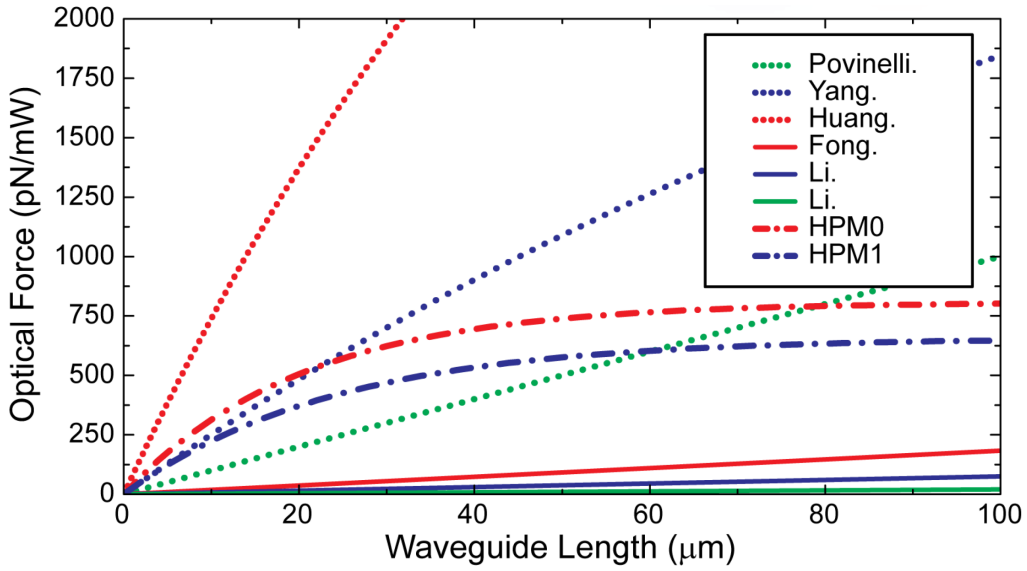

Fig. 3.4. Optical force comparison.

Comparison of the dependence of the total optical force on the waveguide length in different waveguide structures from literatures and this work. Solid lines represent experimental work while the other line styles represent theoretical calculation. Povinelli [60]. Yang [55]. Huang [57]. Fong [51]. Li (blue) [16]. Li (green) [20].

in HPWG because it is accurate even when material loss is present, although MST does not provide as much insight as Eq. (3.1) does. When plotting Fig. 3.4, for theoretical curves, the maximum optical forces reported in the corresponding literature using a gap no less than 30 nm are chosen; while for experimental curves, the maximum demonstrated optical forces in the corresponding literature are used. Because gaps less than 30 nm are quite challenging to fabricate, so we have excluded these cases in the theoretical results when comparing with the experimental results. The two curves from this work are simulation results for HPM0 and HPM1. Compared with optical forces in dielectric systems, the optical forces for HPM0 and HPM1 can be significantly stronger over a short distance, thanks to the field enhancement effect. Over a longer distance, however, the normalized total optical forces F_n for HPMs plateau while those for dielectric waveguides continue to increase linearly and eventually exceed the F_n in HPMs. Thus, HPWG is capable to generate large total optical force in a short distance and potentially advantageous for miniaturizing device footprint. For longer distance, HPWG may be too lossy to compete with dielectric waveguides in order to generate large optical forces.

For given HPWG thickness and gap width, the optical force p_n depends non-monotonically on the Si waveguide width, which has an optimum that generates the maximum force. This optimal Si waveguide width is different for different order of HPM. The HPM0 and HPM1 curves in Fig. 3.4 are calculated with 220 nm thicknesses, 30 nm gaps and their respective optimal Si waveguide widths, which are 250 nm for HPM0 and 550 nm for HPM1. It turns out that the HMP0 is the most efficient to generate large optical

force, so in our experiments, we only focused on HMP0. It is worth noting that the normalized local optical force p_n is only determined by the HPWG structure and the dispersion property of the pertinent HPM, as is described in Eq. (3.1), so it is the quantity that our experimental measurements aim to determine.

3.2.2. Multimode vibrational theory for doubly clamped beam (DCB)

The suspended Si waveguide in the HPWG structure can be modeled as a thin and long doubly clamped beam (DCB). Because the optical force distribution along the waveguide is not uniform, it is necessary to rigorously analyze the mechanical modes and the driven response of the waveguide in order to quantify the optical force. In the following, we employ the multimode theory as described in [67], [68] for such a purpose.

In absence of damping and loads and in the stress limit, where tension is negligible compared to bending rigidity, the equation of motion of the DCB is given by

$$EI\frac{\partial^4 u(x,t)}{\partial x^4}+\rho A\frac{\partial^2 u(x,t)}{\partial t^2}=0, \tag{3.3}$$

where E is the Young's Modulus, I is the cross sectional area moment of inertia with respect to the neutral axis, ρ is the density, A is the cross-sectional area, t is time, x is the axis along the waveguide and u is the DCB in-plane transverse displacement along the z axis, which is defined in Fig. 3.3a. The solution of Eq. (3.3) has the form of normal mode expansion which satisfies the doubly clamped boundary conditions:

$$u(x,t)=\sum_{j=1}^{\infty}C_j\sin\left(\omega_j t+\delta_j\right)\phi_j(x),\ \text{with} \tag{3.4}$$

$$\begin{aligned}\phi_j(x)=&\left[\sin\left(\lambda_j L\right)-\sinh\left(\lambda_j L\right)\right]\left[\cos\left(\lambda_j x\right)-\cosh\left(\lambda_j x\right)\right]\\&-\left[\sin\left(\lambda_j x\right)-\sinh\left(\lambda_j x\right)\right]\left[\cos\left(\lambda_j L\right)-\cosh\left(\lambda_j L\right)\right],\end{aligned} \tag{3.5}$$

where ω_j and $\phi_j(x)$ are the angular frequency and mode profile of the jth mechanical mode, respectively, while λ_j is a solution of

$$\cos\left(\lambda_j L\right)\cosh\left(\lambda_j L\right)=1. \tag{3.6}$$

The profile of the first order mode is shown in Fig. 3.3a in the in-plane direction. The relationship between λ_j and ω_j is given by

$$\left(\lambda_j L\right)^4=\frac{\omega_j^2\rho AL^4}{EI}. \tag{3.7}$$

In order to study the dynamics of the DCB subjected to time varying forces (including damping), the motion of the beam is expanded with the normal modes as shown in Eq. (3.8). The equation of motion for each mechanical mode is given by Eq. (3.9), where $q_j(t)$, $p_j(t)$, m_j, k_j and Q_j are the instantaneous amplitude, driving force, effective mass, spring constant and quality factor for the jth mode, respectively. The expression for $p_j(t)$ is given by Eq. (3.10), where $p(x,t)$ is the time varying force distribution. In the case of optical force excitation, $p(x,t)$ should be the time varying optical force distribution, which decays exponentially along the HPWG. The expressions for m_j and k_j in terms of the beam parameters are given by Eq. (3.11).

$$u(x,t)=\sum_{j=1}^{\infty}\phi_j(x)q_j(t). \tag{3.8}$$

$$m_j\ddot{q}_j(t)+\frac{\sqrt{k_j m_j}}{Q_j}\dot{q}_j(t)+k_j q_j(t)=p_j(t). \tag{3.9}$$

$$p_j(t)=\int_0^L p(x,t)\phi_j(x)\,dx. \tag{3.10}$$

$$m_j=\rho A\int_0^L\left(\phi_j\right)^2 dx \text{ and } k_j=EI\int_0^L\left(\phi_j''\right)^2 dx. \tag{3.11}$$

It is worth noting that Eq. (3.10) indicates that generally a certain force distribution $p(x,t)$ will excite more than one mode, unless it has the same profile as one of the normal modes $\phi_j(x)$, in which case only that single mode will be excited. Furthermore, different force distributions will excite different sets of modes and it is possible to purposely engineer the force distribution to selectively excite one or more specific modes only. In Fig. 3.3b, three typical types of force distribution—point force at the middle of the beam, uniform force and exponential decaying force (with decay constant $\alpha=2/L$)—are compared. In each case, the overlap integral in Eq. (3.10) is evaluated and normalized with Eq. (3.12) , where the results N_j are plotted. In the fraction on the right-hand side of Eq. (3.12), the first term in the denominator normalizes the force distribution $p(x,t)$ in the overlap integral to the total force, which is the integral of the absolute value of the force distribution along the entire beam. Meanwhile, the mode profile $\phi_j(x)$ in the overlap integral is normalized by the second term in the denominator.

$$N_j = \frac{p_j(t)}{\int_0^L |p(x,t)|\,dx \sqrt{\frac{1}{L}\int_0^L \phi_j^2(x)\,dx}}. \tag{3.12}$$

Due to symmetry, the point force and the uniform force only excite odd order modes, while the exponential force excites both the odd and even order modes. For the same total force, point force is much more efficient to excite higher order modes than the other two cases.

For analysis of thermomechanical noise of the DCB, application of equipartition theorem yields the Lorentzian expression of noise power spectral density (PSD) of q_j, if Q_j is high and j is not very large,

$$S_{q_j q_j}(\omega) = \frac{\frac{k_B T \omega_j}{2Q_j k_j}}{(\omega - \omega_j)^2 + \frac{\omega_j^2}{4Q_j^2}}, \tag{3.13}$$

where k_B is the Boltzmann constant and T is the temperature. The thermomechanical noise PSD is directly measurable and can be used to calibrate key parameters of the Si beam in the experiments.

3.2.3. Frequency response of the Si beam driven by optical force

When the Si beam is subject to an exponentially decaying optical force distribution, the overlap integral in Eq. (3.10) can be evaluated as

$$p_j(t) = \int_0^L p(0,t) e^{-\alpha x} \phi_j(x)\,dx = p_n P(0,t) \int_0^L e^{-\alpha x} \phi_j(x)\,dx, \tag{3.14}$$

where the time dependence of $p(x)$ and $P(x)$ is explicitly indicated. The resultant definite integral in Eq. (3.14) can be evaluated analytically with Eq. (3.15).

$$\int e^{-\alpha x}\phi_j(x)\,dx = \frac{\alpha^3\phi_j(x)+\alpha^2\phi_j'(x)+\alpha\phi_j''(x)+\phi_j'''(x)}{\lambda_j^4-\alpha^4}e^{-\alpha x}. \tag{3.15}$$

Fourier transforming both sides of Eq. (3.9) and organizing it into the form of a transfer function, we obtain the full frequency response of the Si beam:

$$H_j(\omega) = \frac{\tilde{q}_j(\omega)}{\tilde{p}_j(\omega)} = \frac{1}{-\omega^2 m_j + i\omega\dfrac{\sqrt{k_j m_j}}{Q_j} + k_j}, \tag{3.16}$$

where the sign "~" indicates the Fourier transform of the corresponding quantity and i is the imaginary unit. At the mode resonance frequency, the amplitude of the transfer function in Eq. (3.16) reaches the resonance peak, which is

$$\left|H_j(\omega_j)\right| = \frac{\left|\tilde{q}_j(\omega_j)\right|}{\left|\tilde{p}_j(\omega_j)\right|} = \frac{Q_j}{k_j}. \tag{3.17}$$

Substituting Eq. (3.14) into Eq. (3.17), we obtain the expression for normalized local optical force p_{n} shown in Eq. (3.18), which can be evaluated from experimental results, assuming Q_j is high.

$$p_{\mathrm{n}} = \frac{1}{\int_0^L e^{-\alpha x}\phi_j(x)\,dx}\frac{k_j}{Q_j}\frac{\left|\tilde{q}_j(\omega_j)\right|}{\left|\tilde{P}(0,\omega_j)\right|}. \tag{3.18}$$

3.3. Device fabrication

The fabrication process for the HPWG, which is illustrated in Fig. 3.5, begins with a standard silicon-on-insulator (SOI) wafer with a 220 nm thick top Si layer and a 3 μm thick buried oxide layer. First, a recess in the top Si layer is created by electron beam lithography (EBL) and plasma etching and filled with gold by evaporation and lift-off. In order to reduce the surface roughness of the deposited gold, this step is done with diluted electron beam resist ZEP 520 which is developed with developer solution in a cold bath [69]. Then, another step of EBL with ultrahigh alignment precision is used to define the Si waveguides. The alignment precision is critical in determining the size of the gap between the

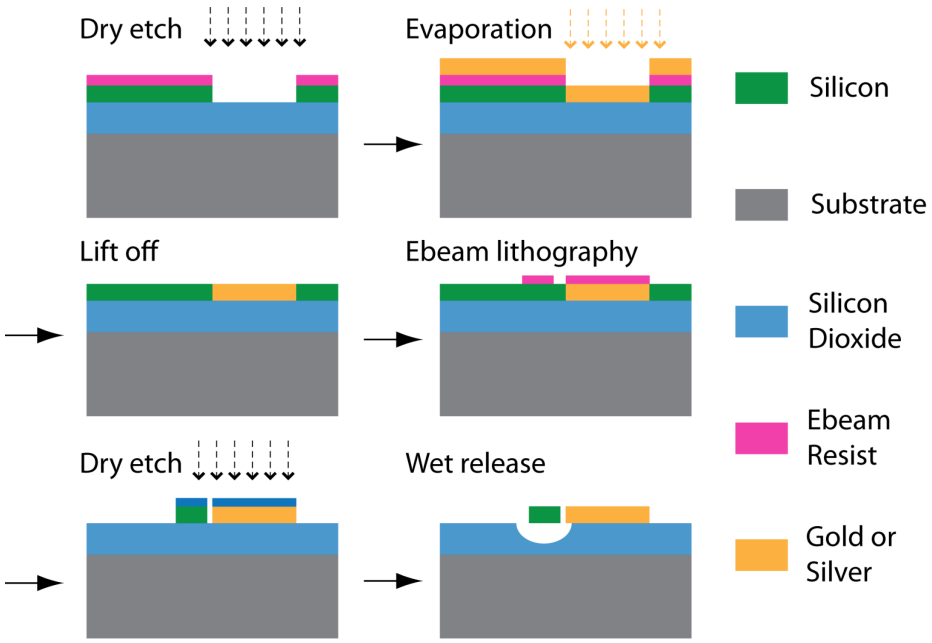

Fig. 3.5. Fabrication process diagram of the HPWG device.

All of the EBL processes are done with Vistec EBPG 5000+ system, with which 20 nm alignment precision can be routinely achieved.

waveguide and the gold patch. In the final step, the Si waveguide is plasma etched and released from the substrate by wet etching the buried oxide to form the suspended structure. All of the EBL processes are done with Vistec EBPG 5000+ system, with which 20 nm alignment precision can be routinely achieved.

The fabricated device is shown in Fig. 3.6. The device consists of a pair of grating couplers which couples light into and out of the device and a Mach-Zehnder interferometer (MZI) structure which is used to characterize the optical properties of the HPWG and

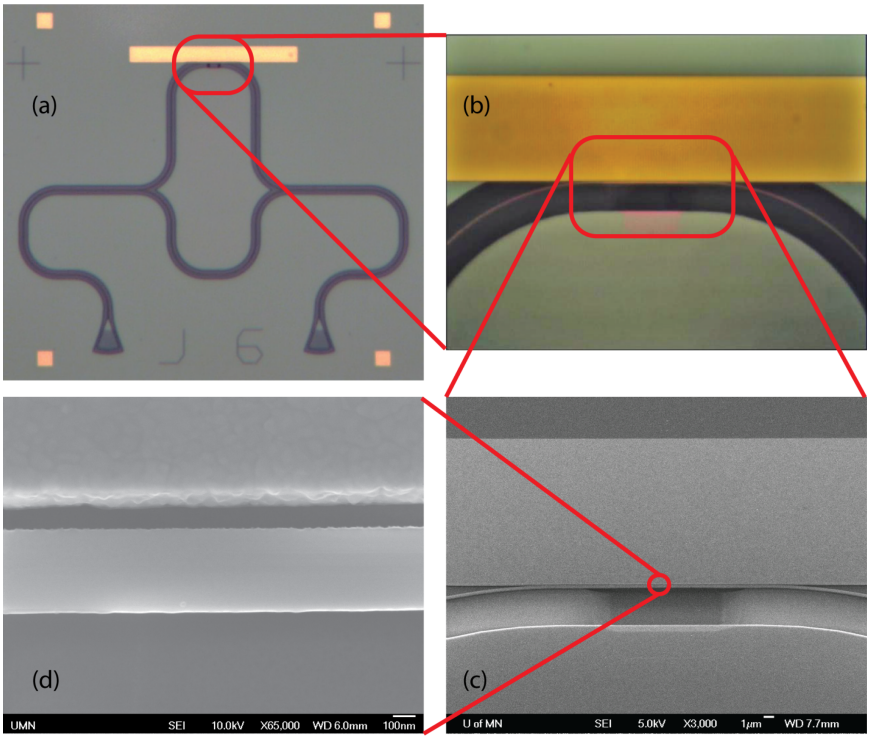

Fig. 3.6. Images of the fabricated HPWG device.

(a) Optical microscope image showing the device overview. (b) Optical microscope image showing the HPWG with gold and suspended Si waveguide. (c) SEM image showing the HPWG with gold and suspended Si waveguide. (d) SEM image showing the gap in the HPWG.

transduce the HPWG motion. HPWG is fabricated in only one of the arms of the MZI. The suspended length of the Si waveguide in HPWG is varied from 10 μm to 30 μm. The typical size of the gap in HPWG varies from 20 nm to 100 nm, depending on the design and the precision of alignment. To achieve longer suspended waveguide or smaller gap is challenging due to built-in stress induced buckling of the Si waveguides or stiction during the wet releasing process. Using the cold development process can noticeably improve the smoothness of the gold structure. The root mean square (RMS) value of the gold surface line edge roughness (LER) is estimated to be about 15 nm.

3.4. Optical characteristics

In order to confirm the excitation of the HPM, we systematically measured the optical loss in HPWG with varying lengths and gap sizes using the MZI structures. Since the reference arm of the MZI is a low-loss Si waveguide, the optical loss (or the decay constant) in the HPWG arm can be derived from the extinction ratio (*ER*) of the MZI transmission spectra, using Eq. (3.19).

$$\alpha = -\frac{20}{L}\log_{10}\left(\frac{\sqrt{ER}-1}{\sqrt{ER}+1}\right) \ \left[\text{dB/m}\right]. \tag{3.19}$$

In Fig. 3.7a, the MZI transmission spectra of HPWG with the same Si waveguide width and gap size but four different lengths are compared, showing decreasing *ER* with increasing length—hence increasing total loss, in agreement with theory. These measurements were conducted without releasing the Si waveguide in the HPWG to avoid

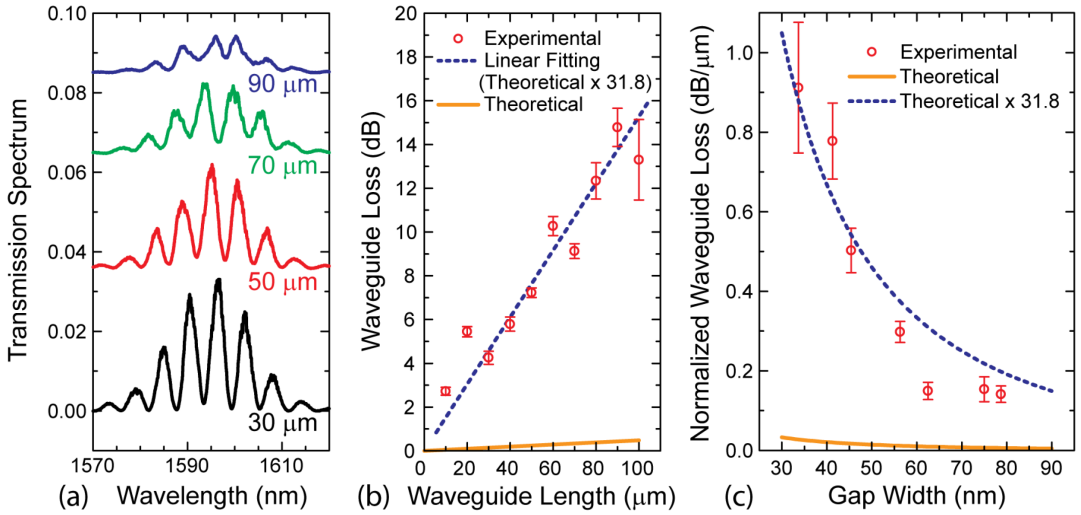

Fig. 3.7. Optical characteristics of the fabricated HPWGs.

Optical characteristics of the fabricated HPWGs with 450 nm wide Si waveguides. The measured HPWG loss is about 30 times higher than theoretical calculation. (a) MZI transmission spectra showing deceasing extinction ratio as the length of the HPWG is increased. The gap is 100 nm. (b) Experimental and theoretical results of the waveguide loss as a function of HPWG length. The gap is 100 nm. (c) Experimental and theoretical results of the waveguide loss normalized to unit HPWG length as a function of the HPWG gap.

the uncertainty induced in the wet etching process. This approach is justified by simulation results, which suggest that the presence of the SiO_2 substrate only slightly perturbs the HPM and introduces insignificant change to the mode profile and optical loss. The linear dependence of total loss on the HPWG length is further shown in Fig. 3.7b. However, the measured value of total loss is about 30 times higher than the theoretical expectation. In Fig. 3.7c, the normalized loss is plotted against HPWG gap width, showing qualitatively the same trend as the theory, but again is about 30 times higher. We attribute this large

discrepancy to the inevitable metal surface roughness and other non-idealities in the fabrication process.

3.5. Optomechanical characteristics

In order to determine the generated optical force and demonstrate the force enhancement effect, for each device we conducted the thermomechanical noise measurement to calibrate the displacement transduction gain factor and subsequently, driven frequency response measurement to determine the normalized local optical force p_n generated in the HPWG.

3.5.1. Transduction gain factor calibration by thermomechanical noise measurement

The MZI structure is used to transduce the motion of the Si beam in the HPWG. The in-plane motion of the Si beam changes the gap in the HPWG and hence both the real and imaginary parts of the effective index, which further leads to power modulation at the output of the MZI. For a given probe laser wavelength and mechanical mode, this transduction should be linear when the amplitude of the Si beam displacement is small. The transduction gain factor G_j, defined as the derivative of the photodetector output voltage with respect to the amplitude q_j of the jth mechanical mode, can be calibrated by measuring the thermomechanical noise of the Si beam, as described in reference [16]. Here we only focus on the first in-plane mechanical mode because it is the most efficient to excite and detect.

For each device, first we measure the widths of the Si beam and gap in the HPWG by scanning electron microscope (SEM) imaging, as is shown in Fig. 3.6d. Next we use a low-power probe laser to measure the thermomechanical noise of the Si beam in the HPWG with a spectrum analyzer (SA) to obtain the resonance frequency of the first in-plane mechanical mode and its quality factor, namely ω_1 and Q_1, by fitting the experimental curve with Eq. (3.13). From the width, thickness and resonance frequency of the Si beam, using Eq. (3.7), we can determine its actual length, which is difficult to be accurately measured by SEM imaging. Subsequently the mode spring constant k_1 can be calculated with Eq. (3.11) and finally we use Eq. (3.13) again to derive the theoretical PSD of the thermomechanical noise and compare with the measured noise spectrum to calibrate the transduction gain G_1. The results from a typical device are shown in Fig. 3.8a, in which case the transduction gain is 4.82 V/nm.

3.5.2. Optical force measurement by driven response

Knowing all the key parameters of the Si beam and the transduction gain, we are ready to use Eq. (3.18) to measure the normalized local optical force p_n except for the last fraction on the right hand side, which can be obtained from driven frequency response measurement.

The driven frequency response of the Si beam is measured with the well-known pump-probe scheme. In addition to the probe laser, a pump laser is sent into the device. The pump laser is power modulated using an electro-optical modulator with the modulation

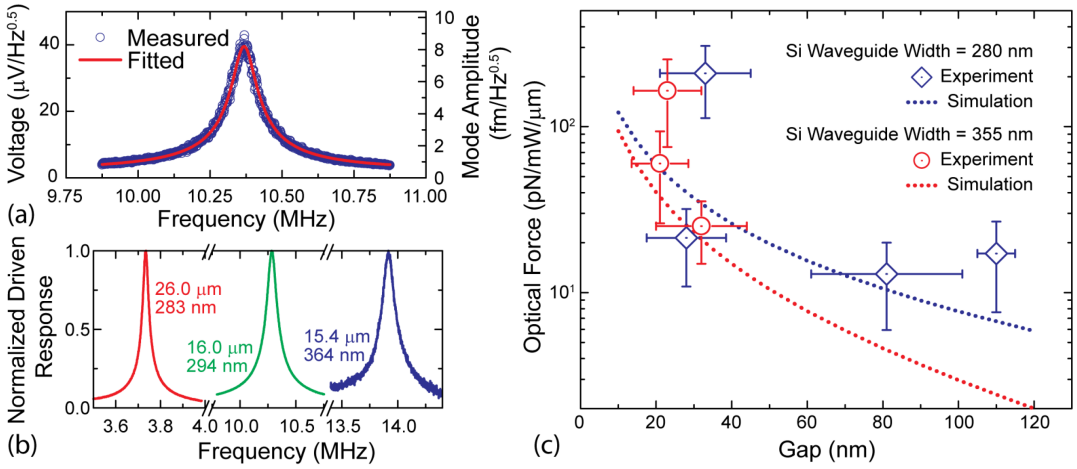

Fig. 3.8. Optomechanical measurements of the HPWG.

(a) Thermomechanical noise measurement for transduction calibration. In this case, G_1=4.82 V/nm. (b) Normalized driven responses from 3 representative devices, showing peaks at their respective resonance frequencies. The length and gap size of each device are labeled nearby its resonance peak. (c) The measured normalized local optical forces plotted against the gap width, for two different Si waveguide widths in the HPWG. The symbols are experimental results while the dotted lines are simulation results.

frequency swept near the resonance frequency of the Si beam. It generates a dynamic optical force to excite the in-plane vibration of the Si beam. Meanwhile the mode amplitude of the Si beam is measured by the probe laser at the same wavelength at which the transduction gain factor has been calibrated. A tunable Fabry-Perot filter is used in front of the photodetector to filter out the pump laser. The driven frequency response of the Si beam is thus measured with a network analyzer and converted into the Si beam mode amplitude using the calibrated transduction gain factor. Typical experimental results from three different devices are shown in Fig. 3.8b, after normalization for ease of comparison. In the

final step, the normalized local optical force is calculated by substituting the experimental results for all the parameters into Eq. (3.18), where α is calculated from the *ER* and HPWG length, $\tilde{q}_1(\omega_1)$ is extracted from the peak point of the measured driven frequency response and $\tilde{P}(0,\omega_1)$ is carefully calibrated from the measured MZI transmission spectrum.

The measured normalized local optical forces from seven devices of different Si waveguide widths and gaps are plotted in Fig. 3.8c, showing good agreement with the theoretical calculation. The horizontal error bars originate from the fact that the actual gaps are not uniform over the entire HPWG length, due to the alignment uncertainty in the EBL process and the slight buckling of Si beams induced by the built-in stress in the top Si layer of SOI wafer. The vertical error bars account for all the uncertainties in the measurement process, including the uncertainties of the actual optical power in the HPWG due to interference effects induced by reflections where mode conversion happens, and the non-uniform gap in the HPWG, which cannot be described by the model developed in this work. In the plot, the relative uncertainty introduced by the two reasons above is estimated to be about 40%. Even though this estimation may be crude because the gap width varies randomly, measurement of multiple devices can help reduce this uncertainty. Thus, the apparent agreement between theoretical and experimental results in Fig. 3.8c confirms the enhanced optical force in HPWG within the experimental precision. When the gap size is as low as 20 nm, the optical force per unit length is determined to be approximately 100

pN/μm/mW, which is 200 times larger than that in a silicon waveguide coupled to silicon dioxide substrate [16].

3.6. Conclusion and discussion

In this work we fabricated HPWG devices and for the first time experimentally characterized their optical and mechanical properties and optical forces. The experimental results confirmed the theoretically predicted optical force enhancement, although the loss is significantly higher than theoretical prediction due to the metal surface roughness and other non-idealities in the fabrication process. Future work can be focused on further reducing the metal surface roughness by techniques such as template stripping [63]. Despite of its lossy nature, HPWG is a potentially very attractive solution in applications where large optical force is desired in limited device footprint to change device structure and/or circuit topology, such as mechanical memory operation, all-optical signal processing, tunable or reconfigurable optical circuits.

Chapter 4. Multichannel Cavity Optomechanics for All-Optical Amplification of Radio Frequency Signals [34]

Optomechanical phenomena in photonic devices provide a new means of light–light interaction mediated by optical force actuated mechanical motion. In cavity optomechanics, this interaction can be enhanced significantly to achieve strong interaction between optical signals in chip-scale systems, enabling all-optical signal processing without resorting to electro-optical conversion or nonlinear materials. However, current implementation of cavity optomechanics achieves both excitation and detection only in a narrow band at the cavity resonance. This bandwidth limitation would hinder the prospect of integrating cavity optomechanical devices in broadband photonic systems. Here we demonstrate a new configuration of cavity optomechanics that includes two separate optical channels and allows broadband readout of optomechanical effects. The optomechanical interaction achieved in this device can induce strong but controllable nonlinear effects, which can completely dominate the device's intrinsic mechanical properties. Utilizing the device's strong optomechanical interaction and its multichannel configuration, we further demonstrate all-optical, wavelength-multiplexed amplification of radio-frequency signals.

4.1. Introduction

In nanoscale photonic devices, one optical signal can generate sufficient optical force to mechanically displace or deform the optical path that another optical signal takes and consequently alter its propagation [9], [16], [47], [60]. Such an optomechanical effect permits optical signals to interact directly and can be implemented on an integrated device platform using only optically passive materials such as silicon and glass, circumventing the conventional need of electro-optical conversion or nonlinear optical materials [19], [46], [70]–[72]. Using high finesse optical cavities, optomechanical interaction can be resonantly enhanced. Research in cavity optomechanics exploits the dynamical interplay between the intra-cavity optical field and the mechanical motion of the device, leading to demonstrations of unprecedented phenomena including backaction cooling [12], [15], [73], [74], normal mode splitting [75] and optomechanically induced transparency [22], [23]. Other than fundamental studies, a plethora of promising applications of cavity optomechanics, including tunable photonic filters and wavelength router [19], [46], wavelength conversion and switching [71], [72], radio-frequency optomechanical oscillators [76], [77] and non-volatile optical memory [24], have emerged.

However, in the cavity optomechanical systems demonstrated so far, only one optical channel is available for both excitation and detection lasers to couple into the cavity. For example, in systems based on micro- and nanoscale cavities, optical coupling with the cavity is through either a single optical fiber [17], [46], [78] or an integrated waveguide [19], [79]. Furthermore, in these systems, because the mechanical element is embedded

inside the high finesse cavity, optomechanical effects can only be interrogated within extremely narrow bandwidths at the discrete resonance frequencies. These requirements impose a stringent limitation on the available spectral range to operate cavity optomechanical devices, thus limiting the prospect of practical applications. Should cavity optomechanics be integrated with other photonic devices, which may work at very different frequencies such as in a wavelength multiplexed system, a broad operation bandwidth would be necessary.

We propose a multichannel scheme of cavity optomechanics with two waveguides that separate the mechanical element from the optical cavity. The first waveguide is denoted as the control that is used to couple a laser into the cavity to excite its resonance and generate optomechanical force. The mechanical element resides outside the cavity in the second signal waveguide so that its optomechanical motion can be readout over a broad wavelength range. When tuned to resonance, the cavity resonantly enhances the optical force on the mechanical element. Moving the mechanical element out of the optical cavity and adding the second waveguide has the following benefits: first, the mechanical device can be optimized without sacrificing the quality of the optical cavity; second, the thermo-optic effect that often plagues optomechanical effects becomes insignificant because the mechanical device is outside the cavity and the readout signal can be decoupled from the cavity resonance; third and more importantly, the freedom to use a readout wavelength in the signal waveguide over a broad band offers great flexibility for cavity optomechanics to be integrated with other nanophotonic devices to achieve advanced functionalities.

4.2. Multichannel Design of a Cavity Optomechanical Device

Our device is comprised of a micro-disk cavity coupled with a control and a signal waveguide, in the typical configuration of an add-drop filter as illustrated in Fig. 4.1a. A scanning electron microscope image of the actual device is shown in Fig. 4.1b. The control waveguide at the top couples with the micro-disk with a gap of 120 nm, providing the first channel to excite the resonance modes of the cavity. The second channel is through the signal waveguide at the bottom. In it, a small gap (50 nm) is created and a 22-μm long cantilevered waveguide is suspended from the substrate. The evanescent optical field of the micro-disk's resonance mode applies a gradient optical force on the signal waveguide

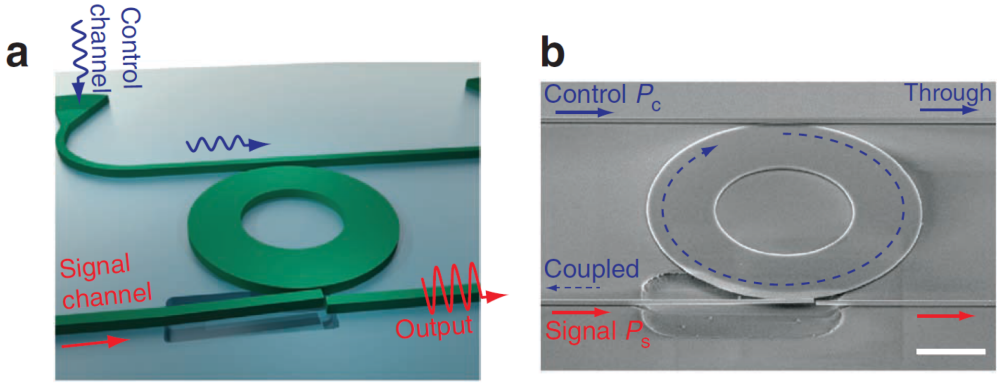

Fig. 4.1. A multichannel cavity optomechanical device.

(a) Schematic illustration of the device, which features a micro-disk cavity coupled with a control and a signal channel waveguide. The key mechanical element is the cantilevered section in the signal waveguide whose motion can be detected over a broad bandwidth by measuring the optical transmission of the waveguide. (b) Scanning electron microscopy image of the device, highlighting the micro-disk (10 μm in radius) and the cantilever waveguide.

and, inversely, the signal waveguide's motion also dispersively perturbs the cavity's resonance [78], [79]. In contrast to the conventional phase sensitive detection method, which relies on the cavity resonance, the optomechanical motion of the signal waveguide is detected directly by monitoring the intensity of transmission. Previously it has been shown that this intensity detection scheme is inherently broadband; even an incoherent light source can be used to achieve high detection sensitivity [49]. To limit the number of resonance modes, the micro-disk is designed in an annular shape with a major and a minor radius of 10 and 5 μm, respectively. The measured transmission spectrum through the control waveguide and the coupling spectrum from the control to the signal waveguide

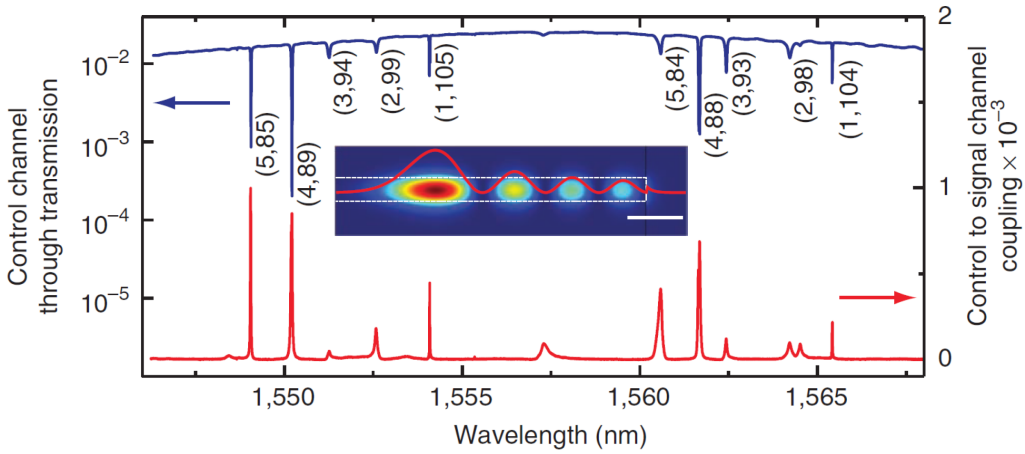

Fig. 4.2. Transmission spectra of the device.

The measured spectra of the transmission through the control waveguide (blue trace, logarithmic scale, left axis) and the coupling from the control to the signal waveguide (red trace, linear scale, right axis), respectively. Inset: finite element simulation result showing the square of transverse electric field component and its profile (red overlay curve) of the fourth radial modes. The dashed box outlines the micro-disk.

(that is, the drop port transmission as in an add-drop filter) are shown in Fig. 4.2, where each resonance mode is labeled with its radial and azimuthal mode order number as (p, m). Transverse-electric (TE) resonance modes with radial mode number from one to five can be observed in the spectra. In the transmission spectrum of the control waveguide, the cavity modes show varying extinction ratios because of the difference in their coupling efficiency with the waveguide mode. Among them, we focus on the TE mode (4, 89) that has the highest loaded quality factor Q of 5×10^4 (corresponding finesse is 561) and extinction ratio of more than 20 dB, indicating a nearly critical coupling condition. The inset of Fig. 4.2 shows the square of the transverse electric field component of the fourth-order radial mode, calculated with finite element method [80]. To detect the cantilevered signal waveguide's motion, the transmission of the signal waveguide is monitored using a laser with any wavelength that is different from the micro-disk's resonance (for example, at 1,555 nm in Fig. 4.2). To obtain a linear response to its motion, the fixed end of the waveguide is designed during patterning to offset laterally from the cantilevered end by 250 nm, causing a manageable addition of 3 dB insertion loss (see Section 4.9).

We first demonstrate the actuation of the signal waveguide by exciting the resonance of the micro-disk from the control waveguide. The evanescent field of the circulating light in the micro-disk generates a gradient optical force on the signal waveguide [78], [79]. This force is attractive toward the micro-disk and can be expressed as [79]:

$$F_{\mathrm{c}}(x) = -\frac{2P_{\mathrm{in}}\gamma_1}{\omega\,\gamma^2}\frac{g(x)}{1+\delta^2} \tag{4.1}$$

Here, x is the signal waveguide's lateral position (positive is in the direction away from the micro-disk), P_{in} is the input optical power in the control waveguide. $\delta = (\omega - \omega_{\mathrm{c}})/\gamma$ is the normalized detuning of the control laser frequency ω relative to the cavity resonance frequency $\omega_{\mathrm{c}}(x)$, which is dependent on the position of the signal waveguide. $\gamma = \gamma_1 + \gamma_2 + \gamma_{\mathrm{i}} = \omega_{\mathrm{c}} / 2Q$ is the total damping rate of the cavity including the coupling rate with the control and the signal waveguides γ_1 and γ_2, respectively, and the cavity's intrinsic damping rate γ_{i}. $g(x)$ is the important optomechanical coupling coefficient, which under the perturbation approximation [78], depends exponentially on the signal waveguide's displacement $\delta x = x - x_0$ and can be expressed as $g(x) = \partial\omega_{\mathrm{c}} / \partial x = g_0 \exp\left(-2\alpha\,\delta x\right)$, where α is the evanescent field decay constant of the cavity resonance mode. In our device, the static value of g_0 for the TE mode (4, 89) is experimentally determined to be $2\pi \cdot 11.3$ MHz/nm (see Section 4.10) [81]. From Eq. (4.1), it is clear that when the control laser frequency is tuned to the cavity resonance ($\delta_0 = \delta(x = x_0) = 0$), the static optical force $F_{\mathrm{c}}(x_0)$ will be maximized, enhanced by the cavity power build-up factor. Modulating the input power P_{in} will generate a time varying optical force on the cantilever waveguide to excite its mechanical resonance. The Fig. 4.3a shows the measured small-amplitude mechanical response of the signal waveguide using a

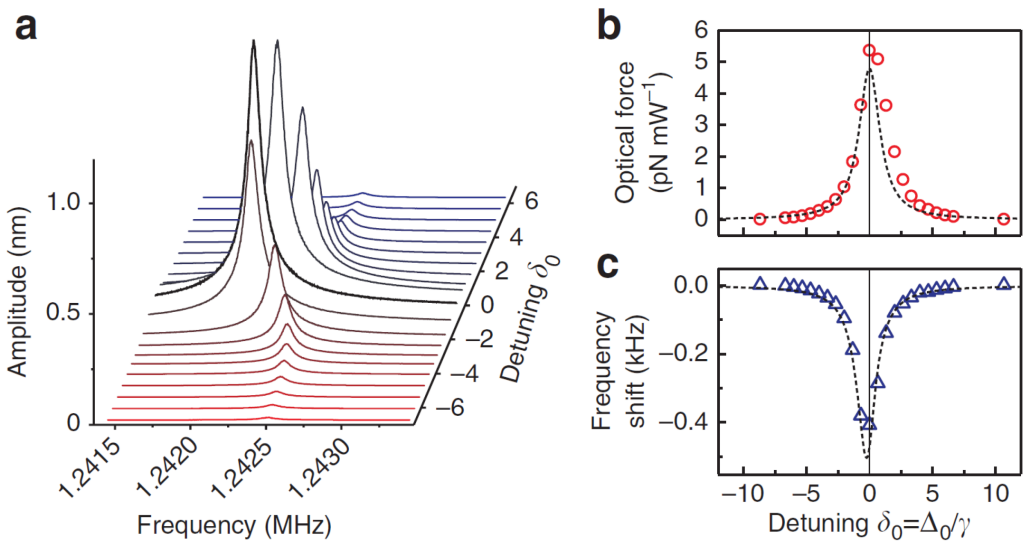

Fig. 4.3. Optical force and optical spring effect.

(a) Small amplitude resonance response of the cantilevered signal waveguide driven by the control laser with constant power (alternating current (AC) power: 0.76 μW, DC power: 0.52 mW) and varying detuning. The vibration amplitude reaches maximum when the control laser is tuned to the cavity resonance. (b,c) Total attractive optical force on the signal waveguide and resonance frequency shift as a function of detuning. Black dashed lines show theoretical results (see Section 4.6).

low modulated optical power (0.76 μW peak value) but varying detuning value δ_0. The signal waveguide vibrates with a resonance frequency of 1.24 MHz and a quality factor Q_m of 1.6×10^4 in vacuum. The resonance amplitude increases drastically when the detuning approaches zero. The Fig. 4.3b shows the calibrated measurement of the optical force (normalized to the input power) on the signal waveguide versus detuning values, demonstrating a resonant enhancement factor of more than 500 as expected from the theory (see Section 4.8). In addition, the mechanical frequency of the signal waveguide also appears to depend on the detuning, as shown in Fig. 4.3c. This dependence is known as the

optical spring effect from the linear variation of optical force with the device's position. In contrast to conventional cavity optomechanics in which the optical spring vanishes when the detuning is zero [13], [14], [82], our result shows a maximal negative frequency shift near zero detuning, indicating the strongest negative optical spring. This distinction is because the optical force in our system is generated by the evanescent field outside the cavity, instead of the intra-cavity field. The observed phenomenon can be well explained theoretically as plotted with dashed lines in Fig. 4.3b and Fig. 4.3c and discussed in detail in Section 4.6.

4.3. Controllable Optomechanical Nonlinearity

Cavity optomechanical devices are inherently nonlinear mechanical systems [83] because the optomechanical interaction involves the intra-cavity field, which depends nonlinearly on the mechanical elements' position. Exploiting the nonlinear dynamics in cavity optomechanical systems will be especially important to applications that need to operate the devices in the high-amplitude regime, such as optomechanical oscillators [76], [77] and optomechanical memory [24]. As can be seen from Eq. (4.1), the optical force F_c in our device is a nonlinear function of the signal waveguide's displacement $\delta x = x - x_0$. The expression can be expanded near the static position x_0 to the higher orders of δx as $F_c(x) = F_c(x_0) + k_1 \delta x + k_2 \delta x^2 + k_3 \delta x^3 + O(\delta x^4)$. Here, k_1 is the force constant of the optical spring, k_2 and k_3 are the quadratic and cubic nonlinear force constants,

respectively. The mechanical frequency of the signal waveguide is modified by the optical spring k_1 to be $\omega_m^2 = \omega_{m0}^2 - k_1/m_{eff}$, where m_{eff} is the effective mass of the fundamental mechanical resonance mode. The nonlinear components in the optical force induce mechanical nonlinearity with quadratic and cubic nonlinear coefficients given by: $\alpha_2 (= -k_2/m_{eff})$ and $\alpha_3 (= -k_3/m_{eff})$. In the small-amplitude regime, the nonlinear terms are insignificant and only the frequency down shift due to the optical spring k_1 can be observed as in Fig. 4.3. When the signal waveguide's vibration is excited to large amplitude, the cubic nonlinear term becomes important and the signal waveguide vibrates as a nonlinear Duffing oscillator with bifurcation in its frequency response. In this regime, the quadratic term as a small correction to the Duffing nonlinearity is negligible [84]. The critical amplitude a_c, at which the intrinsic mechanical nonlinearity becomes evident, is evaluated to be about 1 μm using the expression $a_c = 6.3L/\sqrt{Q_m}$ [85], where $L = 22$ μm is the length of the cantilever and $Q_m = 1.6 \times 10^4$ is its mechanical Q factor. Such large amplitude cannot be reached in our device because the gap between the micro-disk and the signal waveguide is only 120 nm. However, the optomechanical contribution to the cubic coefficient α_3 is proportional to the optical power level (see Section 4.7). Hence, even at amplitude much lower than a_c, with sufficient optical power strong optomechanical nonlinearity can be induced to dominate the device's mechanical response.

To demonstrate the optomechanical nonlinearity, we apply a third laser, denoted as the tuning laser, with a static power level to the control waveguide. The magnitude of the induced optomechanical nonlinearity can be controlled by varying the power level and the frequency of the tuning laser. The result is shown in Fig. 4.4 and Fig. 4.5. With the tuning laser power at as low as 100 μW (in the control waveguide), strong nonlinearity can be observed when the signal waveguide's vibration amplitude is above 50 nm, only one-twentieth of the mechanical critical amplitude a_c. Most interestingly, the detuning of the tuning laser has a significant effect on the device's nonlinearity. The Fig. 4.4a and Fig. 4.4b show the measured amplitude-frequency response when the modulation level of the control laser power is gradually increased (direct current (DC) power is constant at 80 μW)

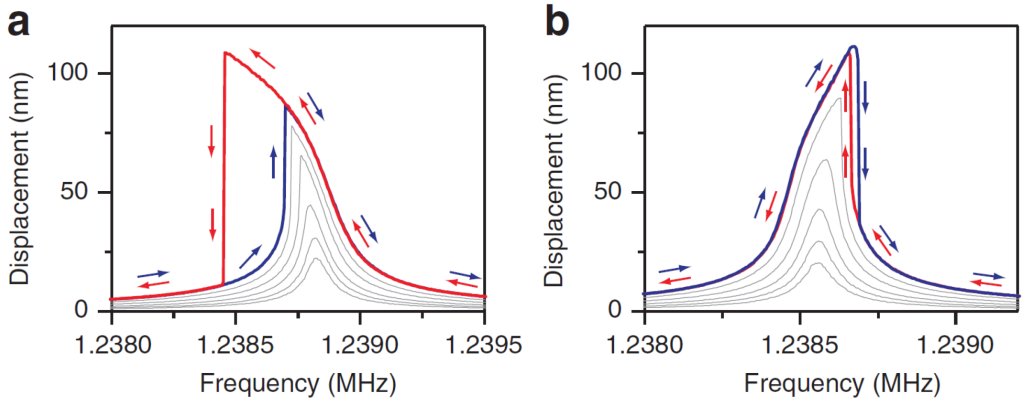

Fig. 4.4. Controllable optomechanical nonlinearity. (Part 1.)

(a,b) Amplitude-frequency response curves of the signal waveguide under increasing drive amplitude, measured with 350 μW tuning laser red-detuned (a, $\delta_0 = -0.5$) and blue-detuned (b, $\delta_0 = 0.4$) to the cavity resonance. The red and blue curves are obtained by sweeping the drive frequency downward and upward, respectively, and with the same modulation level.

and the tuning laser power is fixed at 350 μW. When the tuning laser is red-detuned to the cavity resonance (Fig. 4.4a, $\delta_0 = -0.5$), the response shows the softening nonlinearity of a typical Duffing oscillator with the characteristic amplitude jumps and the hysteresis effect when the actuation frequency is swept upward (blue trace) and downward (red trace), indicating that the cubic nonlinear coefficient α_3 is negative. The situation changes when the tuning laser is blue-detuned, the response instead shows hardening nonlinearity (Fig. 4.4b, $\delta_0 = 0.4$), indicating a positive α_3. From these measured response curves, the value of α_3 can be determined experimentally (see Section 4.7) and the results for varying detuning δ_0 are plotted in Fig. 4.5a. It clearly shows that the cubic nonlinear coefficient is controlled by the tuning laser and its sign can be changed depending on the detuning. The maximal negative and positive values of α_3 are obtained experimentally with δ_0 equals −0.67 and 0.67, respectively. At blue detuning of $\delta_0 \sim 0.02$, the value of α_3 vanishes and the cubic nonlinearity diminishes, allowing higher order nonlinearity to appear. The theoretical value of α_3 is also calculated using only experimentally determined and numerically simulated values of the parameters in Eq. (4.1) and plotted in Fig. 4.5a (see Section 4.7), in an excellent agreement with the experimental result. The deviation is attributed to the imprecision in determining the actual detuning value because of the thermal drift of the cavity resonance. The Fig. 4.5b shows that the value of α_3 is proportional to the power of the tuning laser for both softening (red) and hardening (blue) situations, as expected from theoretical analysis. The rich and completely controllable

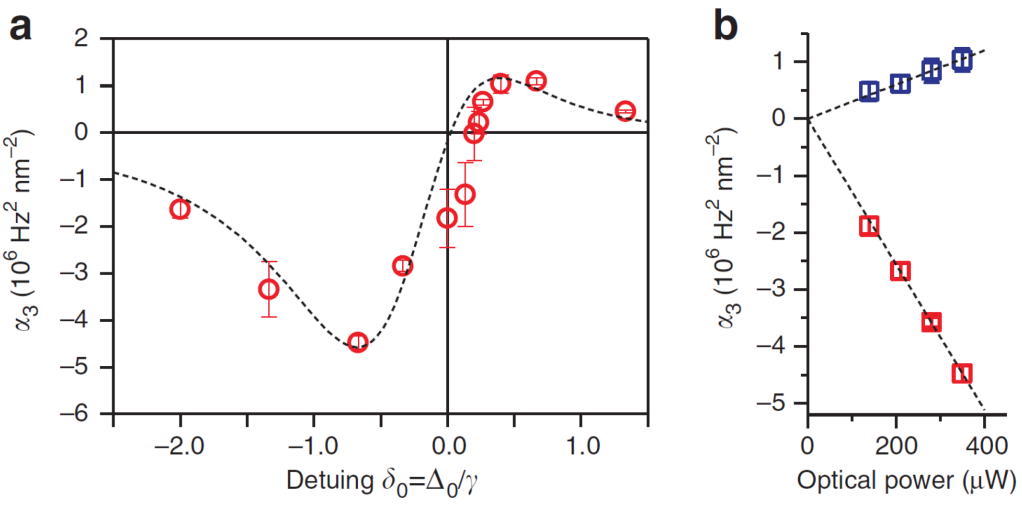

Fig. 4.5. Controllable optomechanical nonlinearity. (Part 2.)

(a) The measured cubic (Duffing) nonlinear coefficient α_3 as a function of tuning laser detuning. α_3 can be controlled to be negative or positive by changing the detuning. Black dashed line shows the theoretical results with no free parameters, using only experimentally determined and numerically simulated values of the parameters. Error bars: s.d. from five measurements. (b) The measured value α_3 for red ($\delta_0 = -0.67$) and blue ($\delta_0 = 0.67$) detuned laser at various optical power of the applied tuning laser, showing a proportional dependence. Error bars: s.d., from five measurements.

optomechanical nonlinearity in cavity optomechanics, demonstrated here for the first time, can be harnessed to explore nonlinear phenomena in nanomechanical oscillators [83], including parametric amplification [86], synchronization [87] and stochastic dynamics [88], [89].

4.4. Optomechanical Signal Amplification

In cavity optomechanics, by leveraging the enhancement from both the optical and mechanical resonances, a low-power optical signal can be used to modulate a high-power

optical signal via their enhanced optomechanical interaction, making it possible to achieve a net signal gain at the modulation frequency. Such a mechanical means of signal amplification is analogous to the principles of electromechanical relays or electronic transistors (Fig. 4.6a) and has found important applications [90], [91]. In addition, our multichannel design of cavity optomechanics features a broadband transmission in the signal waveguide, making wavelength multiplexing possible. In our device, the signal gain factor (*GF*) is defined as the ratio between the alternating current (AC) optical power input to the control waveguide and the modulated output power from the signal waveguide. At the mechanical resonance frequency, *GF* is maximized and given by

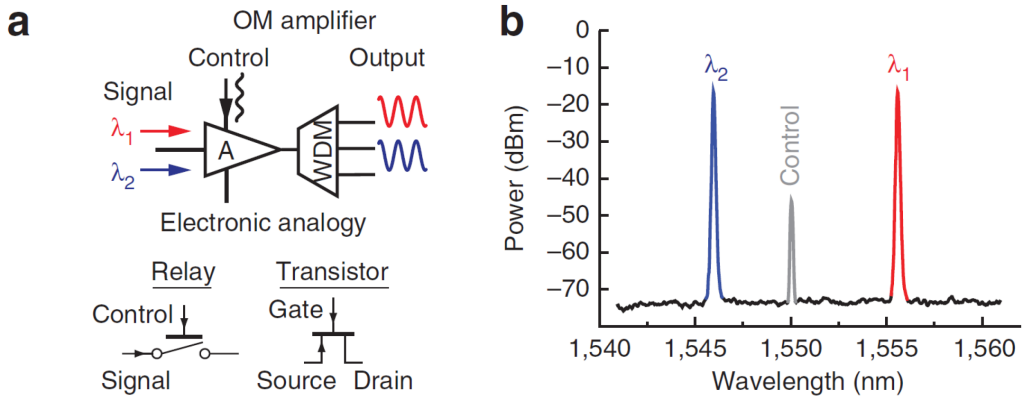

Fig. 4.6. All-optical signal amplification and wavelength multiplexing. (Part 1.)

(a) The principle of optomechanical amplification is analogous to that of electromechanical relays or electronic transistors. A small signal in the control waveguide (or gate) can be used to modulate a large signal in the signal waveguide (or source to drain) to achieve a signal gain. Wavelength multiplexing can also be achieved. (b) Optical spectrum measured at the output of the signal waveguide, showing signals at two wavelengths and the leaked control.

$$GF(\omega_{\mathrm{m}}) = \frac{\tilde{P}_{\mathrm{out}}}{\tilde{P}_{\mathrm{in}}} = \left(\frac{\partial T_{\mathrm{s}}}{\partial x}\right)\left(\frac{\partial F_{\mathrm{c}}}{\partial P_{\mathrm{c}}}\right)\left(\frac{Q_{\mathrm{m}}}{k_{\mathrm{m}}}\right)P_{\mathrm{s}} \tag{4.2}$$

Here, $\partial T_{\mathrm{s}}/\partial x$ is the response of the signal channel's transmission to the lateral motion of the cantilever waveguide, $\partial F_{\mathrm{c}}/\partial P_{\mathrm{c}}$ is the efficiency of optical force generation, which is enhanced by the cavity finesse as demonstrated in Fig. 4.3. Although in principle arbitrarily large *GF* can be attained with sufficient signal power P_{s} as *GF* is proportional to P_{s}, in practice the maximal *GF* is limited by the power handling capability of the device. The high finesse of the micro-disk cavity and the high mechanical quality factor Q_{m} and compliance ($1/k_{\mathrm{m}}$) of the cantilevered waveguide allows a high gain value to be attained with a low signal power P_{s}.

To demonstrate the principles of optomechanical amplification of radio-frequency signal and wavelength multiplexing with our device, two continuous wave (CW) lasers were input to the signal waveguide and the control laser was modulated at the mechanical resonance frequency. The Fig. 4.6b shows the optical spectra at the output of the signal waveguide, showing the two optical signals at wavelength λ_1 and λ_2, which can be freely selected over a broad spectral range as long as the cavity resonance wavelengths are avoided. Also seen in Fig. 4.6b is the leaked control laser with 30 dB lower power than the signal lasers because the micro-disk also acts as a filter. A standard wavelength division-multiplexing filter is used to separate the two signals at wavelengths λ_1 and λ_2. The Fig. 4.7a shows the time domain traces of the input modulation signal (DC power 170 μW at

1,550.21 nm) at the control waveguide and two output signals (DC power 450 μW at 1,546.12 and 1,555.75 nm) from the signal waveguide, modulated at the mechanical resonance frequency of 1.24 MHz. The result shows that the modulated amplitude of the input signal is amplified by a factor of three in the output signal. Because of the broadband signal waveguide, this *GF* is independent of the signal wavelength so the device is suited to optical systems using wavelength multiplexing. The *GF* increases proportionally with the input signal power P_s and is consistent for the two different signal wavelengths, as shown in Fig. 4.7b. Similar silicon micro-disk cavity with quality factor as high as 3 million

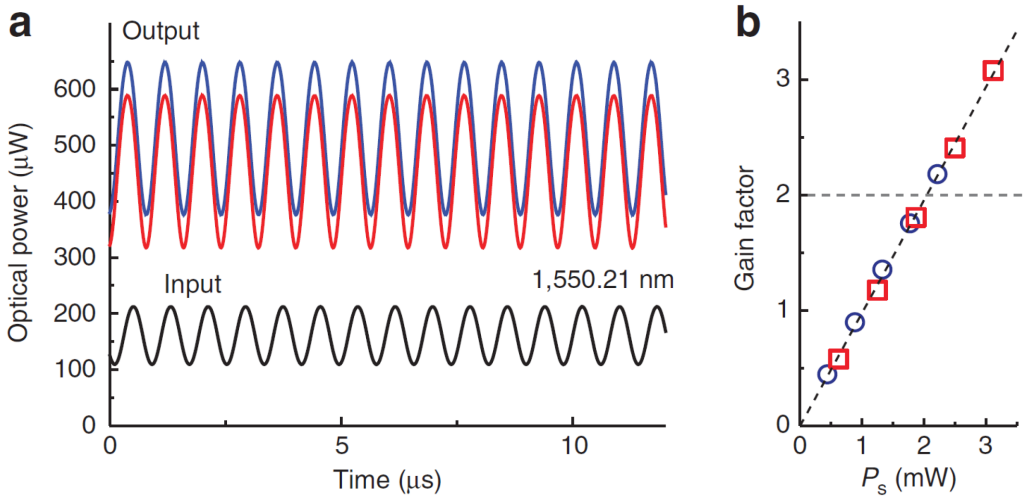

Fig. 4.7. All-optical signal amplification and wavelength multiplexing. (Part 2.)

(a) Time domain traces of the input (black) and output signals at two different wavelengths (blue: 1,546.12 nm and red: 1,555.75 nm), showing the input signal is amplified by a gain factor of three at the output. One output trace (blue) is intentionally shifted upward for clarity. (b) The gain factor is proportional to the optical power in the signal waveguide but independent of the signal wavelength (blue: 1,546.12 nm and red: 1,555.75 nm). A gain factor of two can be achieved with a signal power of only 2 mW.

has been reported in the literature [92] so it is possible to achieve even higher *GF* with a much lower power level. Although the operation speed of the device currently is limited by the relatively low mechanical frequency of the cantilevered signal waveguide, it is feasible to improve the mechanical frequency to the hundreds of megahertz range [93], [94], making it suited for radio-frequency (RF) photonics applications.

Recently, micro- and nanoscale mechanical switches and relays have been revisited for their potential in integrated circuits for low power computation [95] and for harsh environment applications [96]. Optomechanical devices also provide unique attributes that are unattainable with conventional optical devices, such as the all-optical signal amplification demonstrated here and the ability to be reconfigured and re-programmed [19], [78], [97]. The broad optical bandwidth enabled by the new multichannel configuration offers great flexibility for cavity optomechanics to be integrated at a higher level, allowing their remarkable properties to be applied in cohorts with conventional photonic systems for optical and RF communications.

4.5. Device Fabrication and Measurement Scheme

The devices are fabricated on commercial SOI wafers (SOITEC) with 220 nm silicon layer and 3 μm buried oxide, using standard electron beam lithography and plasma dry etching processes. The cantilevered section of the signal waveguide is released from the substrate by wet etching the buried oxide layer through a photoresist mask patterned by photolithography. Critical point drying is used to prevent the collapsing of the cantilevered

waveguide caused by the viscous dragging effect during etchant solution evaporation. The released section of the signal waveguide is 22 μm long, 420 nm wide with a mechanical spring constant of 69.4 mN/m. With a gap of 50 nm and a lateral offset of 250 nm between the cantilevered end and the receiving end, the signal waveguide has an estimated total insertion loss of 7.8 dB.

A schematic of the measurement setup is shown in Fig. 4.8. The control, signal and tuning lasers are coupled into the device by aligning a linear array of single-mode fibers, spaced 250 μm and mounted on a V-groove (OZ optics) chip, to the integrated grating couplers on the device. Each fiber to grating coupler interface has a typical coupling efficiency of 15%. All the power values mentioned in the manuscript refer to the power in the waveguide immediately after the coupler and are carefully calibrated and monitored.

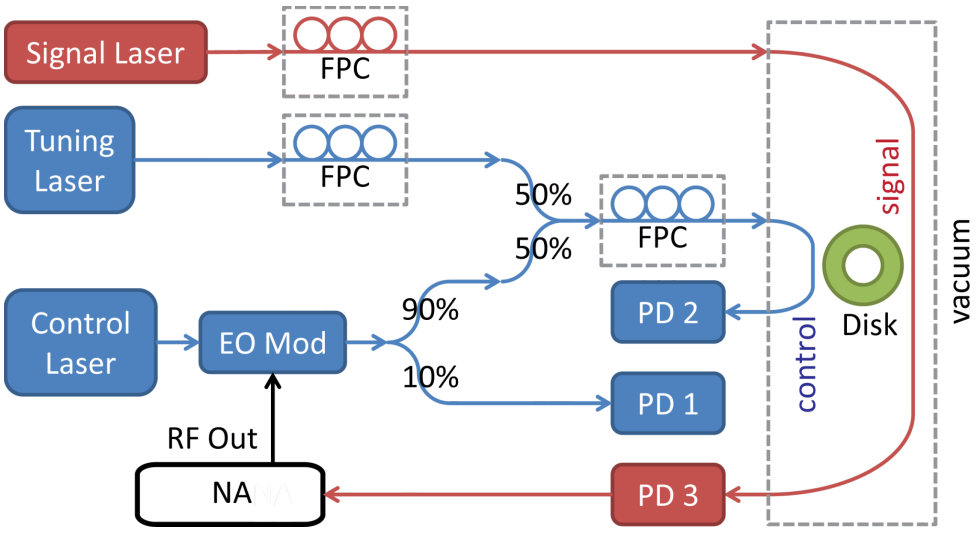

Fig. 4.8. Schematic of the measurement setup.

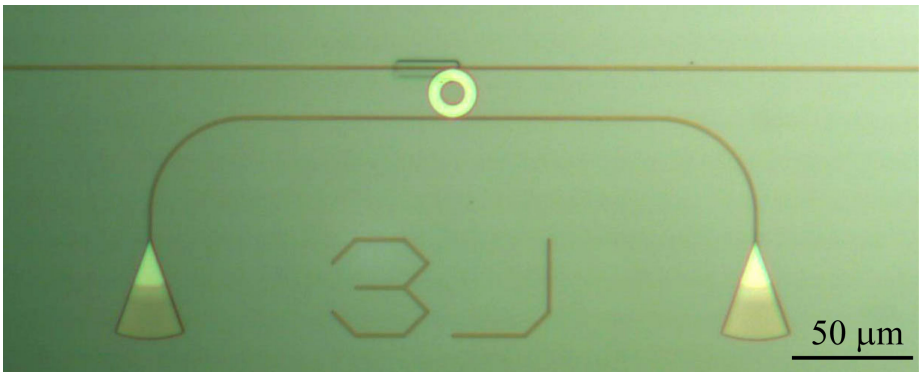

Fig. 4.9. Optical microscope image of the device measured in the experiment.

There are four grating couplers (two are shown) integrated with the control (bottom) waveguide and the signal (top) waveguide.

To achieve high mechanical quality factor, the measurements are conducted in a vacuum chamber with pressure of 2×10^{-4} Torr. A microscope image of the device that is measured during the experiment is shown in Fig. 4.9.

4.6. Theoretical Analysis of Nonlinear Optical Force

First, we define the coordinate system of our device as in Fig. 4.10. The optical force applied by the cavity on the signal waveguide is given in Eq. (4.1) [79] and is repeated here for convenience.

$$F_c(x) = -\frac{2P_{in}\gamma_1}{\omega}\frac{g(x)}{\Delta(x)^2+\gamma^2} \tag{4.3}$$

Here, the positive of x-axis is in the direction pointing away from the micro-disk. $\Delta(x)=\omega-\omega_c(x)$ is the laser (frequency ω) detuning relative to the cavity resonance

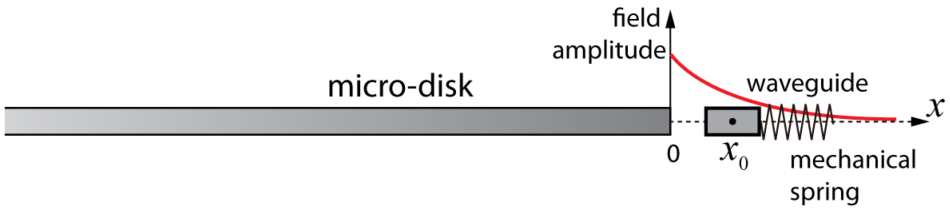

Fig. 4.10. Coordinate system defined in the theoretical calculation.

The red line marks the decaying field amplitude outside the micro-disk.

frequency $\omega_c(x)$ which is dependent on the position of the signal waveguide, $\gamma = \gamma_1 + \gamma_2 + \gamma_i$ is the total amplitude damping rate of the intra-cavity field including waveguide coupling rate γ_1 (for control waveguide), γ_2 (for signal waveguide) and intrinsic damping rate γ_i. Light is coupled to the cavity through the control waveguide, which is not moving. Here we are only concerned with the optical force on the cantilevered signal waveguide and its induced mechanical motion. One important parameter is the $g(x) = \partial\omega_c / \partial x$ factor which is the optomechanical coupling coefficient between the movable signal waveguide and the micro-disk cavity. Note here both $g(x)$ and the detuning $\Delta(x) = \omega - \omega_c(x)$ are dependent on the signal waveguide's position *x*. We note that the coupling rate γ_2 of the signal waveguide is also dependent of position *x*. However, in our device $\gamma_2 \ll \gamma_1$ so the optomechanical effect on the cavity damping is weak and neglected in the following analysis.

When the signal waveguide moves from its original position x_0 to an arbitrary position *x*, the corresponding new detuning $\Delta(x)$ can be expressed as:

$$\begin{aligned}\Delta(x) &= \omega - \omega_c(x) = \omega - \left[\omega_c(x_0) + \int_{x_0}^{x} \frac{\partial \omega_c}{\partial x'} dx'\right] \\ &= \omega - \omega_c(x_0) - \int_{x_0}^{x} g(x')dx' = \Delta_0 - \int_{x_0}^{x} g(x')dx'\end{aligned} \tag{4.4}$$

Here Δ_0 is the static detuning value when the waveguide is not moved. Using the perturbation treatment employed in [78], the optomechanical coupling coefficient, to the first order, has an exponential dependence on the signal waveguide's position:

$$g(x) = g(0)e^{-2\alpha x} = g(x_0)e^{-2\alpha(x-x_0)} = g_0 e^{-2\alpha(x-x_0)} \tag{4.5}$$

where α is the field amplitude decay constant outside the rim of the micro-disk and $g_0 = g(x_0)$ is the static value of the optomechanical coupling coefficient when the waveguide is not moved.

Thus, Eq. (4.4) can be written as:

$$\Delta(x) = \Delta_0 - \int_{x_0}^{x} g_0 e^{-2\alpha(x'-x_0)} dx' = \Delta_0 - \frac{g_0}{2\alpha}\left[1 - e^{-2\alpha(x-x_0)}\right] \tag{4.6}$$

Then substituting Eq. (4.5) and Eq. (4.6) into Eq. (4.3), the optical force can be expressed as:

$$\begin{aligned}F_c(x) &= -\frac{2P_{in}\gamma_1}{\omega} \frac{g_0 e^{-2\alpha\delta x}}{\left[\Delta_0 - g_0\left(1 - e^{-2\alpha\delta x}\right)/2\alpha\right]^2 + \gamma^2} \\ &= -\frac{2P_{in}\gamma_1}{\omega\gamma} \frac{\xi_0 e^{-2\alpha\delta x}}{\left[\delta_0 - \xi_0\left(1 - e^{-2\alpha\delta x}\right)/2\alpha\right]^2 + 1}\end{aligned} \tag{4.7}$$

Here we define normalized static detuning $\delta_0 = \Delta_0/\gamma$ and normalized static optomechanical coupling coefficient $\xi_0 = g_0/\gamma$, normalized by the half cavity linewidth γ. We can see that the optical force exerted on the waveguide is a nonlinear function of δ_0 and $\delta x = x - x_0$ which is the signal waveguide's displacement. The nonlinear behavior of

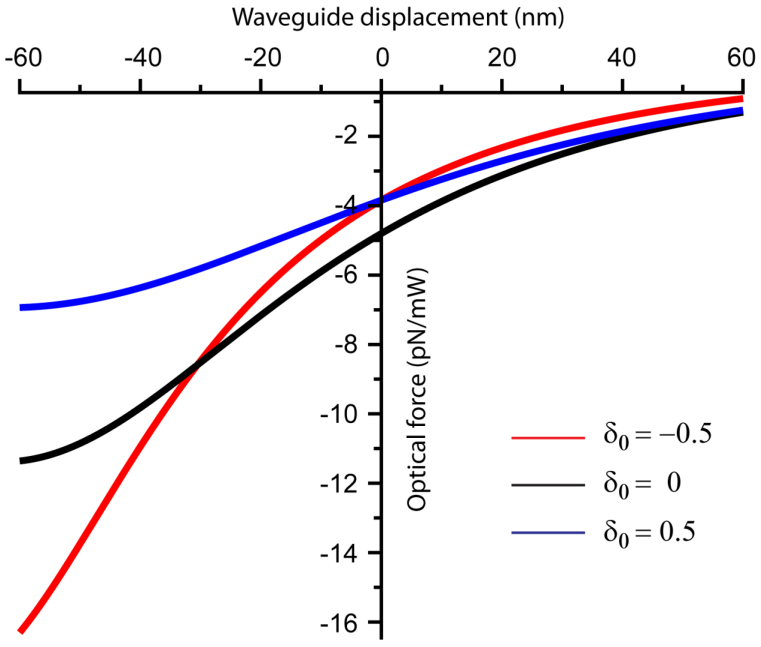

Fig. 4.11. Nonlinear behavior of the optical force.

Calculated optical force (normalized by the input power at the control channel) versus the signal waveguide displacement for different normalized static detuning values, showing strong nonlinearity.

the optical force can be seen in the plot of F_c versus δx for different values of δ_0 in Fig. 4.11, assuming the independently determined values of the parameters listed in Table 4.1.

We then expand Eq. (4.7) at the waveguide's static position $x = x_0$ to the third order of the waveguide displacement as:

$$F_c(x) = F_c(x_0) + k_1 \delta x + k_2 \delta x^2 + k_3 \delta x^3 + O(\delta x^4) \tag{4.8}$$

Thus, the coefficient k_1 is the force constant corresponding to the optical spring effect, k_2 and k_3 are the quadratic and cubic nonlinear coefficients, respectively. Their expression can be derived from the Taylor expansion of (4.7) and written in the form of polynomials of the normalized static detuning δ_0:

Table 4.1. Parameters used to calculate the theoretical values.

Symbol	Parameter	Value	Source
ω	Optical frequency	$2\pi\times1.94\times10^{14}$ Hz	Experiment
ω_c	Optical resonance frequency	$2\pi\times1.94\times10^{14}$ Hz	Experiment
g_0	Optomechanical coupling coefficient	$2\pi\times11.3$ MHz/nm	Experiment
Q	Optical quality factor	5×10^4	Experiment
γ	Optical damping rate ($=\omega_c/2Q$)	$2\pi\times1.94\times10^9$ Hz	Experiment
γ_1	Waveguide coupling rate ($=\gamma/2$ for critical coupling)	$2\pi\times9.68\times10^8$ Hz	Experiment
α	Evanescent field decay constant	1/95 nm^{-1}	Simulation
m_{eff}	Effective modal mass (=0.24×cantilever mass)	1.14 pg	Device fabrication

$$k_1 = \frac{4P_{\text{in}}\gamma_1\xi_0}{\omega\gamma}\frac{\alpha(1+\delta_0^2)-\xi_0\delta_0}{(1+\delta_0^2)^2} \tag{4.9}$$

$$k_2 = \frac{P_{\text{in}}\gamma_1\xi_0}{\omega\gamma\left(1+\delta_0^2\right)^3}\left[\begin{array}{l}\left(2\xi_0^2-4\alpha^2\right)+12\xi_0\alpha\delta_0 \\ -\left(6\xi_0^2+8\alpha^2\right)\delta_0^2+12\xi_0\alpha\delta_0^3-4\alpha^2\,\delta_0^4\end{array}\right] \tag{4.10}$$

$$k_3 = \frac{P_{\text{in}}\gamma_1\xi_0}{\omega\gamma\left(1+\delta_0^2\right)^4}\left[\begin{array}{l}\left(-8\xi_0^2\alpha+\frac{8}{3}\alpha^3\right)+\left(8\xi_0^3-\frac{56}{3}\xi_0\alpha^2\right)\delta_0 \\ +\left(16\xi_0^2\alpha+8\alpha^3\right)\delta_0^2-\left(8\xi_0^3+\frac{112}{3}\xi_0\alpha^2\right)\delta_0^3 \\ +\left(24\xi_0^2\alpha+8\alpha^3\right)\delta_0^4-\frac{56}{3}\xi_0\alpha^2\delta_0^5+\frac{8}{3}\alpha^3\delta_0^6\end{array}\right] \tag{4.11}$$

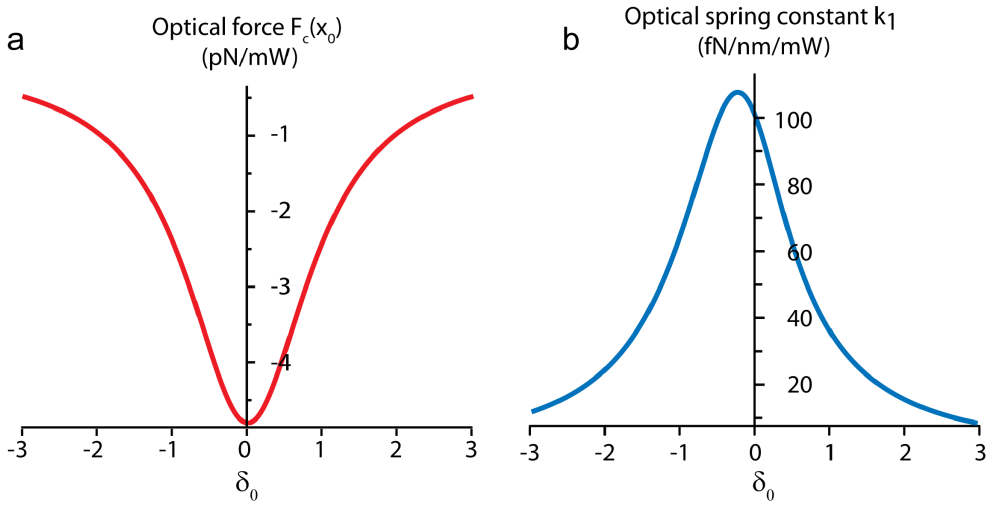

Fig. 4.12. Static optical force and optical spring constant.

Calculated static optical force $F_c(x_0)$ (a) and optical spring constant k_1 (b) of our device, normalized to the control channel power, as a function of normalized static detuning.

In Fig. 4.12a and Fig. 4.12b, we plot the static optical force $F_c(x_0)$ and the optical spring constant k_1 versus normalized static detuning δ_0 for our device using independently determined parameters listed in Table 4.1.

4.7. Theoretical Analysis of Tunable Duffing Nonlinearity

The cantilever waveguide can be modeled as a nonlinear oscillator driven by the optical force with quadratic and cubic nonlinearities. Its equation of motion is that of a typical Duffing oscillator:

$$\frac{d^2(\delta x)}{dt^2} + \mu \frac{d(\delta x)}{dt} + \omega_m^2 \delta x + \alpha_2 \delta x^2 + \alpha_3 \delta x^3 = \frac{f(t)}{m_{eff}} \tag{4.12}$$

Here m_{eff} is the effective modal mass of the cantilevered signal waveguide; $\mu = \omega_m / Q_m$ is the mechanical damping coefficient; $f(t)$ is the harmonic time-varying driving force generated by the modulated optical power; $\omega_m^2 = \omega_{m0}^2 - k_1 / m_{eff}$ is the modified mechanical resonance frequency taking into account the optical spring constant k_1. α_2 and α_3 are the quadratic and cubic nonlinear coefficients. They are given by:

$$\alpha_2 = -\frac{k_2}{m_{eff}} \ , \ \alpha_3 = -\frac{k_3}{m_{eff}} \tag{4.13}$$

In our system, the nonlinear coefficients α_2 and α_3 are dominated by the optomechanically induced nonlinearity instead of the intrinsic mechanical nonlinearity, because the vibration amplitude of our device is limited to less than 132 nm, which is much

less than the critical amplitude (~1 μm) of the device's intrinsic mechanical nonlinearity. The calculated results of α_2 and α_3 of our device are shown in Fig. 4.13a and Fig. 4.13b using Eq. (4.10), Eq. (4.11) and Eq. (4.13) with independently determined parameters as listed in Table 4.1. The same calculated result of α_3 is plotted with the experimental results in Fig. 4.5a.

The nonlinear effect due to the quadratic term induces sub-harmonic and super-harmonic resonances. But to the primary resonances, the main effect of the quadratic term is a modification to the effective Duffing coefficient in the oscillator's frequency response curve as [84]:

$$\alpha = \alpha_3 - 10\alpha_2^2 / \omega_m^2 \tag{4.14}$$

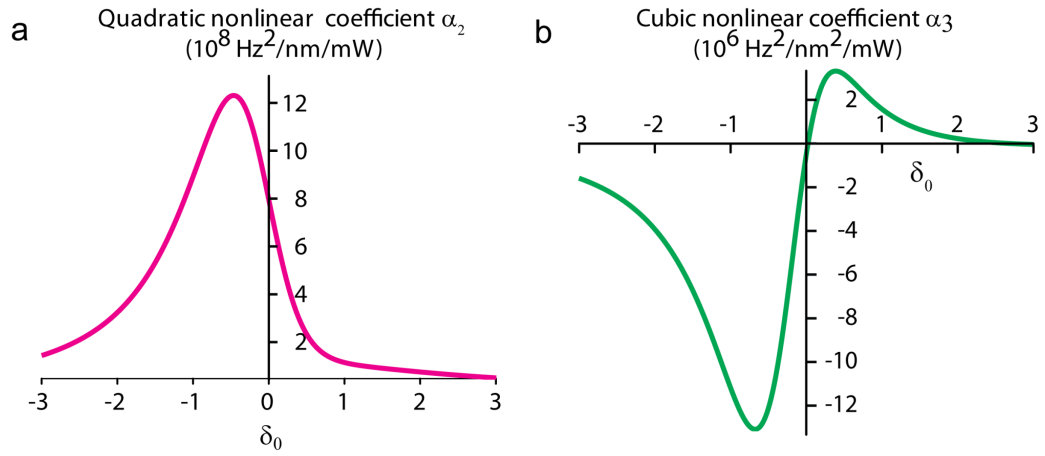

Fig. 4.13. Quadratic and cubic nonlinear coefficients.

Calculated quadratic (a) and cubic (b) nonlinear coefficients (α_2 and α_3) of our device, normalized to the control channel power, as a function of normalized static detuning.

However, in our device and with the conditions used in the measurement, the modification term $10\alpha_2^2/9\omega_{\mathrm{m}}^{-2}$ is orders of magnitude smaller than the value of α_3 (compare Fig. 4.13a and Fig. 4.13b), except for at the static detuning value when α_3 vanishes. The result is a minor shift of the detuning value for zero nonlinearity, which is below our measurement uncertainty and thus cannot be discerned in our experiment. Therefore we neglect the effect of quadratic nonlinear term in our analysis and omit the subscript 3 of α_3 for conciseness.

Duffing equation of nonlinear oscillators has been analyzed with the method of multiple scales [84]. The amplitude-frequency response curve of a Duffing oscillator can be expressed in an implicit form:

$$\left[\frac{\mu^2}{4}+\left(\sigma-\frac{3\alpha}{8\omega_{\mathrm{m}}}a^2\right)^2\right]a^2=\frac{f^2}{4m^2\omega_{\mathrm{m}}^2} \tag{4.15}$$

Here $\sigma=(\omega-\omega_{\mathrm{m}})/\omega_{\mathrm{m}}$ is the normalized detuning of the harmonic driving force frequency ω to the modified mechanical resonance frequency ω_{m}. With the increasing driving force, the resonance amplitude increases but leans towards higher or lower frequency side depending on the sign of α, as shown in the experimental results shown in Fig. 4.4a and Fig. 4.4b.

The peak amplitude and the frequency at which the peak amplitude is reached have a simple relation:

$$\sigma_{\mathrm{peak}}=\frac{3\alpha}{8\omega_{\mathrm{m}}}a_{\mathrm{peak}}^2 \tag{4.16}$$

This relation between σ_{peak} and a_{peak} is called the "backbone curve". To experimentally determine the cubic nonlinear coefficient α and its relation to the laser static detuning, we measure the amplitude-frequency response of the device at each laser static detuning value, with increasing modulated control laser power (in at least five steps) to increase the vibration amplitude, as shown in Fig. 4.4a and Fig. 4.4b. We then find the peak amplitude a_{peak} and the corresponding detuning σ_{peak}, and fit the result with the backbone curve as given by Eq. (4.16). The standard error given by the fitting result is used as the uncertainty and plotted as error bars in Fig. 4.5a and Fig. 4.5b.

4.8. Calibration of Displacement Measurement

The displacement measurement in this paper consistently refers to the lateral (or in-plane) displacement of the free end of the cantilevered signal waveguide. For clarity, in this section, the signal channel transmission and its noise power spectral density (PSD) are always normalized to the transmission value when the waveguide is not displaced. We define signal channel responsivity as the ratio between the change of the normalized transmission and the waveguide's lateral displacement:

$$\Re = \frac{1}{T_0}\frac{\partial T}{\partial x} \tag{4.17}$$

We calibrate the responsivity with two methods independently and the results agree well. The first method was the widely employed thermomechanical noise measurement. With no laser sent into the control channel, the signal laser at constant power level and

arbitrary off-resonance wavelength was sent into the signal channel. The noise PSD of the transmitted signal laser was measured with a photodetector and a spectrum analyzer. The Fig. 4.14 shows the normalized noise PSD near the resonance frequency of the cantilever, with a signal laser wavelength of 1555.75 nm. On resonance, the displacement noise PSD of the cantilever is expected to be $S_z = (4k_B T Q_m)/(k\omega_{m0})$, where k_B is the Boltzmann constant, $T = 300\text{K}$ is the absolute temperature in the lab, $Q_m = 1.6\times10^4$ is the mechanical quality factor, $\omega_{m0} = 2\pi\times(1.242\text{MHz})$ is the angular mechanical resonance frequency and

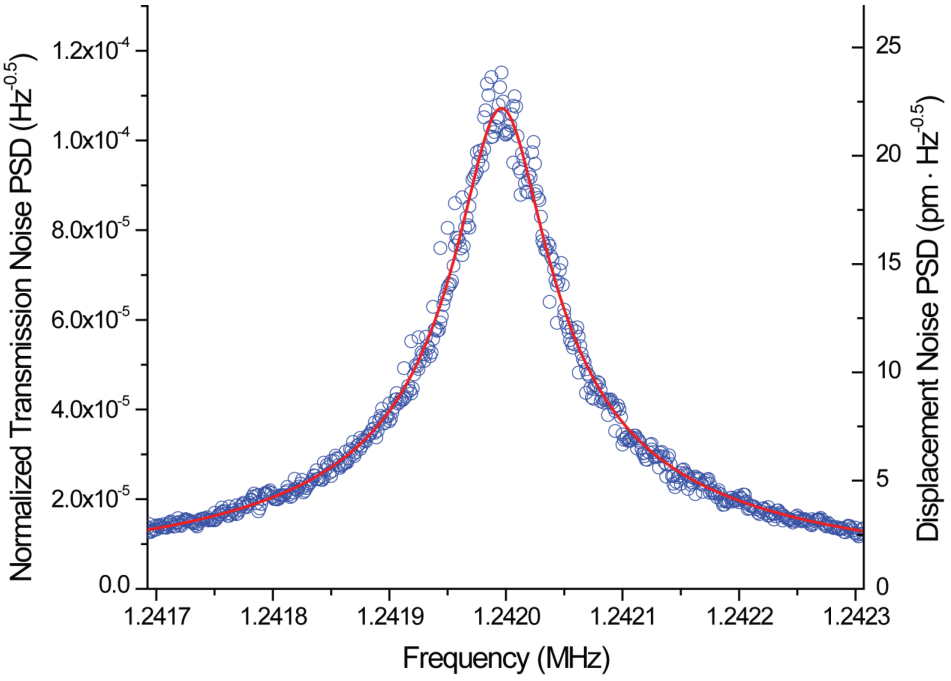

Fig. 4.14. Transmission and displacement noise PSD.

The measured normalized transmission noise PSD from the signal channel and the expected displacement noise PSD.

$k = 6.94\times10^{-2}\,\mathrm{N\cdot m^{-1}}$ is the point load spring constant. Q_{m} and ω_{m0} are obtained by fitting the noise PSD shown in Fig. 4.14 with a Lorentzian peak, while k is calculated using the standard equation of a cantilever. The expected peak displacement noise PSD $S_{\mathrm{z}} = 4.92\times10^{-22}\ \mathrm{m^2\cdot Hz^{-1}}$ corresponds to the measured peak normalized transmission noise PSD $P_{\mathrm{max}}^{\mathrm{norm}} = 1.15\times10^{-8}\ \mathrm{Hz^{-1}}$ obtained from Fig. 4.14. Therefore the responsivity is calibrated to be $\Re = \left(P_{\mathrm{max}}^{\mathrm{norm}} / S_{\mathrm{z}}\right)^{0.5} = 4.83\ \mu\mathrm{m^{-1}}$.

The maximal displacement that the signal waveguide can reach is limited by the 120 nm sized gap between the waveguide and the micro-disk. This provides the second method to independently calibrate the displacement measurement at the large amplitude regime. Determined from the geometry of the device and the mode profile of the cantilever resonance, the maximal displacement of the tip of the cantilevered waveguide is 132 nm, as is illustrated in Fig. 4.15. The strong optical force applied by the micro-disk cavity on the signal waveguide is sufficient to drive the signal waveguide to reach this maximal amplitude and be stopped by the micro-disk. The Fig. 4.15 shows the time-domain signal measured with increasing vibration amplitude. At high amplitude, the sinusoidal waveform shows a flattened bottom, indicating that the waveguide is hitting the side wall of the micro-disk. Thus, the transmission value at the flattened amplitude is 0.474, corresponding to a displacement of 132 nm at the tip of the cantilevered waveguide. Hence the responsivity is evaluated to be $\Re = (1-0.474)/(132\mathrm{nm}) = 3.98\ \mu\mathrm{m^{-1}}$. The discrepancy with the value calibrated with thermomechanical noise measurement method is due to the nonlinear

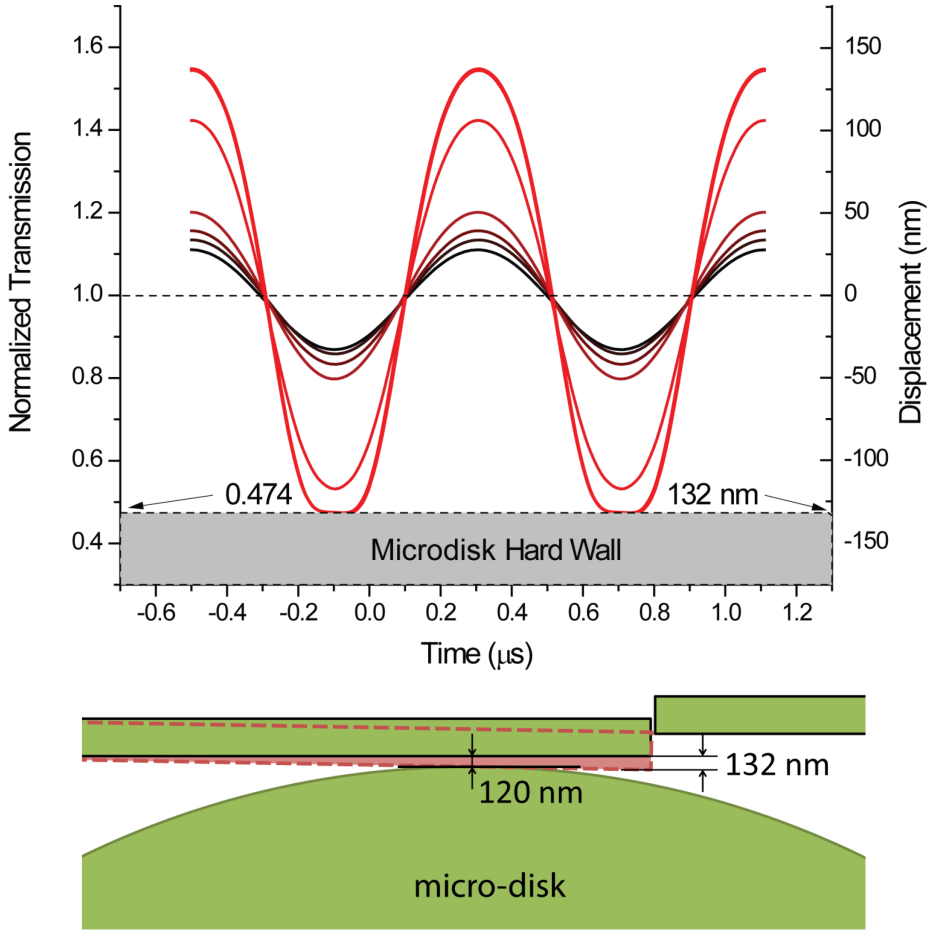

Fig. 4.15. Time-domain traces of the transmitted signal in the signal waveguide.

Time-domain traces of the transmitted signal in the signal waveguide with increasing vibration amplitude. The waveguide eventually hit the micro-disk and the amplitude is limited by the 120 nm sized gap, as indicated by the flattened bottom in the trace. The maximal displacement at the tip of the cantilever is determined to be 132 nm as an additional calibration to the displacement measurement.

response of the waveguide transmission at high amplitude, as explained in Section 4.9. It is interesting to note that there is no pull-in effect like that in electrostatic-ly actuated MEMS devices because optical force decreases when the waveguide touches the micro-

disk, due to the reduction of the optical Q and strong coupling. The mechanical spring of the waveguide is also large enough so that it will not stick to the micro-disk due to surface forces.

4.9. Cantilevered Signal Waveguide Design

The signal waveguide is designed with a gap between the free end of the cantilevered section and the receiving end of the fixed section. In addition, to detect the cantilever waveguide's lateral (or in-plane) motion, a lateral offset between the waveguide ends is also needed. The transmission through the cantilevered signal waveguide has been numerically analyzed with Finite Difference Time Domain (FDTD) simulations, which is a rigorous treatment that takes into account the mode evolution during the propagation through the gap, the coupling from the gap back to the receiving waveguide and all the reflections that occur in this process. We studied three different cases: 400 nm, 420 nm and 500 nm wide waveguides. The simulation results are shown in Fig. 4.16, suggesting that 500 nm wide waveguide has the steepest slope on both sides of the curve and 400 nm wide the least steep. 420 nm wide waveguide was eventually chosen based on various considerations, especially the trade-off between a softer cantilever and more sensitive transduction. In order to achieve the most linear transduction in a large displacement range, we designed the initial lateral offset to be 250 nm, which is almost in the center of the linear part of the transmission curves (shaded areas in Fig. 4.16). In the actual device, the displacement was limited by the fixed gap between the cantilever and the disk resonator

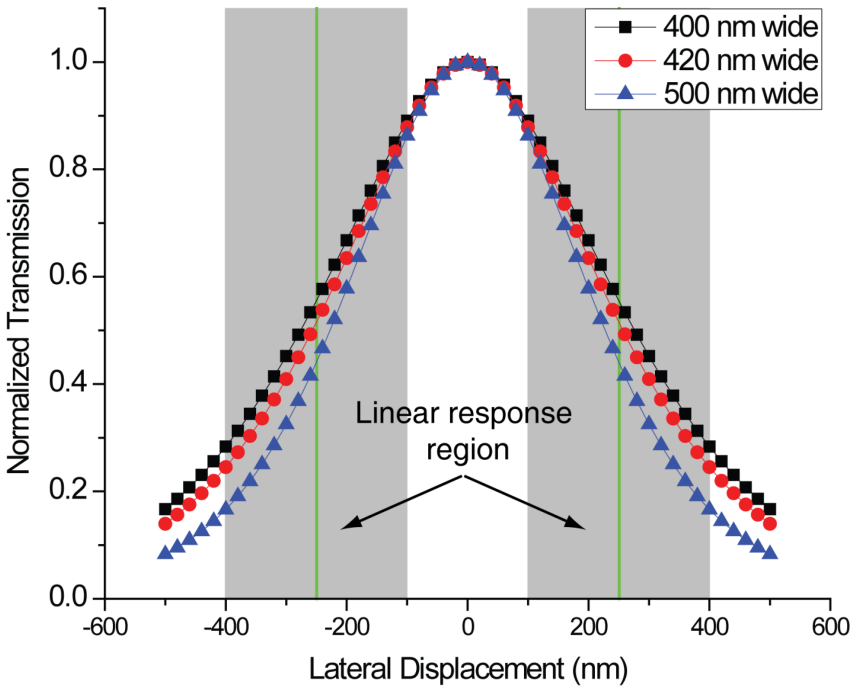

Fig. 4.16. FDTD simulation results for the cantilevered signal waveguide design.

For each waveguide width, the maximum transmission was normalized to 1 for convenient comparison. The green vertical lines indicate the 250 nm and -250 nm displacement and the shaded areas in the background shows the approximately linear transduction regime for the 400 nm and 420 nm cases.

hence never exceeded 132 nm towards the disk and 140 nm away from the disk (see Fig. 4.15), so the cantilevered signal waveguide remains in the approximately linear transduction regime even when being driven to the highest amplitude. Nevertheless, the imperfection in the linearity still leads to the discrepancy between the values of responsivity calibrated by the two methods described in Section 4.8. The receiving waveguide is designed to be farther away from the disk than the cantilever, so the

transmission increases (decreases) when the cantilever moves away from (towards) the disk.

4.10. Experimental Calibration of g Factor

The optomechanical coupling coefficient or the *g* factor is one of the most important parameters of cavity optomechanical systems. We experimentally determine the *g* factor by measuring the thermomechanical noise of the device using the slope detection method. In the experiment, a probing laser at constant power is sent into the control channel and tuned on the slope of the resonance dip in the transmission spectrum (see Fig. 4.2). The thermomechanical vibration of the cantilever dispersively perturbs the disk resonance introducing amplitude noise in the transmitted probing laser power, which was measured by a photodetector and a spectrum analyzer. The *g* factor can be determined experimentally using the following equation:

$$|g| = \left|\frac{\partial \omega_c}{\partial x}\right| = \left(\frac{2\pi c}{\lambda_{Prob}^2}\right)\left|\frac{dT}{d\lambda}\right|_{\lambda_{Prob}}^{-1}\frac{\sqrt{S_v/S_z}}{P_{Prob}G} \tag{4.18}$$

where S_v is the measured voltage noise power spectral density (PSD), S_z is the expected cantilever displacement noise PSD which is described in Section 4.8, P_{Prob} is the probing laser power, G (in V/W) is the transduction gain factor of the photodetector, c is the light velocity in vacuum, λ_{Prob} is the probing laser wavelength, $T(\lambda)$ is the measured transmission spectrum of the resonance through the control channel, including the input

and output grating couplers, its derivative with respect to λ ($dT/d\lambda$) is estimated by linear curve fitting near the probing laser wavelength. The experimentally determined values of the *g* factor are listed in Table 4.2 for the modes labeled in Fig. 4.2.

4.11. Theoretical Calculation of g Factor

In order to theoretically calculate the optomechanical coupling coefficient, or the *g* factor, we first used Finite-Element-Method (FEM) to calculate the Whispering Gallery Mode (WGM) profiles $\vec{E}(\vec{r})$ of the disk resonator without control or signal waveguide, so that

Table 4.2. Parameters used to calculate the theoretical values.

Mode profile $\lvert E_r\rvert^2$	Mode number (p, m)	$g_{exp}/2\pi$ (MHz/nm)	$g_{theory}/2\pi$ (MHz/nm)	V_{mode} (μm^3)
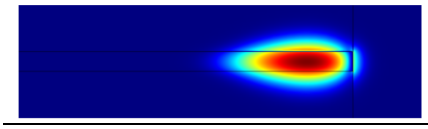	(1,105)	2.30	1.40	39.5
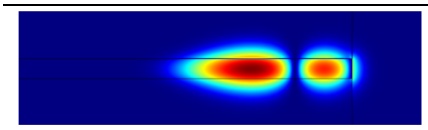	(2,99)	N.A.	1.89	47.7
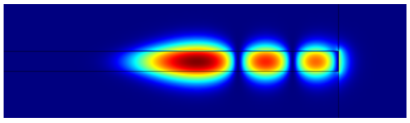	(3,94)	2.15	2.88	57.0
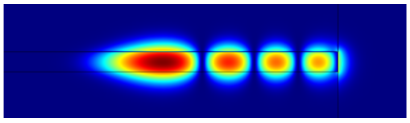	(4,89)	11.3	14.3	65.4
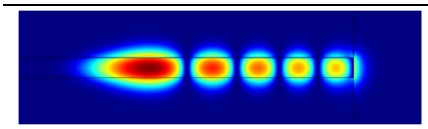	(5,85)	3.39	1.65	74.5

we could take advantage of the axisymmetry of the disk resonator to simplify the large scale 3D problem into a 2D problem [80]. Subsequently we employed a perturbation treatment derived from energy considerations [98] to take into account the resonance frequency shift induced by the existence of the nearby waveguide and its motion:

$$\frac{\Delta\omega_c'(\delta x)}{\omega_c'} = -\frac{1}{2}\frac{\iiint_{V_{\text{Cant}}(\delta x)}\left[\varepsilon(\vec{r})-1\right]\left|\vec{E}(\vec{r})\right|^2 d^3\vec{r}}{\iiint_V \varepsilon(\vec{r})\left|\vec{E}(\vec{r})\right|^2 d^3\vec{r}} \tag{4.19}$$

where $\varepsilon(\vec{r})$ is the dielectric constant, ω_c' is the resonance frequency without waveguides nearby, $\Delta\omega_c'(\delta x)$ is the resonance frequency shift with respect to ω_c' when the cantilever displacement is δx, $V_{\text{Cant}}(\delta x)$ is the volume of the cantilever when the cantilever displacement is δx and V is the entire space. The *g* factor when the cantilever is at its original position can be derived as:

$$g = \left.\frac{d(\Delta\omega_c')}{d(\delta x)}\right|_{\delta x=0} \tag{4.20}$$

In Eq. (4.19), ω_c' was solved in the FEM simulation and the integrals on the right hand side were calculated numerically from the simulation results. The derivative in Eq. (4.20) was also calculated numerically by five point method. The calculation results agree reasonably well with the experimentally calibrated g factors, as listed in Table 4.2.

Mode volume is another important characteristic of resonance modes. It is defined as [80]:

$$V_{\text{mode}} = \frac{\iiint_V \varepsilon(\vec{r})\left|\vec{E}(\vec{r})\right|^2 d^3\vec{r}}{\max\left[\varepsilon(\vec{r})\left|\vec{E}(\vec{r})\right|^2\right]} \tag{4.21}$$

where $\max[\cdots]$ denotes the maximum value of its functional argument. The numerically calculated mode volumes are also included in Table 4.2. We note that the TE mode (4, 89), which our experiment focuses on, has a particularly high *g* factor because of the good phase-matching with the waveguide mode.

Chapter 5. Optomechanical Photon Shuttling Between Photonic Cavities [29]

Mechanical motion of photonic devices driven by optical forces provides a profound means of coupling between optical fields. The current focus of these optomechanical effects has been on cavity optomechanics systems in which co-localized optical and mechanical modes interact strongly to enable wave mixing between photons and phonons, and backaction cooling of mechanical modes. Alternatively, extended mechanical modes can also induce strong non-local effects on propagating optical fields or multiple localized optical modes at distances. Here, we demonstrate a multicavity optomechanical device in which torsional optomechanical motion can shuttle photons between two photonic crystal nanocavities. The resonance frequencies of the two cavities, one on each side of this 'photon see-saw', are modulated antisymmetrically by the device's rotation. Pumping photons into one cavity excites optomechanical self-oscillation, which strongly modulates the inter-cavity coupling and shuttles photons to the other empty cavity during every oscillation cycle in a well-regulated fashion.

5.1. Introduction

Photonic cavities are indispensable components in integrated optical systems as buffers or registers to trap and store photons for processing both classical and quantum information

[99]–[102]. To achieve advanced optical functions, it is often necessary to couple multiple cavities so that photons can be exchanged between them to achieve signal processing and computational operation [103]–[106]. Two cavities in proximity couple evanescently so that photons in one cavity can spontaneously couple to the other cavity with a coupling rate determined by the spatial overlap of the optical modes of both cavities. From the perspective of optical signal processing, however, it is desirable to couple cavities that are separated far enough that each cavity can be controlled individually and the exchange of photons between them can be regulated. For example, two cavities can be coupled to a common bus waveguide to achieve a strong-enough coupling to cause photon number Rabi oscillation between the two; modulation of intercavity coupling can be achieved by detuning one of the cavities via the optical injection of carriers [107].

Recently, optical forces in nano-optomechanical systems have been exploited as a new means of controlling the coupling between optical modes in various nanophotonic systems [9], [10], [16], [19], [20], [47], [51], [60], [70], [71]. In particular, cavity optomechanics explores the interactions between the cavity optical modes and the localized mechanical modes, such as the vibration of a mirror in a Fabry–Perot cavity [13]–[15], [75], [82], [108], and the bulk and surface acoustic modes in whispering gallery resonators and photonic crystal cavities [11], [18], [109], [110]. In these systems, there is only one optical cavity, although multiple optical modes of the cavity have been utilized to induce the optomechanical effects. Meanwhile, multiple mechanical modes can also be synchronized through their optomechanical coupling with one cavity mode [25], [111].

More recently, coupling between two Fabry–Perot cavities mediated by the mechanical motion of a nanomembrane between them was studied theoretically [112]. In most of the systems mentioned above, however, the involved mechanical modes are highly localized compared to the spatial extent of the optical modes: the mechanical motion only perturbs a portion of the optical mode of the cavities. If, instead of localized mechanical modes, an extended mechanical mode that simultaneously interacts with multiple cavities can be exploited, intriguing cavity optomechanical effects can emerge. In this work, we

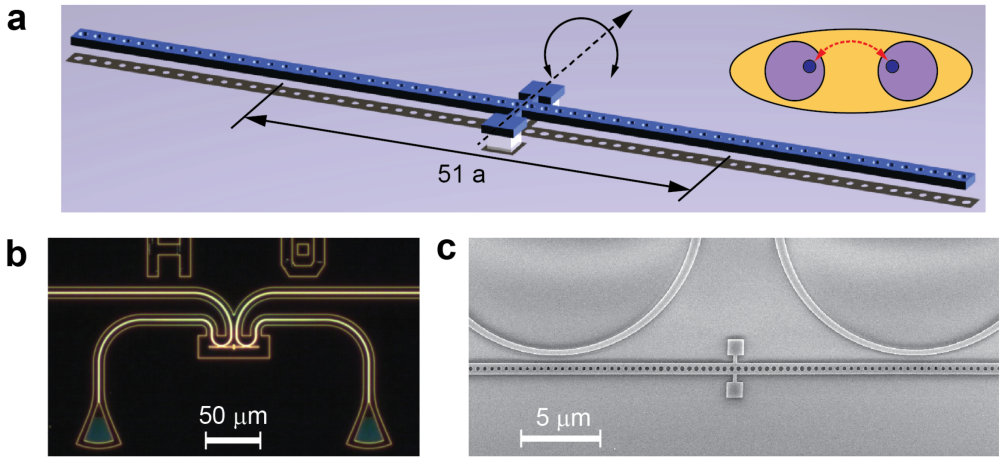

Fig. 5.1. Photon see-saw oscillator.

a, Artistic illustration of the photon see-saw oscillator consisting of a suspended nanobeam inscribed with two photonic crystal cavities, one on each side; a = 450 nm is the lattice constant of the photonic crystal. For better visualization, this illustration is not to the scale of the actual device, which consists of 102 air holes in total. The labelled distance between the centres of both sides of the nanobeam is consistent with that of the actual device, but not with the illustration. Inset: The torsional mechanical mode (yellow) extends to and couples two cavity optical modes (purple). **b**, Darkfield optical microscope image of the device taken after the nanobeam was released, showing the integrated grating couplers connected to the coupling waveguides. **c**, SEM image of the device taken before the nanobeam was released, showing the two waveguides coupled with the two cavities separately.

demonstrate a novel torsional multicavity optomechanical system, which we name a 'photon see-saw', as depicted in Fig. 5.1a. The photon see-saw consists of a nanobeam inscribed with two one-dimensional (1D) photonic crystal nanocavities, one on each side. The optical force generated by photons inside the nanocavities excites rotational motion of the nanobeam, which antisymmetrically modulates the frequencies of both nanocavities. With this device, we demonstrate optomechanical modulation of the coupling between the two nanocavities and the photon-shuttling effect in the side-band unresolved regime. Our work focuses on the well-regulated transfer of photons in small amounts (potentially and ultimately at the single-photon level), and represents an important first step towards the side-band resolved regime, in which a wealth of intriguing photon dynamics can be explored [112].

5.2. Photon See-Saw Oscillator

Instead of the commonly used dielectric resonant modes, the two 1D photonic crystal nanocavities are designed identically to resonate in the fundamental air mode (Fig. 5.2a) (effective mode index $n_{\text{eff}} = 1.71$), which enables stronger coupling with the substrate and, consequently, a higher optomechanical coupling coefficient [113], [114]. (The design of the photonic crystal nanocavity is discussed in Section 5.8.) On the mechanical design, the nanobeam is suspended on two axial spokes anchored to the substrate. The nanobeam can oscillate as a torsional resonator driven by the optical force generated by photons in either of the two cavities. Very unique in this torsional cavity optomechanics device is that the

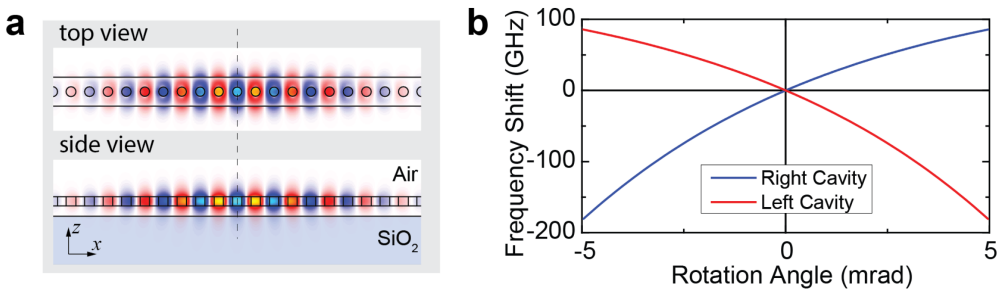

Fig. 5.2. Photonic crystal cavity simulation results.

a, Finite-difference time-domain simulation-generated field amplitude plot (top and side views) of the air mode of the nanobeam photonic crystal cavity. The side view shows the mode field penetrating into the substrate to induce strong optomechanical coupling. The dashed line indicates the centre of the cavity. **b**, Simulated relative frequency shift of the left and right cavities versus the rotation angle of the see-saw. The angular optomechanical coupling coefficients of the two cavities have opposite signs.

rotation of the nanobeam as an extended mechanical mode couples the two nanocavities dispersively in an antisymmetric way: when the nanobeam rotates such that one side of it approaches the substrate, the cavity on the same side will experience a resonance red shift because of the increased coupling with the substrate, and the resonance of the other cavity on the opposite side will be blue shifted because of the decreased coupling with the substrate. This antisymmetric optomechanical effect is manifested in Fig. 5.2b, in which the resonance frequencies of the left and right cavities are simulated with a varying rotation angle of the nanobeam. The linear and angular optomechanical coupling coefficients of the cavity ($g_{\mathrm{OM}} = d\omega_{\mathrm{c}}/dz$ and $g_{\mathrm{OM}}^{\mathrm{A}} = d\omega_{\mathrm{c}}/d\theta = g_{\mathrm{OM}} \cdot l$, where l is the distance from the centre of the cavity to the rotation axis of the nanobeam and ω_{c} is the angular frequency of the

cavity resonance) are calculated to be $2\pi \times 2.13$ GHz nm^{-1} and $2\pi \times 24.5$ GHz mrad^{-1}, respectively, at zero rotation angle. As the torsional mode is very compliant (effective spring constant $k = 0.11$ N m^{-1}), the cavity resonance frequency shift induced by a single photon, given by $\delta\omega_c = \hbar g_{OM}^2 / k = 2g_0^2 / \Omega_m = 2\pi \times 27$ kHz (g_0 is the vacuum optomechanical coupling strength and Ω_m is the angular frequency of the mechanical resonance) is among the highest in cavity optomechanics systems demonstrated so far [10] and thus the design is favourable to achieving efficient optomechanical tuning of the cavity modes.

The photon see-saw device was fabricated on a standard silicon-on-insulator (SOI) substrate with a 220 nm thick top silicon layer and a 3-μm-thick buried oxide (BOX) layer. After patterning the device with electron-beam lithography and dry etching, the nanobeam was released selectively from the substrate by wet etching the BOX layer using hydrofluoric acid. The Fig. 5.1b shows the optical microscope image after the nanobeam was released, whereas Fig. 5.1c shows the scanning electron microscope (SEM) image, taken before the release to prevent the collapse of the nanobeam owing to electrostatic charging induced in the SEM. Each of the two cavities is coupled with a waveguide, which allows them to be characterized independently. To avoid overloading the cavity, the gap between the photonic crystal cavities and the waveguides is designed to be 500 nm, much larger than the 250 nm gap between the cavities and the substrate. Therefore, the optomechanical coupling between the cavity and the waveguide is negligible compared to

that between the cavity and the substrate, which dominates the optomechanical effects in the device. Consequently, the out-of-plane motion driven by the substrate-coupled optical forces dominates the in-plane motion induced by the waveguide-coupled optical forces. In the transmission spectra measured from the two waveguides (Fig. 5.3), the resonance modes of the two nominally identical cavities are shown to be very close in wavelength (left, $\lambda_{L0} = 1541.574$ nm; right, $\lambda_{R0} = 1541.219$ nm) with a detuning of $2\pi \times 44.8$ GHz. They also have similar quality factors (waveguide loaded, $Q_L \approx 1.0\times10^4$, intrinsic, $Q_i \approx 1.6\times10^4$), which are significantly lower than the simulated value ($Q \approx 10^6$) because of fabrication non-idealities. The two cavities are separated by a long distance of 23 μm, equivalent to about 50 optical wavelengths in silicon. Therefore, the coupling rate between the two cavities is very low ($\kappa \approx 2\pi \times 0.72$ GHz) and thus the resonance mode of the right cavity is not observed in the spectrum measured from the left cavity and vice versa.

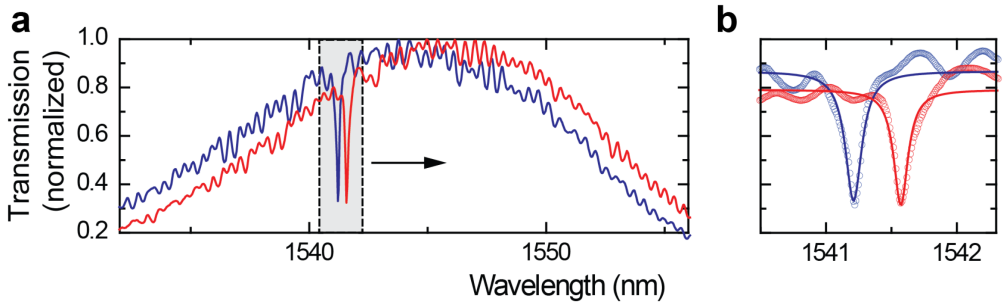

Fig. 5.3. Transmission spectra of the two cavities.

a,**b**, Broad (**a**) and narrow (**b**) band transmission spectra of the two cavities. The loaded optical quality factors are ~1.0×10^4.

5.3. Impulse Response Experiment

To investigate the mechanical and optomechanical properties of the device, we first employed an impulse-measurement technique. One laser tuned to the resonance of the left cavity and modulated with a pulse generator was sent to the left cavity and used as a pulsed pump with an effective pulse width of ~10 ns and peak power level of ~4 mW. Another continuous wave (CW) probe laser was input to the right cavity with varying detuning δ_b relative to the right cavity's initial resonance, and a low, fixed power level of ~30 nW; its transmission through the device was monitored in the time domain so that the mechanical motion of the torsional nanobeam was read out with such a slope-detection scheme. The

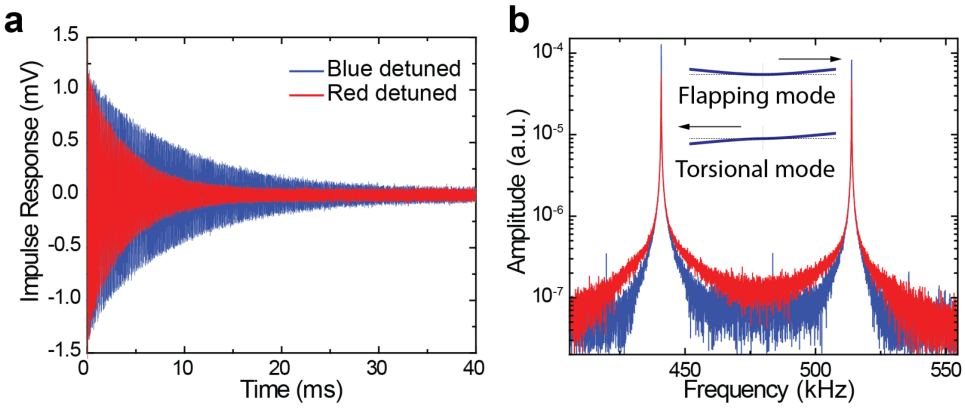

Fig. 5.4. Impulse response and photon see-saw effect. (Part 1.)

a, Impulse response measured in vacuum when a pump pulse was sent to the left cavity and the transmission of a probe laser coupled to the right cavity monitored. The response shows fast oscillation with a ring-down time noticeably longer when the probe is blue detuned than when red detuned, which indicates the backaction cooling and amplification effects. **b**, Fourier transform spectra of the impulse responses, showing two out-of-plane mechanical modes: the torsional mode at 441 kHz and the flapping mode at 514 kHz.

Fig. 5.4a displays the measured impulse responses when the device was in vacuum (1×10^{-4} torr) and the probe laser was red or blue detuned ($\delta_b = \pm 0.8$), and shows the typical ring-down response of a mechanical resonator. The Fig. 5.4b shows the Fourier transform spectra of the time-domain signals, revealing two dominant resonance modes at $\Omega_m = 2\pi \times 441$ kHz and $2\pi \times 514$ kHz, which correspond to the fundamental torsional and flapping modes (insets, Fig. 5.4b), respectively. As expected from the design, no in-plane mechanical modes could be observed in the spectra. In Fig. 5.4a, it is obvious that the ring-down time when the probe laser is blue detuned ($\delta_b > 0$) is longer than the ring-down time when the probe laser is red detuned ($\delta_b < 0$), which indicates modified mechanical damping coefficients of both mechanical modes. This is a result of the well-known backaction cooling and amplification effects induced by the detuned probe laser, which have been investigated extensively in various cavity optomechanics systems. The intrinsic mechanical quality factors, determined independently from thermomechanical noise calibration, are 1.66×10^4 and 1.68×10^4 for the torsional and flapping modes, respectively.

Although the impulse response measurement in vacuum yields important information about the mechanical properties of the device, some interesting optomechanical effects are submerged by the fast oscillation. We next conducted the same impulse-response measurement at atmospheric pressure utilizing air damping to 'slow down' the mechanical motion, as shown in Fig. 5.5a. Immediately after the pump pulse entered the left cavity (t = 0), a positive (negative) response was observed in the output of

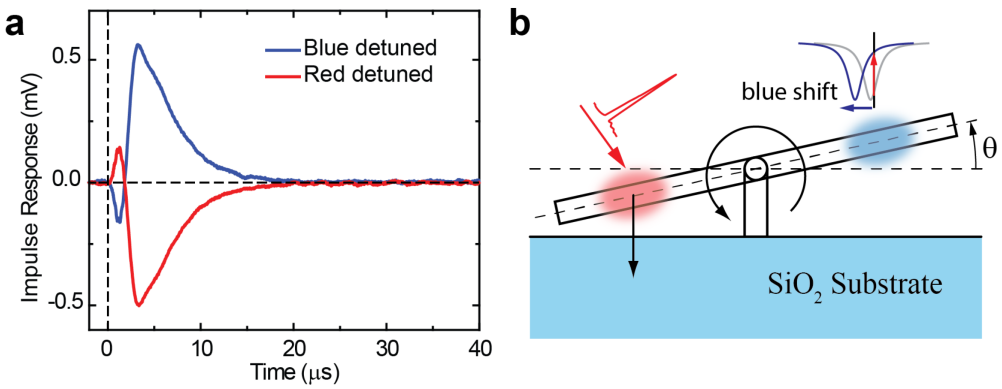

Fig. 5.5. Impulse response and photon see-saw effect. (Part 2.)

a, The impulse response measured at atmospheric pressure when fast mechanical oscillation is damped by air. **b**, The initial response (between 0 and 1.9 μs) indicates that the nanobeam rotated anticlockwise under the impulse of the pump pulse and the resonance of the right cavity was blue shifted. The later response (after 1.9 μs) is dominated by the thermo-optical effect. a.u., arbitrary units.

the probe laser red (blue) detuned from the right cavity resonance. As illustrated in Fig. 5.5b, the sign of the response indicates that an instantaneous anticlockwise rotation of the nanobeam and a consequent blue shift of the right cavity's resonance were induced by the pulse of optical force generated at the left cavity by the pump pulse. Thus, this time-domain result reveals the interesting photon see-saw effect: the photons in the left cavity outweigh the photons in the right cavity, tilt the torsional nanobeam and detune the right cavity. The see-saw response reached a peak value at 1.2 μs and started to decrease as the nanobeam recoiled back. At 1.9 μs the response changed sign and peaked with a much higher amplitude at 3.2 μs. This is because the pump pulse in the left cavity generated a heat pulse that propagated across the nanobeam to the right cavity and induced a thermo-optical red-shift of its resonance. The time scale of this event agrees well with the simulated thermal

response of the device (see Section 5.15). From this impulse-response measurement, the antisymmetric nature of the optomechanical coupling between the nanobeam's torsional motion and the optical modes of the two cavities, namely the photon see-saw effect, is clearly revealed.

5.4. Dynamics of the Cavity Resonance Frequencies During Oscillation

When the pump laser was changed to the CW mode, significant cavity optomechanical backaction effects on the torsional mode of the nanobeam resonator were induced. Here we focus on the amplification effect (the cooling effect is discussed in Section 5.14), which can excite optomechanical self-oscillation with lasing-like characteristics [24]. As a result of the very high mechanical quality factor of the torsional mode and the strong optomechanical coupling of the cavities, optomechanical self-oscillation can be triggered at a very low laser-power level. During the experiment, the pump laser power sent to the left cavity was fixed at 3.4 μW to excite stable oscillation. The probe laser coupled with the right cavity was set at a much lower power level of 2.3 nW, so its backaction effect was negligible compared to that of the pump. The Fig. 5.6 shows the time-domain traces of the transmitted probe signal when stable oscillation was excited and the initial probe laser detuning δ_b was varied from positive to negative values. When the nanobeam oscillates in the see-saw motion, the resonance frequencies of both cavities swing back and forth together, but 180° out-of-phase with each other. The time-domain trace of the probe laser transmission can provide a real-time monitor of the right cavity's resonance: minimum

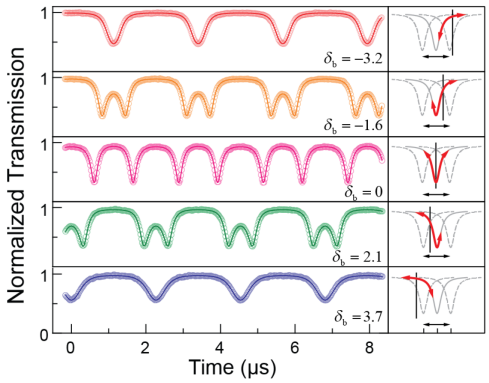

Fig. 5.6. Time-domain traces of the probe laser transmission.

Time-domain traces of the probe laser transmission (normalized) from the right cavity with varying detuning (δ_b) when optomechanical oscillation is excited by the pump laser coupled to the left cavity at a power level of 3.4 μW. The right column depicts the dynamics of the right cavity resonance (grey solid and dashed lines) and its alignment with the probe laser wavelength (black line). The black arrows show the extent to which the right cavity's resonance frequency swings during the self-oscillation, whereas the red arrows illustrate the change of the probe laser transmission during an oscillation cycle.

when its resonance swings closest to and maximum when furthest away from the probe laser wavelength. This dynamics is illustrated in the right column in Fig. 5.6.

By varying the initial probe laser detuning and fitting the measured traces with the theoretical model (Fig. 5.6, solid lines, see Section 5.16 for details), stroboscopic snapshots of the cavity resonance frequency and line shape at any moment during the oscillation cycle can be constructed. The results are shown in Fig. 5.7, in which are plotted the resonances of the left and right cavities when the nanobeam rotates to the most anticlockwise, the neutral and the most clockwise positions. From these results it is clear that, even with a modest pump power, the nanobeam can be excited into a see-saw oscillation with an

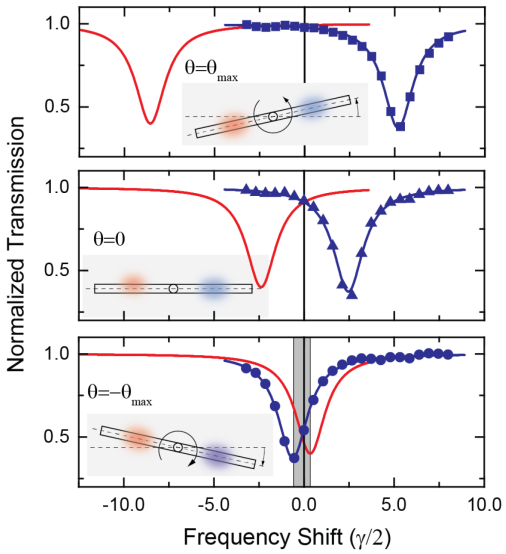

Fig. 5.7. Stroboscopic snapshots of the cavity resonances.

From the time-domain traces, stroboscopic snapshots of the cavity resonances can be constructed for the selected moments during the oscillation cycle. Shown are the positions of the resonances when the rotation angle $\theta = \theta_{max}$, 0 and $-\theta_{max}$. It can be observed that at this amplitude, the resonances of the two cavities cross over (grey box in the bottom panel) during the oscillation.

amplitude high enough such that the resonances of the two cavities can cross over each other during each oscillation cycle. In Fig. 5.8, the relative frequency shift of both cavities determined from above experiment is plotted versus the rotation angle of the nanobeam. Unlike the theoretical results (Fig. 5.2b), the actual optomechanical characteristics of the two cavities are not perfectly antisymmetric despite the identical design, which we attribute to the variance of the surface profile of the etched substrate under the suspended cavities. The result in Fig. 5.8 shows that the resonances of the two cavities align when the nanobeam is rotated to an angle of −0.7 mrad, at which strong inter-cavity coupling can occur.

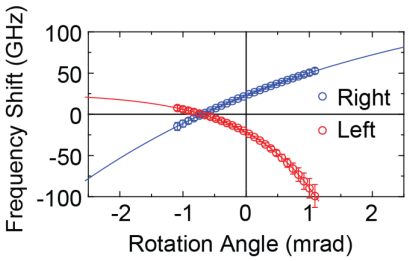

Fig. 5.8. The resonance frequencies of the two cavities.

The resonance frequencies of the two cavities versus the rotation angle of the nanobeam as determined from the above results. The imperfect antisymmetry of the behaviours of the two cavities is attributed to the non-ideal fabrication.

5.5. Photon Shuttling Experiment

We demonstrate in the following that, because of the unique photon see-saw effect and its strong modulation of the cavity resonances, photons can be optomechanically shuttled from the filled left cavity to the empty right cavity when self-oscillation with sufficient amplitude is excited. Such an optomechanical photon-shuttling effect was predicted previously in a membrane-inside Fabry–Perot cavity optomechanical system [112], which has similar antisymmetric optomechanical coupling between the two cavity modes. When the probe laser was removed and only the pump laser was on, the right cavity remained mostly empty because the inter-cavity coupling rate ($\kappa \approx 2\pi \times 0.72$ GHz) was significantly lower than the cavity photon decay rate ($\gamma_{\mathrm{L,R}} \approx 2\pi \times 19$ GHz) and the two cavities were initially detuned by $2\pi \times 44.8$ GHz. The intra-cavity photon number, n_{R} , of the right cavity is given by:

$$n_{\mathrm{R}} = \frac{\left|a_{\mathrm{R}}\right|^2}{\hbar\omega_{\mathrm{p}}} = \frac{\left(\kappa\tau_{\mathrm{R}}\tau_{\mathrm{L}}\right)^2/\tau_{\mathrm{Le}}}{\left(\delta_{\mathrm{R}}^2+1\right)\left(\delta_{\mathrm{L}}^2+1\right)}\left(\frac{P_{\mathrm{in}}}{\hbar\omega_{\mathrm{p}}}\right), \tag{5.1}$$

where a_{R} is the mode amplitude of the right cavity, ω_{p} is the angular frequency of the pump laser, δ_{R} (δ_{L}) and $\tau_{\mathrm{R}} = 2/\gamma_{\mathrm{R}}$ ($\tau_{\mathrm{L}} = 2/\gamma_{\mathrm{L}}$) are normalized laser detuning and field-decay time of the right (left) cavity respectively, τ_{Le} is the external field-decay time of the left cavity and P_{in} is the input pump laser power to the left cavity (see Section 5.17). The

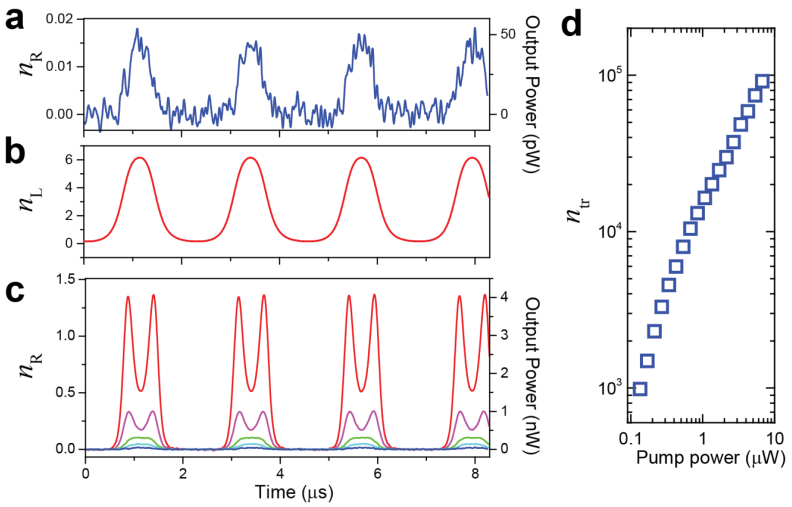

Fig. 5.9. Optomechanical photon shuttling between two cavities. (Part 1.)

a,**b**, Time-domain traces of intra-cavity photon number of the right (**a**) and left (**b**) cavities when the pump laser power is at the threshold level of 0.135 μW. Also shown on the right axis of **a** is the output power of the right cavity. **c**, Intra-cavity photon number in the right cavity when the pump laser power is 0.135 μW (blue), 0.269 μW (cyan), 0.537 μW (green), 1.70 μW (magenta) and 6.76 μW (red). The right axis is the output power of the right cavity. **d**, Total number of photons shuttled from the left to the right cavity during one oscillation cycle versus the pump laser power. The minimum is ~1,000 photons per cycle when the pump is at the threshold level.

Fig. 5.9a shows the time-domain trace of $n_{\mathrm{R}}(t)$ and the transmission out of the right cavity when P_{in} was reduced to the threshold level (~0.135 μW) of self-oscillation. It clearly shows that once per oscillation cycle a pulse of photons is shuttled from the left cavity to fill the right cavity. In between the pulses, the right cavity remains empty ($n_{\mathrm{R}} \approx 0$) because the photon decay rate is much higher than the oscillation frequency, which indicates side-band unresolved regime. At the same time the photon number in the left cavity n_{L} also oscillates because its detuning relative to the fixed pump laser frequency changes during the oscillation cycle (Fig. 5.9b). Thus, the photon number in the right cavity reaches a peak value every time the three frequencies of the left cavity resonance, the right cavity resonance and the pump laser align.

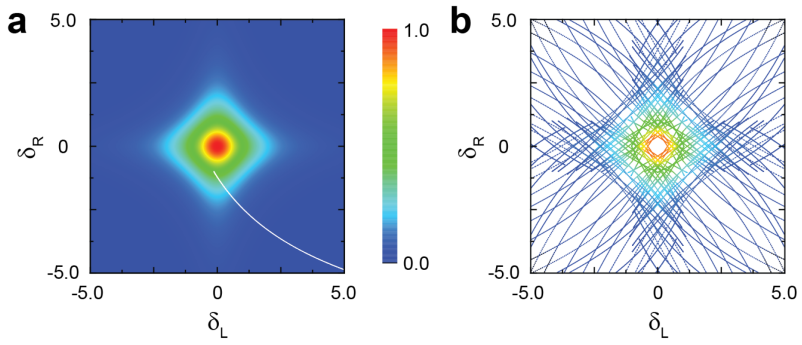

Fig. 5.10. Optomechanical photon shuttling between two cavities. (Part 2.)

a,**b**, Theoretical (**a**) and experimental (**b**) plots of the right cavity's intra-cavity photon number n_{R} (normalized to the range between 0 and 1) versus the normalized pump laser detuning relative to the left (δ_{L}) and the right (δ_{R}) cavities. The white line in **a** represents the trajectory that the system undergoes when it is oscillating at the threshold level (that is, the trace in Fig. 5.9a).

As explained in Fig. 5.6, Fig. 5.7 and Fig. 5.8, when the pump laser power increases, the oscillation amplitude grows and the resonance frequencies of the two cavities cross over during each oscillation cycle. As a result, two peaks per cycle start to appear in the time-domain trace of $n_{\mathrm{R}}(t)$, shown in Fig. 5.9c, when the pump laser power is gradually increased from 0.135 μW to 6.76 μW. The Fig. 5.9d shows that the integrated number of shuttled photons n_{tr} during an oscillation cycle increases with the pump laser power. At the threshold pump power level of 0.135 μW, ~1,000 photons are shuttled to the right cavity during each cycle. The photon-shuttling effect between two optomechanically coupled cavities can be modelled with the temporal coupled-mode theory (described in Section 5.6 and Section 5.7). In Fig. 5.10a, the calculated number of photons in the right cavity n_{R} (normalized) is plotted versus δ_{R} and δ_{L}. In Fig. 5.10b, the normalized experimental results from the time-domain traces, which were obtained when the pump laser power was fixed at 6.76 μW and its detuning was varied, are plotted as trajectories with the two cavities' detuning determined from the stroboscopic method used in Fig. 5.7 (explained in Section 5.16 and 5.17). Close agreement between theoretical model and experimental results is observed. In Fig. 5.10a, the trajectory that the system undergoes in the parameter space when it is oscillating at the threshold level (that is, the trace in Fig. 5.9a) is overlaid on the theoretical plot, which illustrates the dynamics of the photon-shuttling process.

The demonstrated modulation of inter-cavity coupling and photon shuttling between two photonic cavities are mediated only by the optomechanical self-oscillation without any external modulation. It is thus very unique to cavity optomechanics systems and unprecedented, as similar phenomena have not been realized in any other optical systems. The photon-shuttling effect can be utilized to transfer optical information between multiple cavities for optical signal processing. The concept of mechanically mediated optical coupling can be extended to many other types of mechanical motions, such as flexural plate waves and surface acoustic waves [115], to couple multiple photonic cavities over even longer ranges and in more-sophisticated ways. Furthermore, increasing the mechanical Q of the current device to reduce the threshold pump level needed to start self-oscillation meanwhile reducing the inter-cavity coupling rate (κ) can potentially achieve single-photon shuttling per mechanical cycle so that the device could find application in quantum photonics. As the first multi-cavity optomechanical system, the current device ($\Omega_{\mathrm{m}}/\gamma \simeq 2.3\times10^{-5}$) is still far from the side-band-resolved regime, which is necessary to achieve backaction cooling of the mechanical resonator to the quantum ground state and to observe other phenomena in photon–phonon dynamics [112], [116]. However, it is foreseeable that in other systems that have reached the side-band-resolved regime, such as optomechanical crystals that may consist of multiple photonic cavities [18], shuttling of single photons and inter-cavity Rabi oscillations of photons mediated by phonons is within reach. In such a regime, a wealth of quantum optomechanical effects can be expected to emerge. Finally, the photon see-saw device demonstrated here has a very high torque

detection sensitivity, determined to be 9.7×10^{-21} N m $Hz^{-0.5}$ (see Section 5.14) and can be utilized immediately as an all-optical transduced torsional magnetometer [117], [118], accelerometer [119] and gyroscope.

5.6. Temporal Coupled Mode Theory of Two Coupled Photonic Crystal Cavities

The photon dynamics and cavity optomechanics in the photon see-saw device including two coupled photonic crystal cavities can be modeled using either the classical temporal coupled mode theory or the averaged linearized quantum input-output theory. Both theories yield identical results. Here we adopt the temporal coupled mode theory [120]–[122] and the convention of using only positive frequencies.

The cavity modes and the coupling between them and with the waveguides in the device are depicted in Fig. 5.11. The field amplitudes of the incoming and outgoing waveguide modes are denoted with "s", while the field amplitudes of the cavity modes are

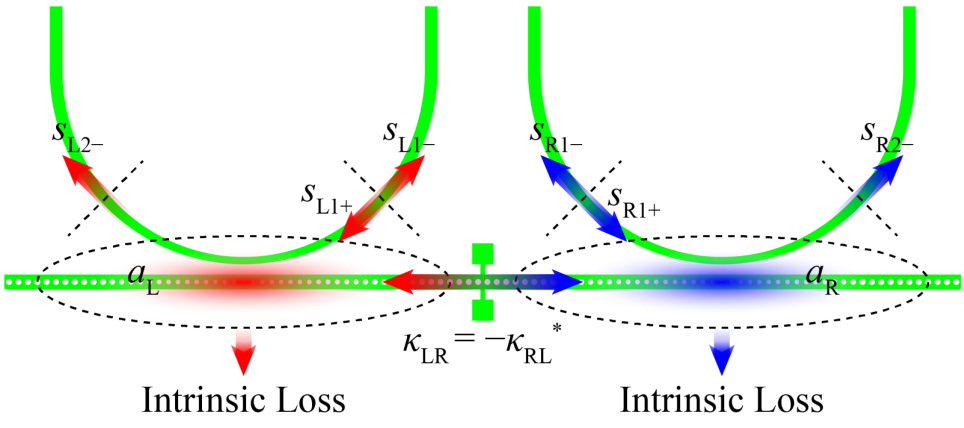

Fig. 5.11. Temporal coupled mode theory model for our device.

denoted with "a". The field amplitudes are normalized such that $|s|^2$ equals the optical power of the waveguide mode, while $|a|^2$ equals the intra-cavity optical energy. The subscripts "L" and "R" indicate the left and right sides of the device, respectively. The subscripts "1" and "2" indicate the input and output ports of the waveguides, respectively. The subscripts "+" and "–" indicate the incoming and outgoing waveguide modes, respectively. The coupling between the two cavities is described by the inter-cavity coupling rates κ_{LR} and κ_{RL}. With above defined variables and parameters, the photon dynamics of the system can be described by the following sets of coupled mode Eq. (5.2) to Eq. (5.4).

$$\begin{aligned} \frac{da_L}{dt} &= \left(j\omega_L - \frac{1}{\tau_L} \right) a_L + \frac{1}{\sqrt{\tau_{Le}}} s_{L1+} + \kappa_{LR} a_R \\ \frac{da_R}{dt} &= \left(j\omega_R - \frac{1}{\tau_R} \right) a_R + \frac{1}{\sqrt{\tau_{Re}}} s_{R1+} + \kappa_{RL} a_L \end{aligned} \tag{5.2}$$

$$s_{L2-} = -s_{L1+} + \frac{1}{\sqrt{\tau_{Le}}} a_L, \; s_{R2-} = -s_{R1+} + \frac{1}{\sqrt{\tau_{Re}}} a_R \tag{5.3}$$

$$\kappa_{LR} = -\kappa_{RL}^{*} \tag{5.4}$$

The resonance angular frequency and the total intra-cavity field amplitude decay rate of the left (right) cavity are denoted by ω_L (ω_R) and $1/\tau_L$ ($1/\tau_R$), respectively, where $\tau_L/2$ ($\tau_R/2$) is the total cavity photon lifetime. The external intra-cavity field amplitude decay rate due to waveguide coupling is denoted by $1/\tau_{Le}$ ($1/\tau_{Re}$), where the subscript "e" stands

for "external". Therefore, the intrinsic intra-cavity field amplitude decay rate of the left (right) cavity is $1/\tau_{\mathrm{Li}} = 1/\tau_{\mathrm{L}} - 1/\tau_{\mathrm{Le}}$ ($1/\tau_{\mathrm{Ri}} = 1/\tau_{\mathrm{R}} - 1/\tau_{\mathrm{Re}}$), where the subscript "i" stands for "intrinsic".

Since the mechanical resonance frequency of the photon see-saw device (441 kHz) is approximately five orders of magnitude smaller than the linewidth ($2/2\pi\tau_{\mathrm{L,R}}$ ~19 GHz) of either cavity, the device operates in the side-band unresolved regime. Therefore, when analyzing the optomechanical dynamics, static solutions of the coupled mode equations can be used at any moment during the mechanical motion. The eight parameters describing the two cavities and their coupling, i.e., ω_{L}, ω_{R}, τ_{L}, τ_{R}, τ_{Le}, τ_{Re}, κ_{LR} and κ_{RL}, can be treated as static parameters that only depend on the mechanical position of the device which is slowly varying compared with the photon dynamics.

Consider that a monochromatic continuous-wave laser at angular frequency ω with constant power P_{in} is sent into the input waveguide of the left cavity ($s_{\mathrm{L1+}} = P_{\mathrm{in}}^{0.5} e^{j\omega t}$) and no laser is sent into the input waveguide of the right cavity ($s_{\mathrm{R1+}} = 0$). In steady state, intra-cavity field a_{L} and a_{R} can be obtained by solving Eq. (5.2) as the following:

$$a_{\mathrm{L}} = \frac{\left[j\left(\omega - \omega_{\mathrm{R}}\right) + \frac{1}{\tau_{\mathrm{R}}} \right] \frac{1}{\sqrt{\tau_{\mathrm{Le}}}} s_{\mathrm{L1+}}}{\left[j\left(\omega - \omega_{\mathrm{L}}\right) + \frac{1}{\tau_{\mathrm{L}}} \right] \left[j\left(\omega - \omega_{\mathrm{R}}\right) + \frac{1}{\tau_{\mathrm{R}}} \right] - \kappa_{\mathrm{RL}} \kappa_{\mathrm{LR}}}, \tag{5.5}$$

$$a_{\mathrm{R}}=\frac{\kappa_{\mathrm{RL}}\dfrac{1}{\sqrt{\tau_{\mathrm{Le}}}}s_{\mathrm{L1+}}}{\left[j\left(\omega-\omega_{\mathrm{L}}\right)+\dfrac{1}{\tau_{\mathrm{L}}}\right]\left[j\left(\omega-\omega_{\mathrm{R}}\right)+\dfrac{1}{\tau_{\mathrm{R}}}\right]-\kappa_{\mathrm{RL}}\kappa_{\mathrm{LR}}}. \tag{5.6}$$

Output waveguide mode amplitude $s_{\mathrm{L2-}}$ and $s_{\mathrm{R2-}}$ can also be solved for from Eq. (5.3). Note that the inter-cavity coupling is very weak in our device, such that

$$\left|\kappa_{\mathrm{RL}}\right|^2=\left|\kappa_{\mathrm{LR}}\right|^2<<\frac{1}{\tau_{\mathrm{L}}\tau_{\mathrm{R}}}. \tag{5.7}$$

At this weak coupling limit, Eq. (5.5) and Eq. (5.6) can be approximated as the following.

$$a_{\mathrm{L}}=\frac{\dfrac{1}{\sqrt{\tau_{\mathrm{Le}}}}s_{\mathrm{L1+}}}{j\left(\omega-\omega_{\mathrm{L}}\right)+\dfrac{1}{\tau_{\mathrm{L}}}} \tag{5.8}$$

$$a_{\mathrm{R}}=\frac{\kappa_{\mathrm{RL}}\dfrac{1}{\sqrt{\tau_{\mathrm{Le}}}}s_{\mathrm{L1+}}}{\left[j\left(\omega-\omega_{\mathrm{L}}\right)+\dfrac{1}{\tau_{\mathrm{L}}}\right]\left[j\left(\omega-\omega_{\mathrm{R}}\right)+\dfrac{1}{\tau_{\mathrm{R}}}\right]}=\frac{\kappa_{\mathrm{RL}}a_{\mathrm{L}}}{j\left(\omega-\omega_{\mathrm{R}}\right)+\dfrac{1}{\tau_{\mathrm{R}}}} \tag{5.9}$$

The intra-cavity energy of both the left and right cavities are

$$\left|a_{\mathrm{L}}\right|^2=\frac{\tau_{\mathrm{L}}^2}{\delta_{\mathrm{L}}^2+1}\left(\frac{P_{\mathrm{in}}}{\tau_{\mathrm{Le}}}\right) \tag{5.10}$$

$$\left|a_{\mathrm{R}}\right|^2=\frac{\tau_{\mathrm{R}}^2}{\delta_{\mathrm{R}}^2+1}\left(\kappa^2\left|a_{\mathrm{L}}\right|^2\right)=\frac{\left(\kappa\tau_{\mathrm{R}}\tau_{\mathrm{L}}\right)^2}{\left(\delta_{\mathrm{R}}^2+1\right)\left(\delta_{\mathrm{L}}^2+1\right)}\left(\frac{P_{\mathrm{in}}}{\tau_{\mathrm{Le}}}\right), \tag{5.11}$$

respectively, where the laser detuning (Δ_{L} and Δ_{R}), normalized laser detuning (δ_{L} and δ_{R}) and inter-cavity coupling rate (modulus) κ are defined in the following.

$$\delta_{\mathrm{L}} = \tau_{\mathrm{L}}\Delta_{\mathrm{L}} = \tau_{\mathrm{L}}\left(\omega - \omega_{\mathrm{L}}\right),\ \delta_{\mathrm{R}} = \tau_{\mathrm{R}}\Delta_{\mathrm{R}} = \tau_{\mathrm{R}}\left(\omega - \omega_{\mathrm{R}}\right) \tag{5.12}$$

$$\kappa = \left|\kappa_{\mathrm{LR}}\right| = \left|\kappa_{\mathrm{RL}}\right| \tag{5.13}$$

The power transmission from the input of the left waveguide to the output of the left and right waveguides, respectively, are:

$$T_{\mathrm{LL}} = \frac{\left|s_{\mathrm{L2-}}\right|^2}{\left|s_{\mathrm{L1+}}\right|^2} = 1 - \frac{1 - T_{\mathrm{LL0}}}{\delta_{\mathrm{L}}^2 + 1} \tag{5.14}$$

$$T_{\mathrm{RL}} = \frac{\left|s_{\mathrm{R2-}}\right|^2}{\left|s_{\mathrm{L1+}}\right|^2} = \frac{T_{\mathrm{RL0}}}{\left(\delta_{\mathrm{R}}^2 + 1\right)\left(\delta_{\mathrm{L}}^2 + 1\right)}, \tag{5.15}$$

where T_{LL0} and T_{RL0} are defined in the following.

$$T_{\mathrm{LL0}} = \left(\tau_{\mathrm{Le}} - \tau_{\mathrm{L}}\right)^2 \Big/ \tau_{\mathrm{Le}}^2 \tag{5.16}$$

$$T_{\mathrm{RL0}} = \left|\kappa_{\mathrm{RL}}\right|^2 \left(\tau_{\mathrm{L}}\tau_{\mathrm{R}}\right)^2 \Big/ \left(\tau_{\mathrm{Le}}\tau_{\mathrm{Re}}\right) \tag{5.17}$$

Using Eq. (5.10), Eq. (5.11), Eq. (5.14) and Eq. (5.15), the intra-cavity energy of both the left and right cavities can be expressed in terms of T_{LL} and T_{RL}, which are directly measurable during the experiment:

$$\left|a_{\mathrm{L}}\right|^2 = \frac{\tau_{\mathrm{Le}}\tau_{\mathrm{L}}}{2\tau_{\mathrm{Le}} - \tau_{\mathrm{L}}}\left(1 - T_{\mathrm{LL}}\right)P_{\mathrm{in}} \tag{5.18}$$

$$\left|a_{\mathrm{R}}\right|^2 = \tau_{\mathrm{Re}}T_{\mathrm{RL}}P_{\mathrm{in}} \tag{5.19}$$

Also, from the energy conservation consideration, the time-averaged net optical power flow from the left cavity to the right cavity, which is the only source of power input to the

right cavity, should equal the time-averaged loss of optical power from the right cavity. This net transferred power, denoted by P_{tr}, can be readily expressed as:

$$P_{\mathrm{tr}} = \frac{2}{\tau_{\mathrm{R}}}\left|a_{\mathrm{R}}\right|^2 = \frac{2\tau_{\mathrm{Re}}}{\tau_{\mathrm{R}}} T_{\mathrm{RL}} P_{\mathrm{in}} . \tag{5.20}$$

It is worth noting that, when weak coupling condition Eq. (5.7) holds, the expressions Eq. (5.8) and Eq. (5.14), for a_{L} and T_{LL}, respectively, are the same as those in the case where the two cavities are completely isolated. This means that if the device is excited and measured only from the same side (including both the cavity and waveguide) of the see-saw and no optomechanical effects are induced, the weakly coupled cavity on the other side has no effect on the photon dynamics. This explains the reason why each of the measured transmission spectra shown in Fig. 5.3a and Fig. 5.3b exhibits only one resonance dip, in which the coupling between the two cavities is not evident. This also explains the simple and similar mathematical forms of Eq. (5.10) and Eq. (5.11) – the only input to the right cavity is the coupling field from the left cavity.

5.7. Cavity Optomechanical Coupling

Due the cavity optomechanical coupling induced by the evanescent field of the cavity mode that penetrates into the substrate, the cavity parameters are dependent on the gap size between the cavity and the substrate, hence are dependent on the rotation angle of the see-saw device. Assuming that among all the eight cavity parameters, i.e., ω_{L}, ω_{R}, τ_{L}, τ_{R},

τ_{Le}, τ_{Re}, κ_{LR} and κ_{RL}, only the resonance frequencies of the two cavities ω_L and ω_R are dependent on the rotation angle θ of the see-saw device. The intrinsic cavity field decay rates are dominated by the scattering loss, therefore they are not sensitive to the rotation. The coupling loss is also insensitive to the rotation to the first order because of the mirror symmetry of the rotational motion with respect to the coupling waveguides. And the inter-cavity coupling rates (κ_{LR} and κ_{RL}) apparently are independent of the rotation because the separation between the cavities is not affected.

When $|\theta| << 1$, the optomechanical coupling of the cavities can be linearized and given by equations and inequalities Eq. (5.21) to Eq. (5.23) [34], [78]. The small θ assumption is valid because in the experiments presented in this work, θ is always on the order of 10^{-3} rad or smaller.

$$\begin{aligned} \omega_L(\theta) &= \omega_{L0} + \frac{g_{L0}}{2\alpha_L}\left[1-\exp\left(-2\alpha_L\theta\right)\right] \simeq \omega_{L0} + g_{L0}\theta \\ \omega_R(\theta) &= \omega_{R0} + \frac{g_{R0}}{2\alpha_R}\left[1-\exp\left(-2\alpha_R\theta\right)\right] \simeq \omega_{R0} + g_{R0}\theta \end{aligned} \tag{5.21}$$

where $\omega_{L0} = \omega_L(\theta{=}0)$, $\omega_{R0} = \omega_R(\theta{=}0)$, and

$$g_{L0} = \left.\frac{d\omega_L}{d\theta}\right|_{\theta=0} < 0,\ g_{R0} = \left.\frac{d\omega_R}{d\theta}\right|_{\theta=0} > 0 \tag{5.22}$$

$$\alpha_L < 0,\ \alpha_R > 0 \tag{5.23}$$

The parameters g_{L0} (g_{R0}) and α_L (α_R) are the optomechanical coupling coefficient at zero rotation angle and the out-of-plane field decay constant of the left (right) cavity mode.

The sign of θ is consistently defined in this work such that $\theta > 0$ when the right (left) cavity is rotated away from (closer to) the substrate; and $\theta < 0$ when the right (left) cavity is rotated closer to (away from) the substrate. The Eq. (5.21) and Eq. (5.22) describe the anti-symmetric optomechanical coupling of the two cavities to the rotational motion of the photon see-saw.

5.8. Photonic Crystal Nanobeam Cavity Design

The two cavities are designed to be identical using a deterministic method [114]. In order to achieve the optimal trade-off between high quality factor and strong optomechanical coupling, the fundamental air mode is used, with effective mode index (1.71) close to the refractive index of the substrate (1.44), so that the evanescent tail of the cavity mode extends well into the substrate.

As shown in Fig. 5.1c, each cavity is constituted by a 700 nm wide, 220 nm thick and 22.95 μm long silicon nanobeam on one side of the see-saw device. A total of 51 holes are used in each cavity and the distance between the centers of adjacent holes is fixed at 450 nm. The diameter of the holes varies from 297 nm, at the edges of the cavity, to 228 nm, at the center of the cavity.

5.9. Mechanical Modes of the Photonic Crystal Nanobeam

With the Finite Element Method (FEM) and the exact geometry of our device, we calculated the six lowest frequency mechanical modes of our device. In Table 5.1, the

Table 5.1. Summary of the mechanical modes.

Abbreviations: Symm, symmetric; Anti-symm, anti-symmetric.

Mechanical Mode	OA1 Torsional	OS1 Flapping	IA1	IS1	OA2	OS2
Direction of Displacement	Out-of-plane	Out-of-plane	In-plane	In-plane	Out-of-plane	Out-of-plane
Symmetry	Anti-symm	Symm	Anti-symm	Symm	Anti-symm	Symm
Number of anti-node(s) on either side	1	1	1	1	2	2
Resonance frequency from FEM simulation	460 kHz	530 kHz	1.67 MHz	2.00 MHz	3.02 MHz	3.36 MHz
Resonance frequency from experiments	441 kHz	514 kHz	Not detected	Not detected	2.92 MHz	3.26 MHz
Quality factor from experiments	1.66×10^4	1.68×10^4	Not detected	Not detected	1.32×10^4	1.33×10^4

calculation results and the experimental results (from thermomechanical noise measurement and the impulse response measurement in vacuum) are summarized, which agree well, except that the in-plane modes could not be transduced due to the negligibly small lateral optomechanical coupling between the cavities and the waveguides.

5.10. Special Precautions for the Wet Etch Releasing Process

To release the nanobeam, we used diluted hydrofluoric (HF) acid instead of the buffered oxide etch (BOE) because BOE seems to roughen the surface of the silicon structure and

is detrimental to the quality factor of the photonic crystal cavity. The diluted HF used consists of 4 volume parts of DI water and 1 volume part of 49% concentrated HF.

The waveguide width is tapered from 600 nm to 345 nm as it gradually approaches the cavity, to achieve better phase matching with the cavity mode and hence more efficient coupling, as shown in Fig. 5.1c. Meanwhile, after the HF wet etching process, we confirmed with surface profilometer that the depth etched into the buried oxide (BOX) layer was ~ 250 nm. Therefore, only a short section of the tapered waveguide that is narrower than ~ 500 nm was released. The released waveguides are adequately mechanically robust, hence did not stiction to the substrate, as is evident in Fig. 5.12.

After wet etching, we used critical point dryer (CPD) to avoid the stiction problem during the evaporation of the solvent.

5.11. Scanning Electron Microscope (SEM) Observations of the Suspended Structures

SEM observations of the suspended photonic crystal nanobeams turned out to be challenging and destructive, because the nanobeams are highly compliant with a small gap of only ~ 250 nm above the substrate. Such mechanical structures are very susceptible to be irreversibly pulled down by electrostatic force due to the accumulated charge on the insulating SiO_2 substrate during SEM imaging. Once pulled down, the released structures will be stictioned to the substrate and cannot be recovered.

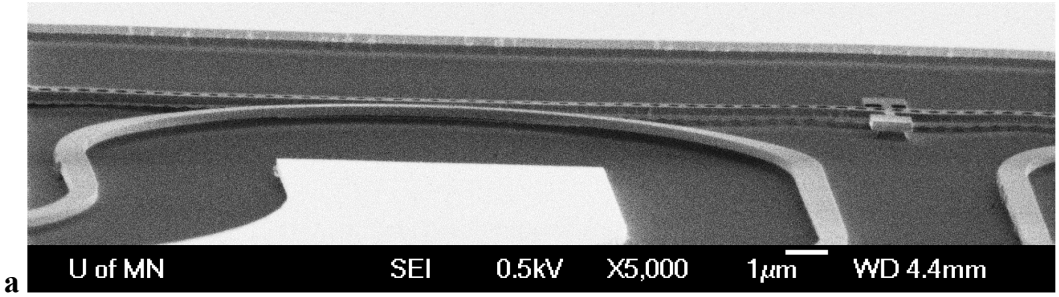

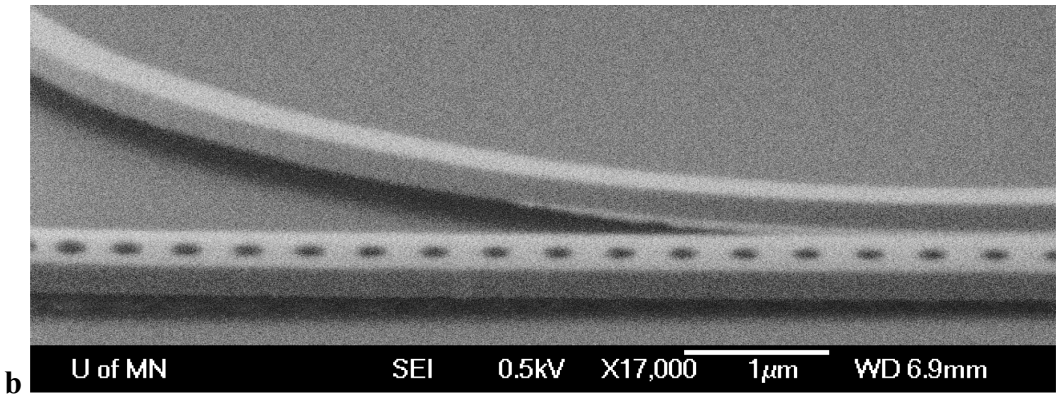

Fig. 5.12. SEM images of the suspended structures.

a. Tilted view of one side of the suspended nanobeam. **b**. Close-up tilted view of the photonic crystal cavity and the suspended part of the waveguide.

In order to avoid significant charging effect, we grounded the top silicon layer of our sample well and used the lowest kV and probe current available, which resulted in non-optimal image resolution. Nevertheless, none of the ~ 20 nanobeam devices that were imaged survived. We did not image the one device that we measured and presented here.

The two images in Fig. 5.12, obtained with a JEOL 6500F SEM, clearly show one side of the suspended structures, although the other side has been pulled down during the SEM imaging. If not imaged in SEM, the entire nanobeam should be straight and both sides

should be even, because the nanobeam is symmetric, free at both ends and has an array of holes inscribed, therefore the built-in stress can be completely relaxed. The waveguides are observed to be partly released, suspended and in the same plane as the suspended nanobeam. Also, the oxide ridges under the suspended structures and the partial undercut at the edges of unsuspended structures can be seen. The etching depth of 250 nm into the BOX layer is shown clearly by comparison to the 220nm thickness of the silicon layer.

In addition to SEM images, optical microscope observations can as well determine whether the structures are suspended, stictioned down or bent up after the wet etch releasing processes. The technique is that the color of the suspended structures depends on the gaps under them due to the interference of the illumination light, preferably white light, which produces rich colors from the interference. This method has been proved sensitive enough and quite reliable according to our experience, and serves as a non-destructive alternative to SEM.

5.12. Transmission Spectrum Measurement and Determination of Cavity Parameters

The transmission spectra of both sides of the see-saw device were measured with laser power below the threshold of optomechanical self-oscillation. In order to accurately determine the resonance wavelengths of both cavities and their difference, the measurement results were calibrated using a wavelength reference gas cell (Wavelength References Inc.). Within the narrow linewidth of the cavity resonance, the grating coupler transmission can be approximated as constant. After taking into account the insertion loss

in the measurement system, the transmission spectra shown in Fig. 5.3b are measured results of T_{LL} and T_{RR}, given by Eq. (5.14). The cavity resonance angular frequencies when $\theta = 0$ (ω_{L0} and ω_{R0}) can be readily determined from the measured transmission spectra, while other four cavity parameters, τ_L, τ_R, τ_{Le}, τ_{Re}, can be calculated from the resonance linewidth (γ_L and γ_R) and extinction ratio (E_L and E_R) with the Eq. (5.24) and Eq. (5.25) . The cavity parameters determined from the transmission spectrum measurement are summarized in Table 5.2.

$$\tau_L^{-1} = \gamma_L/2\,,\ \tau_R^{-1} = \gamma_R/2 \tag{5.24}$$

$$\tau_{Le}^{-1} = \left(1 - E_L^{-0.5}\right)\left(\gamma_L/2\right),\ \tau_{Re}^{-1} = \left(1 - E_R^{-0.5}\right)\left(\gamma_R/2\right) \tag{5.25}$$

Table 5.2. Summary of the cavity parameters.

Cavity Position	**Left Cavity**	**Right Cavity**
Pump Or Probe	Pump	Probe
Resonance Wavelength	1541.219 nm	1541.574 nm
Resonance Frequency Difference ($\omega_{R0} - \omega_{L0}$)	$(2\pi)\cdot$44.8 GHz	
Linewidth in Terms of Frequency (γ_L and γ_R)	$(2\pi)\cdot$18.93 GHz	
Loaded Quality Factor	1.03×10^4	
Extinction Ratio (E_L and E_R)	2.50	2.68
Intrinsic Quality Factor	1.62×10^4	1.68×10^4
Intrinsic Lifetime (τ_{Li} and τ_{Ri})	26.59 ps	27.53 ps
External Lifetime (τ_{Le} and τ_{Re})	45.75 ps	43.21 ps
Total Lifetime (τ_L and τ_R)	16.82 ps	

5.13. Main Experimental Setup

The main experimental setup used in this work is shown in Fig. 5.13. In the probe channel, the power and polarization state of the input laser are controlled by a VOA and an FPC, respectively. The output laser power is then controlled by a VOA and subsequently detected with a PD and either an OS or an SA. For low output signal, an EDFA is used to amplify it and an OTF is used after to suppress the amplified spontaneous emission (ASE) of the EDFA.

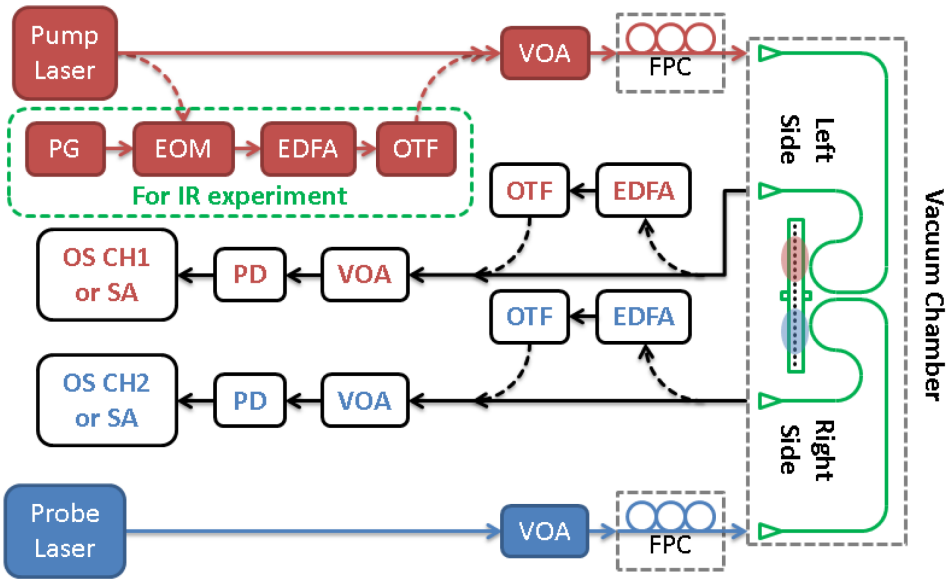

Fig. 5.13. Main experimental setup.

Abbreviations: CW, continuous-wave; IR, impulse response; VOA, variable optical attenuator; FPC, fiber polarization controller; EDFA, erbium doped fiber amplifier; OTF, optical tunable filter; PD, photo diode; OS, oscilloscope; CH1, Channel 1; CH2, Channel 2; SA, spectrum analyzer; EOM, electro-optic modulator; PG, pulse generator.

The pump channel is identical to the probe channel except for the impulse response experiment: In this case, the pump laser power is first modulated by an electrical pulse generator via an EOM, then the pulses are amplified by an EDFA and an OTF is used to suppress ASE.

5.14. Thermomechanical Noise and Cavity Optomechanical Dynamical Backaction Experiments

We employed the slope detection scheme [34] to measure the thermomechanical noise of the see-saw device. When the probe laser power was very low (2.28 nW), the intrinsic resonance frequencies and quality factors of the torsional and flapping modes were

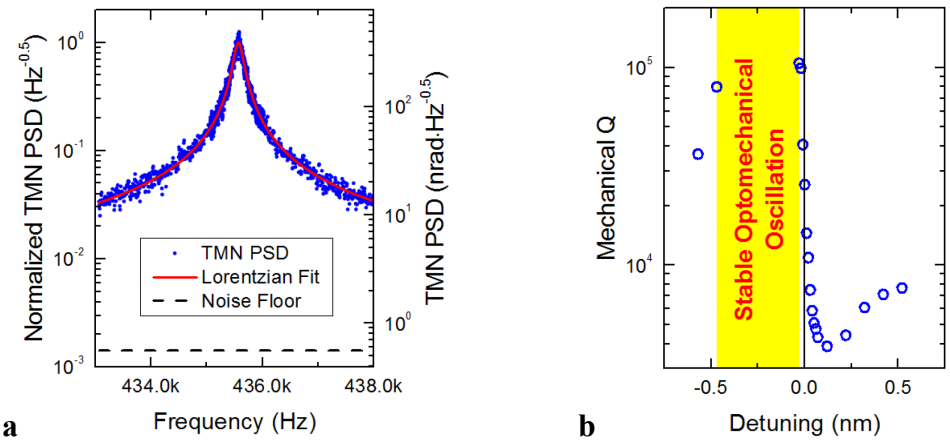

Fig. 5.14. Standard cavity optomechanical experiments.

a. Thermomechanical noise measurement data showing the best sensitivity of torque moment achieved so far on the see-saw devices. **b**. Typical dynamical backaction measurement data of the see-saw devices. Abbreviations: TMN, thermomechanical noise; PSD, power spectral density.

measured to be f_1 = 441 kHz (Q_1 = 1.66×10^4) and f_2 = 514 kHz (Q_2 = 1.68×10^4), respectively. Subsequently, in order to demonstrate high measurement sensitivity of the torque moment, we used a much stronger probe laser (35.5 μW), red detuned to avoid exciting optomechanical self-oscillation. To avoid the risk of permanent damage to this device caused by overheating, we conducted the measurement on another device with the same design but slightly different parameters. The best sensitivity of the torque moment achieved so far is 9.69 fN·μm·Hz$^{-0.5}$, as is shown in Fig. 5.14a. We expect better detection sensitivity when we have optimized our devices in the future specifically for sensing applications.

To measure the cavity optomechanical dynamical backaction, we sent a CW pump laser with constant power (6.35 μW) but varied detuning into one cavity and measure the altered thermomechanical noise with a weak probe laser (2.28 nW) sent into the other cavity. Typical measurement data are shown in Fig. 5.14b, where stable optomechanical self-oscillation was excited when the pump laser was blue detuned and a maximum cooling factor of 4 was achieved when the pump laser was red detuned.

5.15. Impulse Response Experiment (More Details)

In the impulse response experiment, the width of the rectangle optical pulses sent into the input waveguide of the pump (left) cavity was 500 ns, with a rising edge of about 5 ns. The repetition rate of the pulses was 1 kHz for measurement in atmosphere and 1.76 Hz for

measurement in vacuum. In both cases, the repetition rate was low enough for the device's mechanical impulse response to decay sufficiently between the pump pulses.

The actual pulse width in term of the number of intra-cavity photons, however, was much smaller than the input pulse width and only on the order of 10 ns due to thermo-optical shift of the resonance. This is evident in Fig. 5.15 where the waveforms of the input and output pump pulses are shown. The pump laser was initially red detuned to the cold pump cavity. When the input pulse arrived at the cavity at $t = 0$, it started to heat the cavity due to two photon absorption and free carrier absorption in silicon. At approximately $t =$ 50 ns, the cavity resonance aligned with the pump laser wavelength and the output pump pulse reached a local minimum shown as a dip in the time-domain trace. After that, the pump laser was more and more blue-detuned to the cavity resonance. At $t = 500$ ns, the

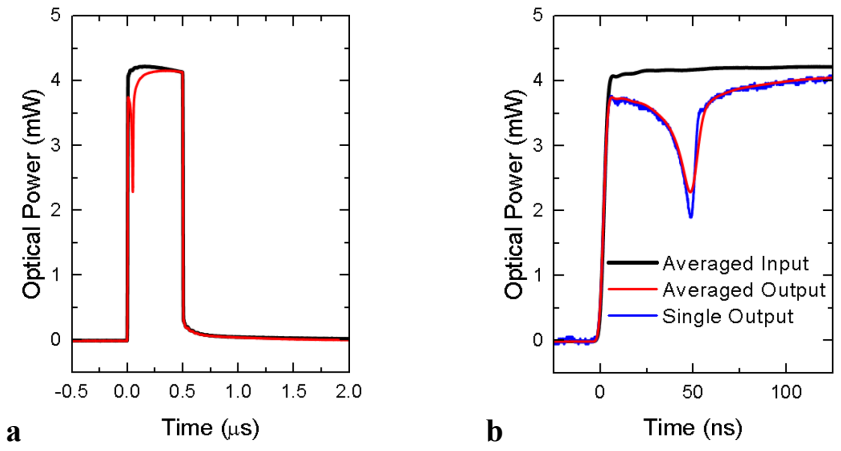

Fig. 5.15. Waveforms of the pump pulse.

a. Averaged ($N = 1\times10^3$) input and output pump pulses. **b**. Close-up view of **a**, with an additional output pump pulse from a single measurement.

pulse ended, and the pump laser reached maximum blue-detuning. The dip in the output pump pulses resembles the Lorentzian line shape of the pump cavity resonance because during the pulse, the pump laser wavelength was fixed and the resonance wavelength of the cavity was continuously red-shifting. Although possible, it is not trivial to quantitatively model this process, nor is it relevant to our primary goal of this experiment. From the waveform of a single measurement shown in Supplementary Fig. 5.15b, the width of the quasi-Lorentzian dip inside the rectangle pulse is approximately 10 ns, which corresponds to the pulse width of photon flux entering the cavity.

During the impulse response measurement in vacuum, the input probe laser power used should be as small as possible in order to prevent the optomechanical backaction effects from significantly altering the mechanical ring-down time. On the other hand, sufficient probe laser power is necessary to maintain enough measurement signal to noise ratio. As a tradeoff, the input probe laser used was 28.7 nW, and the results shown in Fig. 5.4a (Fig. 5.5a) are the average of 1×10^4 (1.5×10^4) measurements in vacuum (atmosphere). It is worth noting that in vacuum, the amplitude of the mechanical response is large enough such that the slope detection scheme [34] employed here is no longer perfectly linear. This is evident from that the two ring-down waveforms in Fig. 5.4a are both slightly asymmetric in positive and negative amplitudes. This minor non-ideality does not change our conclusions in any significant way.

The mechanical resonance frequencies of the torsional mode (441 kHz) and flapping mode (514 kHz) measured from the device ring-down in vacuum agree very well

with those measured from the device's thermomechanical noise and with the finite element method (FEM) simulation results (460 kHz for the torsional mode and 530 kHz for the flapping mode).

In the impulse response measured in atmosphere shown in Fig. 5.5a, the time scale and waveform of the contribution from the temperature rise and thermo-optic effect of the cavities agree very well with our FEM simulation results shown in Fig. 5.16. The simulation takes into account the distributed heating source that corresponds to the optical cavity mode profile of the left cavity, heat flow through the nanobeam toward the right cavity and dissipation into the SiO_2 substrate. The spatial temperature distribution of the right cavity during this process is not uniform, so the result shown in Fig. 5.16 is the weighted average temperature rise of the right cavity, where the weights correspond to the

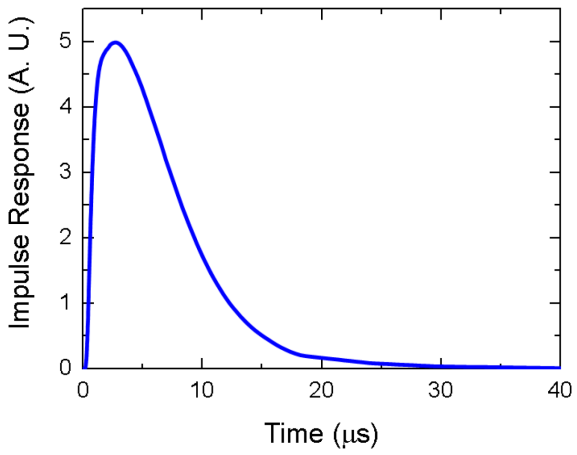

Fig. 5.16. FEM simulation results for the impulse response contributed by the temperature rise and thermo-optic effect of silicon.

optical cavity mode profile. The simulation result shows a fast temperature rise with rise time (from 10% to 90%) of 0.91 μs and a slower cooling with fall time (from 90% to 10%) of 10.55 μs, in good agreement with the measured impulse response.

5.16. Dynamics of the Cavity Resonance Frequencies During Oscillation (More Details)

In dynamics measurement shown in Fig. 5.6, Fig. 5.7 and Fig. 5.8, optomechanical self-oscillation was excited and detected with the CW pump and probe lasers, respectively, both at constant input power level. The oscillatory rotation of the see-saw periodically modulated the resonance frequencies of both cavities, leading to periodically modulated output power of both the pump and probe lasers. From the measured output signal in time-domain, the instantaneous rotation angle and the resonance frequencies at every moment of the oscillation can be derived with the procedure shown below.

When the optomechanical self-oscillation takes place, the rotation angle oscillates sinusoidally as follows:

$$\theta(t) = \theta_{\max} \cos\left(\Omega_{\mathrm{m}} t + \varphi_{\mathrm{m}}\right), \tag{5.26}$$

where $\theta_{\max}$ is the oscillation amplitude, Ω_{m} is the mechanical oscillation frequency of the torsional mode and φ_{m} is the phase of the oscillation when $t = 0$, which we set to be zero ($\varphi_{\mathrm{m}} = 0$) for all the periodic time-domain traces presented in this work. According to Eq. (5.21) to Eq. (5.23), the resonance frequencies of both cavities swing back and forth

simultaneously during the oscillation and can be rewritten as functions of time using Eq. (5.26):

$$\begin{aligned}\omega_{\mathrm{L}}(t) &= \omega_{\mathrm{L}0} + \frac{g_{\mathrm{L}0}}{2\alpha_{\mathrm{L}}}\left[1-\exp\left(-2\alpha_{\mathrm{L}}\theta_{\max}\cos\left(\Omega_{\mathrm{m}}t\right)\right)\right] \\ \omega_{\mathrm{R}}(t) &= \omega_{\mathrm{R}0} + \frac{g_{\mathrm{R}0}}{2\alpha_{\mathrm{R}}}\left[1-\exp\left(-2\alpha_{\mathrm{R}}\theta_{\max}\cos\left(\Omega_{\mathrm{m}}t\right)\right)\right]\end{aligned} \tag{5.27}$$

First consider the case where only the pump laser is on, and the probe laser is off. Because the mechanical resonance frequency is five orders of magnitude smaller than the linewidth of either cavity (i.e. sideband unresolved), the retardation of the intra-cavity field response with respect to the mechanical motion is negligible even when the optomechanical self-oscillation occurs. Therefore, the transmission of the pump laser $T_{\mathrm{LL}}^{\mathrm{p}}$ can still be expressed by Eq. (5.14) after incorporating Eq. (5.27):

$$T_{\mathrm{LL}}^{\mathrm{p}}(t) = 1 - \frac{1-\tau_{\mathrm{Le}}{}^{-2}\left(\tau_{\mathrm{Le}}-\tau_{\mathrm{L}}\right)^2}{\tau_{\mathrm{L}}{}^2\left\{\Delta_{\mathrm{p}} - \frac{g_{\mathrm{L}0}}{2\alpha_{\mathrm{L}}}\left[1-\exp\left(-2\alpha_{\mathrm{L}}\theta_{\max}\cos\left(\Omega_{\mathrm{m}}t\right)\right)\right]\right\}^2 + 1}, \tag{5.28}$$

where $\Delta_{\mathrm{p}} = \omega_{\mathrm{p}} - \omega_{\mathrm{L}0}$ is the pump laser detuning relative to the resonance of the left cavity when $\theta = 0$.

To prove the self-oscillation dynamics, the probe laser is turned on with a power level much lower than that of the pump laser such that its effect on the oscillation amplitude and frequency is negligible. Similarly, the transmission of the probe laser is given by Eq. (5.14) and Eq. (5.27):

$$T_{\mathrm{RR}}^{\mathrm{b}}(t)=1-\frac{1-\tau_{\mathrm{Re}}{}^{-2}\left(\tau_{\mathrm{Re}}-\tau_{\mathrm{R}}\right)^{2}}{\tau_{\mathrm{R}}{}^{2}\left\{\Delta_{\mathrm{b}}-\frac{g_{\mathrm{R0}}}{2\alpha_{\mathrm{R}}}\left[1-\exp\left(-2\alpha_{\mathrm{R}}\theta_{\max}\cos\left(\Omega_{\mathrm{m}}t\right)\right)\right]\right\}^{2}+1}, \tag{5.29}$$

where $\Delta_{\mathrm{b}}=\omega_{\mathrm{b}}-\omega_{\mathrm{R0}}$ is the probe laser detuning relative to the resonance of the right cavity when $\theta=0$.

The Eq. (5.28) and Eq. (5.29) are written only using measurable physical parameters of the system. The time-varying transmission $T_{\mathrm{LL}}^{\mathrm{p}}(t)$ and $T_{\mathrm{RR}}^{\mathrm{b}}(t)$ were measured during the experiment. Their representative time-domain traces are shown in Fig. 5.17a and Fig. 5.6, respectively. The cavity parameters (ω_{L}, ω_{R}, τ_{L}, τ_{R}, τ_{Le} and τ_{Re}), the

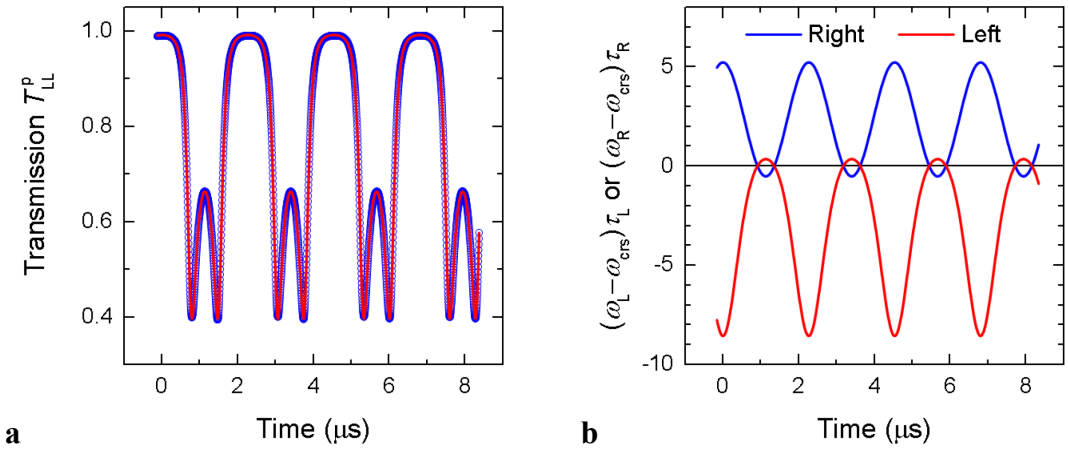

Fig. 5.17. Supplementary time-domain traces pertaining to the dynamics of the cavity resonance frequencies during oscillation.

a. Measured time-domain trace of $T_{\mathrm{LL}}^{\mathrm{p}}(t)$ overlaid with curve fitting result using equation (5.28). **b**. Time-domain traces of $\omega_{\mathrm{L}}(t)$ and $\omega_{\mathrm{R}}(t)$ calculated from experiment data, referenced to the resonance cross-over point ω_{crs} and normalized by half the cavity linewidth.

mechanical resonance frequency (Ω_m) and the optomechanical coupling coefficients (g_{L0} and g_{R0}) can all be independently determined from the transmission spectra shown in Fig. 5.3b and the thermomechanical noise calibration [34]. The only unknown parameters in Eq. (5.28) and Eq. (5.29) are α_L , α_R and θ_{max} , which can be obtained by curve fitting the time-domain traces $T_{LL}^{p}(t)$ and $T_{RR}^{b}(t)$. As shown in Fig. 5.17a and Fig. 5.6, results from the above theoretical model are in excellent agreement with the experimental measurement. In Table 5.3, both the optomechanical parameters determined experimentally here and the simulation results are summarized and compared, which agree reasonably well.

With the above theoretical model and determined parameters, the characteristics of the system at any moment during the oscillation can be derived. For example the instantaneous resonance frequencies of both cavities ($\omega_L(t)$ and $\omega_R(t)$) can be determined from Eq. (5.27). The result is plotted in Fig. 5.17b, showing that, with sufficient oscillation amplitude, the two resonances can cross over each other during one oscillation cycle.

Table 5.3. Summary of the optomechanical parameters.

Cavity Position		**Left Cavity**	**Right Cavity**
Pump Or Probe		Pump	Probe
Optomechanical Coupling Coefficient (g_{L0} and g_{R0})	**Experiment***	−42.0 THz·rad^{-1}	30.4 THz·rad^{-1}
	FDTD**	±24.49 THz·rad^{-1}	
Field Decay Constant (α_L and α_R)	**Experiment**	−439 rad^{-1}	109 rad^{-1}
	FDTD	±75.3 rad^{-1}	

* These results assume zero deflection angle, i.e., $\theta = 0$.

** These results assume the bottom of the cavity is 250 nm above the SiO_2 substrate.

Similarly, the dependence of ω_L and ω_R on θ can also be calculated. Results averaged from all the measured time-domain traces are shown in Fig. 5.8.

Another probably more intuitive method based on stroboscopic principle can be used to determine the time-varying resonance frequencies of the cavities, as is shown in Fig. 5.7. If the motion of the oscillating see-saw is "frozen" at an arbitrary instant in time, while the probe laser frequency is varied, the measured transmission of the probe laser T_{RR}^{b} given by Eq. (5.14) as a function of probe laser frequency will give a snapshot of the resonance line shape of the right cavity. The instantaneous resonance frequency of the cavity can thus be determined from such a snapshot. After many snapshots are taken over the duration of the oscillation cycle, the complete dynamics of the cavity resonance can be captured in exactly the same way of stroboscopic imaging methods.

In the actual experiment, however, instead of sweeping the probe laser frequency, time-domain data traces were taken with varied probe laser frequency. The probe laser transmission can be expressed in expanded form of Eq. (5.14) as a function of both probe laser angular frequency and time:

$$T_{RR}^{b}\left(\omega_b, t\right) = 1 - \frac{1 - T_{RR0}}{\tau_R{}^2\left[\omega_b - \omega_R\left(t\right)\right]^2 + 1} \tag{5.30}$$

Experiment data corresponding to Eq. (5.30) is plotted in Fig. 5.18 as a color coded surface versus both t and ω_b. In the stroboscopic explanation, time is fixed and the probe laser frequency is varied. This corresponds to a vertical cross-sectional cut in Fig. 5.18.

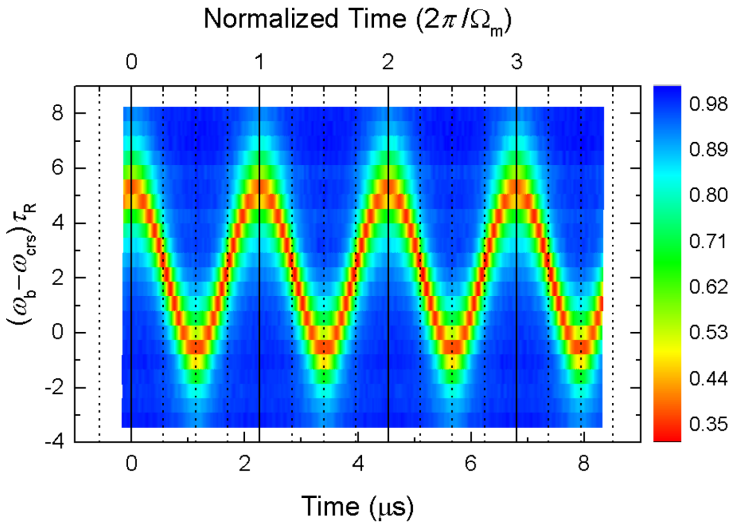

Fig. 5.18. The dynamics of cavity resonance.

The bottom horizontal axis is time in unit of μs while the top horizontal axis is normalized time in unit of the mechanical oscillation period. The vertical axis is ω_b referenced to the resonance cross-over point ω_{crs} and normalized by half the cavity linewidth.

Specifically, the vertical cross sections at $t=0$, $0.5\pi/\Omega_m$ and π/Ω_m correspond to $\theta=\theta_{max}$, 0 and $-\theta_{max}$, respectively, as shown in Fig. 5.7. In the experiment, each trace was taken with fixed probe laser frequency and thus corresponds to a horizontal cross-sectional cut in Fig. 5.18. Hence our time-domain measurement method is equivalent to the stroboscopic principle and the dynamics of cavity resonance shown in Fig. 5.18 can be constructed from the measurement results.

In the actual experiment, the input pump and probe laser power were 3.4 μW and 2.3 nW, respectively. The measured time-domain traces $T_{LL}^{p}(t)$ and $T_{RR}^{b}(t)$ shown in Fig. 5.17a and Fig. 5.6 were the average of 5×10^3 and 5×10^4 measurements, respectively.

5.17. Photon Shuttling Experiment (More Details)

In the photon shuttling experiment, Fig. 5.9 were obtained when the pump laser frequency was fixed while its power was gradually increased from 0.135 μW, which was the threshold level to excite the self-oscillation, to 6.76 μW. Fig. 5.10b was obtained when the pump laser power was fixed at 6.76 μW while its frequency was varied in the range that could excite self-oscillation. For each combination of pump laser frequency and power, we obtained and processed data following a two-step procedure. We first follow the method described in Section 5.16 to determine the dynamics of the cavity resonance frequencies and all of the parameters of the system except the inter-cavity coupling rate κ as the only unknown. In the second step, the probe laser was turned off, the pump laser was kept on and the transmission $T_{\mathrm{LL}}^{\mathrm{p}}(t)$ and $T_{\mathrm{RL}}^{\mathrm{p}}(t)$ were measured in time domain. Here we use the same notations as in Section 5.6 and Section 5.16, so that $T_{\mathrm{RL}}^{\mathrm{p}}(t)$ refers to the transmission of the pump laser from the left input waveguide to the right output waveguide, which is due to inter-cavity photon shuttling. According to Eq. (5.18) and Eq. (5.19), the intra-cavity optical energy as a function of t was calculated from the measured data with the following expressions.

$$\left|a_{\mathrm{L}}(t)\right|^2 = \frac{\tau_{\mathrm{Le}}\tau_{\mathrm{L}}}{2\tau_{\mathrm{Le}}-\tau_{\mathrm{L}}}\left[1-T_{\mathrm{LL}}^{\mathrm{p}}(t)\right]P_{\mathrm{in}} \tag{5.31}$$

$$\left|a_{\mathrm{R}}(t)\right|^2 = \tau_{\mathrm{Re}}T_{\mathrm{RL}}^{\mathrm{p}}(t)P_{\mathrm{in}} \tag{5.32}$$

The corresponding (average) intra-cavity photon number is given by: $n_{\mathrm{L,R}}(t) = \left|a_{\mathrm{L,R}}(t)\right|^2 / \hbar\omega_{\mathrm{p}}$. The net energy transferred from the left cavity to the right cavity during one mechanical oscillation cycle, U_{tr}, was further obtained by integrating the net power transferred in Eq. (5.20), which reads

$$U_{\mathrm{tr}} = \int_0^{2\pi/\Omega_{\mathrm{m}}} P_{\mathrm{tr}}(t)\,dt = \frac{2}{\tau_{\mathrm{R}}} \int_0^{2\pi/\Omega_{\mathrm{m}}} \left|a_{\mathrm{R}}(t)\right|^2 dt\,. \tag{5.33}$$

The (average) total number of shuttled photons per cycle thus is given by: $n_{\mathrm{tr}} = U_{\mathrm{tr}} / \hbar\omega_{\mathrm{p}}$.

Using Eq. (5.31) and Eq. (5.32), $n_{\mathrm{L}}(t)$, $n_{\mathrm{R}}(t)$ and n_{tr} are determined from measured $T_{\mathrm{LL}}^{\mathrm{p}}(t)$ and $T_{\mathrm{RL}}^{\mathrm{p}}(t)$ and plotted in Fig. 5.9. Subsequently, fitting the results with Eq. (5.11), which relates $\delta_{\mathrm{L}}(t)$, $\delta_{\mathrm{R}}(t)$ and $\left|a_{\mathrm{R}}(t)\right|^2$, yields the last unknown parameter, the inter-cavity coupling coefficient $\kappa \sim (2\pi)\cdot 0.72$ GHz.

When the pump laser frequency was increased, the oscillation amplitude of the see-saw device increased even though the power of the pump laser was fixed. In Fig. 5.10b, the parametric function Eq. (5.11) with varying pump laser frequency is plotted as a family of color coded trajectories, which span over the (δ_{L}, δ_{R}) plane almost uniformly. The trajectories become progressively longer when the pump laser frequency was increased, due to increased oscillation amplitude and swing of the cavity resonance frequencies. To better visualize the measured trajectories and compare them with the theory, we take advantage of the symmetry of Eq. (5.11). The experimentally measured trajectories are first

mirrored by the $\delta_L = 0$ axis, then the resultant plot is mirrored again by the $\delta_R = 0$ axis and lastly, a duplicate of the resultant plot is rotated by 90° with respect to the (0,0) point to generate Fig. 5.10b. The replicated trajectories not only span over the original experimentally inaccessible area, but also fill up the void in between the original trajectories. All of the original and replicated trajectories are normalized and shown in Fig. 5.10b, which shows close agreement with its theoretical counterpart, Fig. 5.10a, calculated with Eq. (5.11) and normalized in exactly the same way.

Chapter 6. Fabrication Process Development

Considerable effort is made to develop reliable fabrication processes for NOMS devices, which are a prerequisite for experimental NOMS research. For the multichannel micro-disk devices (Chapter 4) and the photon see-saw devices (Chapter 5), the complete fabrication process includes two main steps. The first step is to fabricate the silicon structures in the top silicon layer of silicon-on-insulator (SOI) wafers with electron beam lithography (EBL) and plasma dry etching. The second step is to selectively release the silicon structure of interest from the SiO_2 substrate with photolithography and wet etching. For the integrated hybrid plasmonic waveguide (HPWG) devices (Chapter 3), between the above two steps, an additional step is needed to pattern the metal, with electron beam lithography, metal deposition and metal lift-off.

The fabrication process development for the multichannel micro-disk devices and integrated HPWG devices was accomplished by Jong Wook Noh and Yu Chen. Based on the early work of theirs, the author developed the complete fabrication process for the photon see-saw devices, which is the focus of this chapter. The various considerations and requirements of this fabrication process development are briefly reviewed. Different fabrication process options are presented and compared.

6.1. Silicon Structure Fabrication

The most critical silicon structure in the photon see-saw devices is the photonic crystal slab and nanobeam (PCS and PCB, respectively). Fabrication and optimization of high quality PCS and PCB require well calibrated and reproducible high resolution EBL and plasma dry etching process. First, the positions and sizes of the holes in the PCS and PCB need to be controlled accurately and consistently from sample to sample. Second, the sidewall of the etched silicon structure should be smooth and vertical (90° with respect to the substrate).

Although dry etching is subsequent to the EBL process, it determines the type and thickness of the resist used in the EBL process, hence should be addressed first. In this case, the Deep Trench Etcher SLR-770 and fluorine based one-step Bosch process were selected for their reliability. Accordingly, diluted ZEP520A EBL resist was selected because of its high resolution and high etching resistance to the one-step Bosch process. (Generally, the one-step Bosch process has much higher selectivity between silicon and ZEP520A EBL resist than chlorine-based etching processes.) In order to improve the EBL resolution, ZEP520A is diluted before spin-coating and developed with developer solution in a cold bath [69]. The finalized combination of the EBL and dry etching processes are given in details in Appendix A.

A dose test was done to calibrate the above process. The e-beam current used was 100 pA and the dose was varied between 200 and 800 $\mu C/cm^2$ in ten steps – 200, 233, 272, 317, 370, 432, 504, 588, 686 and 800 $\mu C/cm^2$. It turned out that the minimum dose to clear

in the test was 432 μC/cm^2. The typical scanning electron microscope (SEM) images and measurement of the critical features in the grating couplers and PCSs are shown in Fig. 6.1, Fig. 6.2 and Table 6.1. The measurement by SEM is always calibrated with the designed periods of the grating couplers or lattice constant of the PCS. (The SEM measurement may not be accurate enough without such calibrations.)

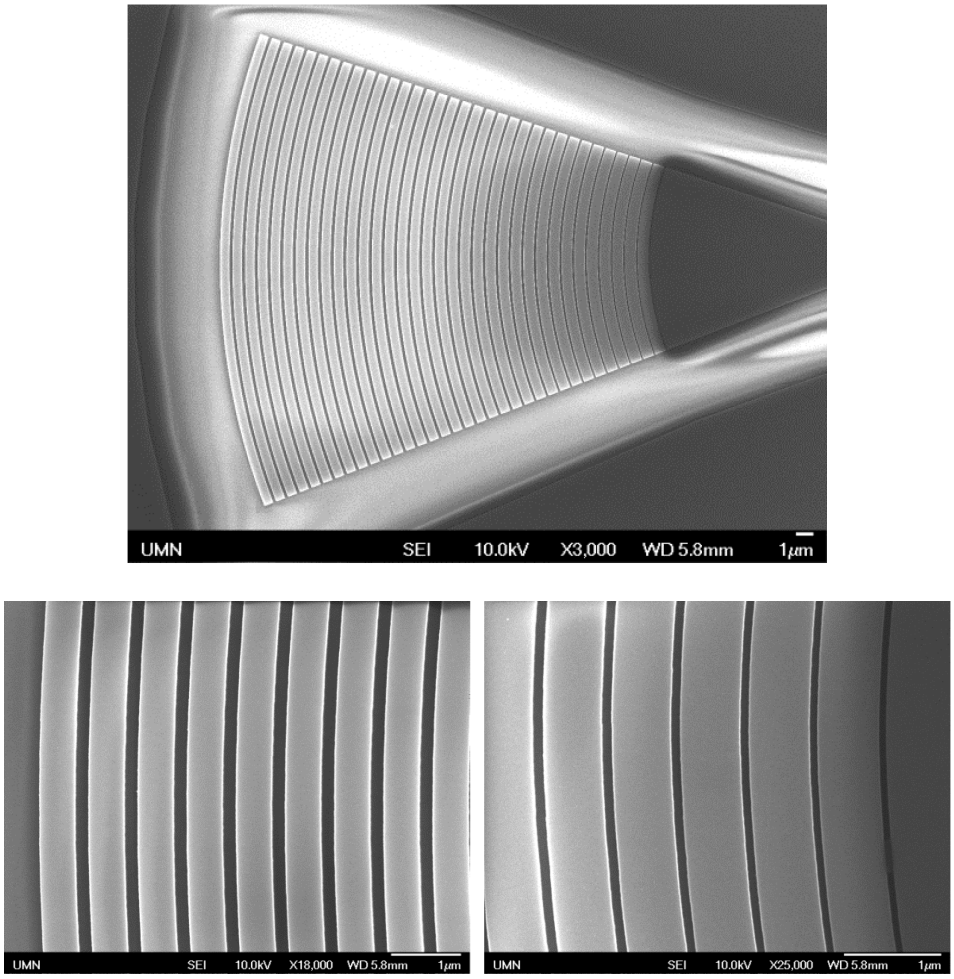

Fig. 6.1. SEM images of the grating coupler on the dose test sample.

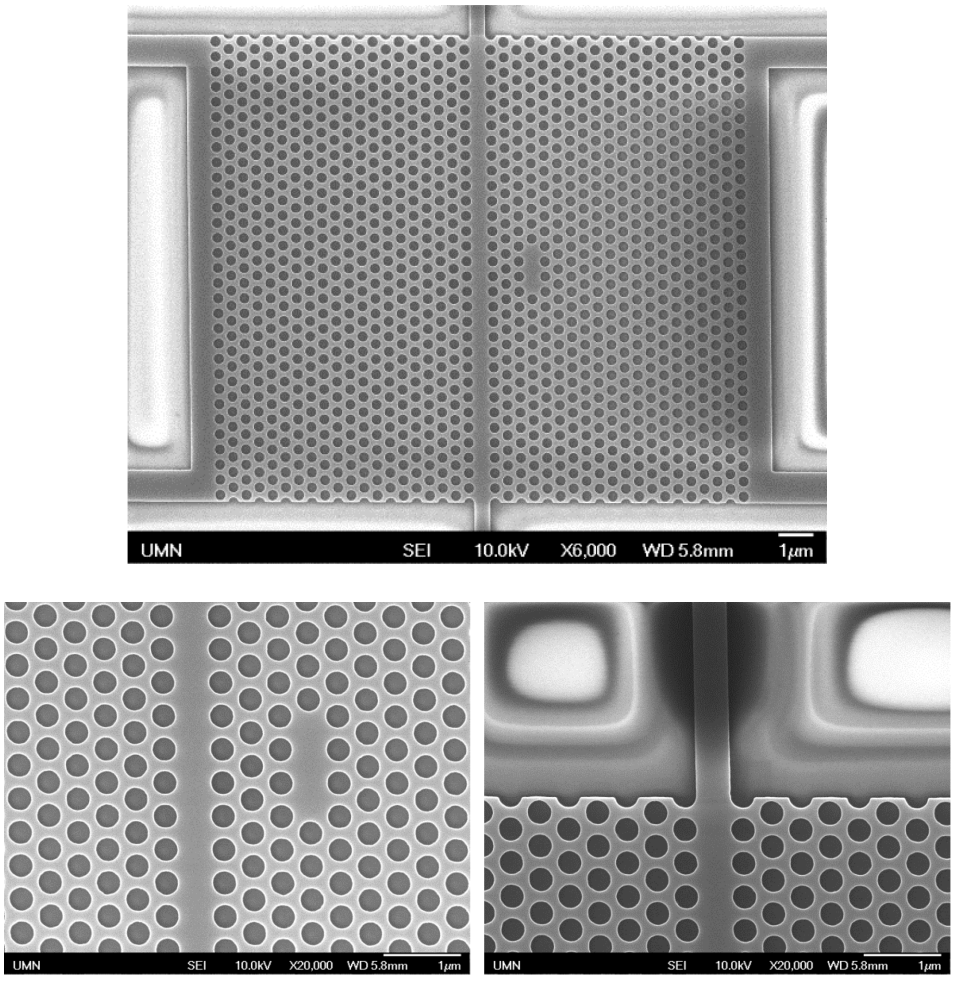

Fig. 6.2. SEM images of the photonic crystal slab on the dose test sample.

From the data in Table 6.1, it is quite clear that 800 μC/cm^2 dose results in the largest but least varied deviations (~50 nm) from the designed PCS hole sizes, as is shown in the shaded area in Table 6.1. Furthermore, from the SEM observation, it seems that higher dose results in more uniform and circular hole shapes. Therefore, 800 μC/cm^2 dose was used and all the hole sizes in the design were purposely reduced by 50 nm to

Table 6.1. Calibrated measurement results by SEM imaging.

Designed Feature Size (nm)				Actual Feature Size (nm)					
				Column 5 432 μC/cm²		Column 7 588 μC/cm²		Column 9 800 μC/cm²	
Grating Coupler Gaps	The smallest		30	63	+33	70	+40	74	+44
	Regular, Row A		138	170	+32	187	+49	196	+58
	Regular, Row J		149	181	+32	192	+43	205	+56
Photonic Crystal Holes	Row A	PCS Center	227	267	+40	270	+43	277	+50
		PCS Edge		263	+36	270	+43	277	+50
	Row J	PCS Center	272	302	+30	318	+46	322	+50
		PCS Edge		313	+41	317	+45	324	+52
Coupling Waveguides	Row A		428	382	−46	379	−49	368	−60
	Row J		513	476	−37	466	−47	457	−56

compensate the systematic error introduced by the fabrication process. Using the optimized dose and the calibrated process compensation, the critical feature size error was controlled consistently within ±5 nm, resulting in excellent and consistent device performance from sample to sample.

Silicon sidewall angle and roughness are also important factors in the EBL and dry etching processes. For PCS cavities, it is desirable to have vertical (90°) sidewalls because tilted sidewalls break the mirror symmetry and consequently scatter the quasi-TE cavity mode into the extended (not confined) quasi-TM mode, which results in additional loss and lower optical quality factor (Q) [120]. The silicon sidewall angle is determined by the resist sidewall angle after development and the dry etching process. It turned out that the EBL and dry etching processes tested here produce nearly vertical silicon sidewalls, as shown in Fig. 6.3. Meanwhile, the sidewalls in Fig. 6.3 are not perfectly smooth and show signs

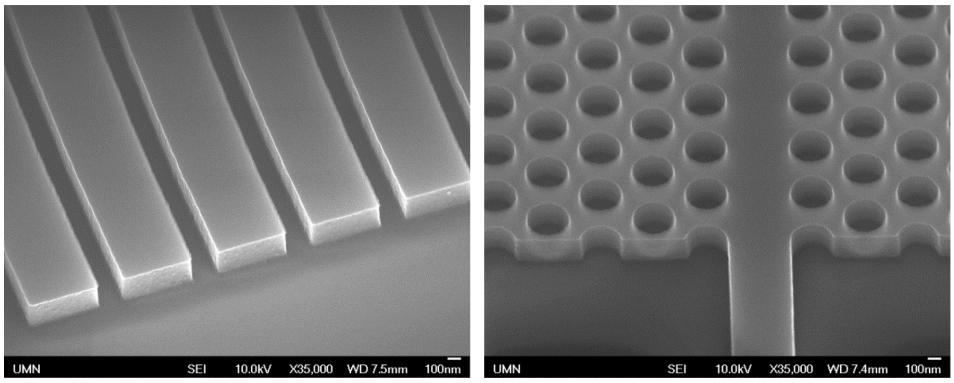

(a) (b)

Fig. 6.3. SEM images of the dry etched sidewalls.

of redeposition during the dry etching process. This turned out to be a minor problem which introduces random scattering of the light and limits the highest optical Q that can be obtained. It remains unknown whether or not this sidewall redeposition can be removed by subsequent chemical treatment.

There are other possible combinations of the EBL and dry etching processes which might be worth exploring in the long term, such as straight (not diluted) ZEP520A with chlorine based dry etching, HSQ with chlorine based dry etching and HSQ with fluorine based dry etching.

6.2. Silicon Structure Releasing

Although SiO_2 substrate etching is the second step in the releasing process, in our case it determines the photolithography process, hence should be addressed first. There are three

Table 6.2. Comparison of the pros and cons of the etchants for SiO2 substrate.

Etchant	PR Resistance	Si Resistance	Etching Rate Control	Stiction Problem
BOE	Good.	Poor.	Easy.	Yes.
Diluted HF	Poor.	Good.	Easy.	Yes.
HF Vapor	Poor but irrelevant.	Good.	Hard but possible.	No, but requires an additional aligned EBL process.

options for the etchant, each of which has its own pros and cons, as are summarized in Table 6.2.

Diluted HF solution without buffering agent attacks and penetrates photoresist (PR) very quickly hence causes serious adhesion problems. In contrast, Buffered Oxide Etch (BOE) has much better PR resistance, but attacks Si and results in very rough Si surfaces, shown in Fig. 6.4a, which is quite undesirable for achieving high optical quality factor. HF

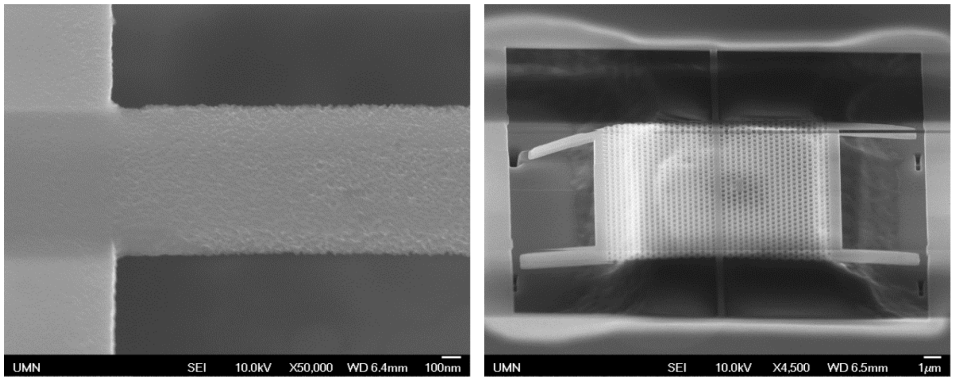

(a) (b)

Fig. 6.4. SEM images of the defective released devices.

vapor also has the same PR resistance problem as the diluted HF solution, but there is no point to use PR as the mask for HF vapor etching, as will be discussed soon. Although the PR resistance to diluted HF is poor, making it very difficult to define the releasing window, photonic crystal slab (PCS) structures can be used to support the suspended waveguide [20] and help prevent undesired undercut, which will be described in greater details at the end of this section.

The etching reactions in solutions, such as BOE and diluted HF, generally have better controlled etching rates than the etching reactions in vapor phase. As long as the ambient temperature is stable, the concentration of the etchant is carefully controlled and the amount of the etchant is sufficient, the etching rate variations for both BOE and diluted HF can be accurately and consistently controlled within ±1%. Compared with etching in solutions, vapor etching requires more complicated control of the temperature and concentration of the etchant to achieve consistent etch rate. However, it may not be necessary to have a very consistent etching rate in the case of HF vapor etching, because in principle it is possible to monitor the etching progress by taking the sample out of the HF vapor environment and measuring the etching depth with a surface profiler or AFM from time to time. In contrast, as will be discussed in more details soon, etching in solutions has an inevitable problem – stiction, which makes it impossible to directly take the sample out of the etchant, measure the etching depth and then put it back into the etchant for more etching. A convenient way to conduct HF vapor etching is to put the sample above sufficient amount of concentrated HF solution in a closed container. When thermal

equilibrium is reached, the sample will be in saturated HF vapor and the etching rate will be reasonably consistent from run to run. However, because the sample is in saturated HF vapor, this over simplified vapor etching device is prone to a detrimental effect – random condensation of small droplets of concentrated HF solution on the sample surface which leads to local non-uniform etching and possible stiction problem. This problem can be solved by creating a constant temperature gradient to disrupt the thermal equilibrium. Either keeping the concentrated HF solution at room temperature and heating up the sample or keeping the sample at room temperature and cooling down the concentrated HF solution can achieve the purpose. We have tested the latter process. The bottom of the HF container was submerged in ice-water mixture while the top of it was in air at room temperature (~20 °C). The sample was placed at the very top of the HF container which should be nearly room temperature while the concentrated HF solution should be nearly 0 °C. This house-made device effectively eliminated condensation problem and resulted in very uniform etching depth across the 6 mm by 6 mm die and reasonable etching rate about 133 nm/min.

Stiction is the most detrimental and universal problem for wet etching releasing process, therefore the use of critical point dryer (CPD) is required for BOE and diluted HF etching. The PR removal and CPD processes following the etching are long, tedious and requires great patience and care. Nevertheless, yield can still be a problem if the structure to be suspended is very soft. In addition, after the CPD is done and the delicate structure suspended in air, if the etching depth turns out to be insufficient, there is no way that a further photolithography and wet-etching can be done without destroying the devices. In

contrast, HF vapor etching is very attractive due to the circumvention of the stiction problem and the ability to suspend much softer structures than the CPD is able to do. However, the use of HF vapor etching dictates that PR cannot be use as an etching mask because good quality PR removal has to be done in solution, which kills the point to use HF vapor etching in the first place. Instead, a two-step EBL and dry etching process has to be done [123], one of which is EBL and shallow etching and the other of which is EBL and through etching. The shallow etched Si layer then can act as a hard mask during the HF vapor etching. Compared with BOE and diluted HF etching, this comes at the price of an additional EBL with accurate alignment and an additional dry etching with accurately controlled etching depth. Furthermore, the designs of the current grating couplers and waveguides have to be adjusted whenever the etching depth is changed in the shallow etching process.

Based on all the above considerations and comparisons, eventually the diluted HF etchant has been chosen. Currently we solely rely on CPD to overcome the stiction problem. It is worth noting that we were trying to use Si anchor structures to support the torsional structure so that the latter can survive the wet etching, and subsequently use focused ion beam (FIB) milling to cut the Si anchor structures and fully release the torsional structure. It is crucial to avoid Gallium ion damage [124], charging effects and the sudden release of the built-in stress in the PCS, which requires careful design and considerable practice. However, we eventually gave up this attempt due to the almost inevitable Gallium

ion damage to the PCS cavity. Fig. 6.4b shows a failed attempt to release a device, which has been pulled down and stuck to the substrate due to the charging effects.

The finalized photolithography and wet etching releasing process is given in details in Appendix B. Because the lengths of the suspended silicon structures are determined by the PCS structures that support them, instead of the sizes of exposed areas in the PR layer, generally there is no need to accurately control the feature sizes in the photolithography process. Therefore most of the parameters here can be changed as necessary. The key in the photolithography process here is to guarantee good adhesion between PR and the Si and SiO_2 surfaces, rather than accurate control of the critical feature sizes.

SEM images of the typical released torsional optomechanical devices are shown in Fig. 6.5, Fig. 6.6 and Fig. 6.7. The large and suspended piece of PCS in the center with two L3 defect cavities constitutes the torsional mass, and the two suspended strip waveguides on both sides of the torsional mass serves as the torsional springs. The releasing window in the PR layer covers the torsional mass and the torsional springs only. The two smaller pieces of PCSs anchor the torsional spring and mass, meanwhile prevent undesired undercut. Without the PCS anchors, diluted HF will penetrate between the PR layer and the SiO_2 surface and propagate a long way, usually tens of microns, along the strip waveguides. When this huge undercut happens, there is no way to control the length of the suspended torsional springs. In Fig. 6.7, it is quite evident that the etchant was contained inside the releasing window, while in Fig. 6.5 and Fig. 6.6, it can be observed that the etchant was able to penetrate the PCS anchors and propagate a little further but not very

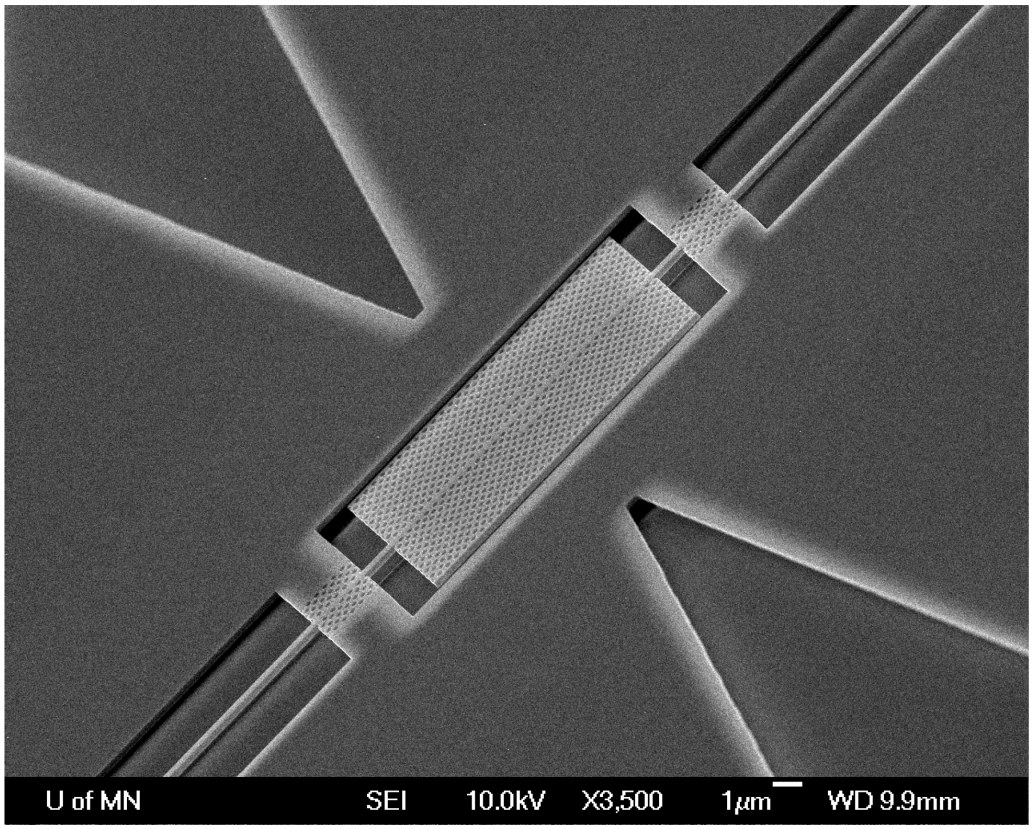

Fig. 6.5. SEM image of typical released torsional optomechanical devices.

far. In the latter case, on one hand, the lengths of the torsional springs are nevertheless very well defined by the PCS anchors. On the other hand, the penetration of the etchant can be completely avoided by simply making the PCS anchors longer or reducing the etching time if possible.

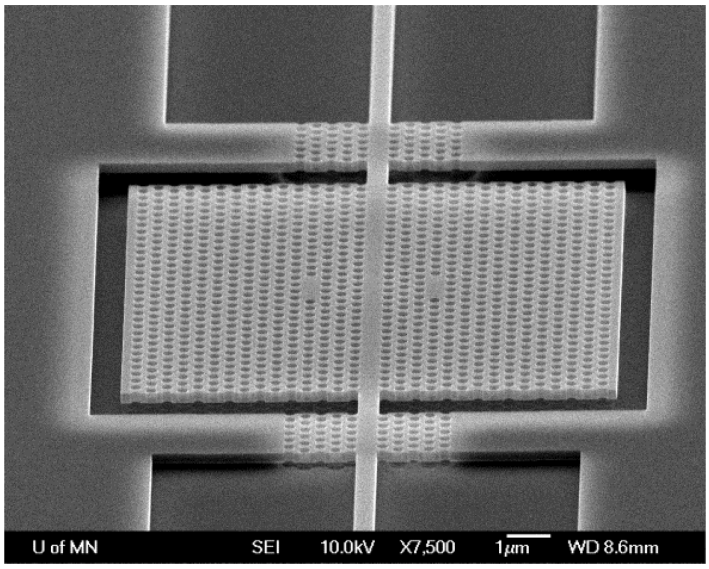

Fig. 6.6. SEM image of typical released torsional optomechanical devices.

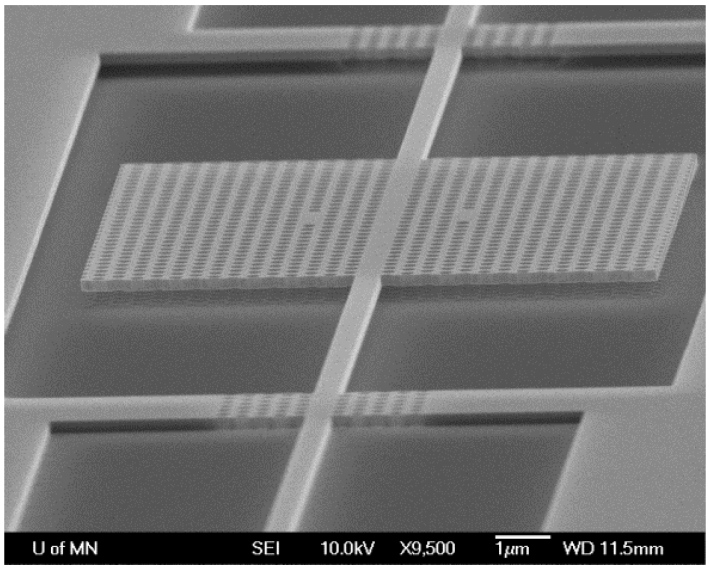

Fig. 6.7. SEM image of typical released torsional optomechanical devices.

Chapter 7. Conclusion

The concept of optical force and the general background of the NOMS research area are introduced. The general goal of the silicon photonics research area and the research presented in this dissertation is described.

The fundamental theory for optical force is summarized. The different methods to calculate optical forces are enumerated and briefly reviewed.

Integrated hybrid plasmonic waveguide (HPWG) devices have been successfully fabricated and the enhanced optical forces experimentally measured for the first time [35]. When light interacts with metal in close proximity, the generated optical forces are enhanced by 1 or 2 orders of magnitude, compared with the cases where no metal is present.

All-optical amplification of RF signals has been successfully demonstrated [34]. The optical force generated by one laser is used to mechanically change the optical path and hence the output power of another laser. In addition, completely optically tunable mechanical nonlinear behavior has been demonstrated for the first time and systematically studied.

Optomechanical photon shuttling between photonic cavities has been demonstrated with a "photon see-saw" device [29]. This photon see-saw is a novel multicavity optomechanical device which consists of two photonic crystal nanocavities, one on each side of it. Pumping photons into one cavity excites torsional optomechanical self-

oscillation, which shuttles photons to the other empty cavity during every oscillation cycle in a well-regulated fashion.

The effort made to develop reliable fabrication processes for NOMS devices is summarized. The various considerations and requirements of this fabrication process development are briefly reviewed. Different fabrication process options are presented and compared.

Future research efforts on the NOMS integrated on silicon photonics platforms (or more generally, NOMS realized on any platforms) may be dedicated in the following directions. The first is to explore the quantum nature of the interactions between light and matter in NOMS, by pursuing single photon operations or non-classical light generation and manipulation. The second is to investigate the wealth of dynamics in the side-band-resolved regime, where the time scale of the mechanical motion is comparable to the cavity photon lifetime. The third is to incorporate more and more optical and mechanical systems into a NOMS device to realize sophisticated functionalities. Last but not least, because NOMS device generally can be employed for ultrasensitive force, acceleration or displacement measurement, further improvement of the measurement sensitivity and the development of NOMS sensors for practical applications are important goals.

Bibliography

[1] J. Kepler, *De Cometis Libelli Tres*. 1619.

[2] J. R. Moffitt, Y. R. Chemla, S. B. Smith, and C. Bustamante, "Recent advances in optical tweezers.," *Annu. Rev. Biochem.*, vol. 77, pp. 205–28, Jan. 2008.

[3] A. Ashkin, J. M. Dziedzic, J. E. Bjorkholm, and S. Chu, "Observation of a single-beam gradient force optical trap for dielectric particles," *Opt. Lett.*, vol. 11, no. 5, p. 288, May 1986.

[4] V. B. Braginsky, S. E. Strigin, and S. P. Vyatchanin, "Parametric oscillatory instability in Fabry–Perot interferometer," *Phys. Lett. A*, vol. 287, no. 5–6, pp. 331–338, Sep. 2001.

[5] V. B. Braginsky, S. E. Strigin, and S. P. Vyatchanin, "Analysis of parametric oscillatory instability in power recycled LIGO interferometer," *Phys. Lett. A*, vol. 305, no. 3–4, pp. 111–124, Dec. 2002.

[6] H. Rokhsari, T. J. Kippenberg, T. Carmon, and K. J. Vahala, "Radiation-pressure-driven micro-mechanical oscillator," *Opt. Express*, vol. 13, no. 14, p. 5293, 2005.

[7] T. Kippenberg, H. Rokhsari, T. Carmon, A. Scherer, and K. Vahala, "Analysis of Radiation-Pressure Induced Mechanical Oscillation of an Optical Microcavity," *Phys. Rev. Lett.*, vol. 95, no. 3, p. 033901, Jul. 2005.

[8] T. J. Kippenberg and K. J. Vahala, "Cavity Opto-Mechanics," *Opt. Express*, vol. 15, no. 25, p. 17172, Dec. 2007.

[9] T. J. Kippenberg and K. J. Vahala, "Cavity optomechanics: back-action at the mesoscale.," *Science*, vol. 321, no. 5893, pp. 1172–6, Aug. 2008.

[10] M. Aspelmeyer, T. J. Kippenberg, and F. Marquardt, "Cavity Optomechanics," p. 65, Mar. 2013.

[11] A. Schliesser, P. Del'Haye, N. Nooshi, K. Vahala, and T. Kippenberg, "Radiation Pressure Cooling of a Micromechanical Oscillator Using Dynamical Backaction," *Phys. Rev. Lett.*, vol. 97, no. 24, p. 243905, Dec. 2006.

[12] J. Chan, T. P. M. Alegre, A. H. Safavi-Naeini, J. T. Hill, A. Krause, S. Gröblacher, M. Aspelmeyer, and O. Painter, "Laser cooling of a nanomechanical oscillator into its quantum ground state.," *Nature*, vol. 478, no. 7367, pp. 89–92, Oct. 2011.

[13] S. Gigan, H. R. Böhm, M. Paternostro, F. Blaser, G. Langer, J. B. Hertzberg, K. C. Schwab, D. Bäuerle, M. Aspelmeyer, and A. Zeilinger, "Self-cooling of a micromirror by radiation pressure.," *Nature*, vol. 444, no. 7115, pp. 67–70, Nov. 2006.

[14] O. Arcizet, P.-F. Cohadon, T. Briant, M. Pinard, and A. Heidmann, "Radiation-pressure cooling and optomechanical instability of a micromirror.," *Nature*, vol. 444, no. 7115, pp. 71–4, Nov. 2006.

[15] J. D. Thompson, B. M. Zwickl, A. M. Jayich, F. Marquardt, S. M. Girvin, and J. G. E. Harris, "Strong dispersive coupling of a high-finesse cavity to a micromechanical membrane.," *Nature*, vol. 452, no. 7183, pp. 72–5, Mar. 2008.

[16] M. Li, W. H. P. Pernice, C. Xiong, T. Baehr-Jones, M. Hochberg, and H. X. Tang, "Harnessing optical forces in integrated photonic circuits.," *Nature*, vol. 456, no. 7221, pp. 480–4, Nov. 2008.

[17] M. Eichenfield, R. Camacho, J. Chan, K. J. Vahala, and O. Painter, "A picogram- and nanometre-scale photonic-crystal optomechanical cavity.," *Nature*, vol. 459, no. 7246, pp. 550–5, May 2009.

[18] M. Eichenfield, J. Chan, R. M. Camacho, K. J. Vahala, and O. Painter, "Optomechanical crystals.," *Nature*, vol. 462, no. 7269, pp. 78–82, Nov. 2009.

[19] G. S. Wiederhecker, L. Chen, A. Gondarenko, and M. Lipson, "Controlling photonic structures using optical forces.," *Nature*, vol. 462, no. 7273, pp. 633–6, Dec. 2009.

[20] M. Li, W. H. P. Pernice, and H. X. Tang, "Tunable bipolar optical interactions between guided lightwaves," *Nat. Photonics*, vol. 3, no. 8, pp. 464–468, Jul. 2009.

[21] J. C. Sankey, C. Yang, B. M. Zwickl, A. M. Jayich, and J. G. E. Harris, "Strong and tunable nonlinear optomechanical coupling in a low-loss system," *Nat. Phys.*, vol. 6, no. 9, pp. 707–712, Jun. 2010.

[22] S. Weis, R. Rivière, S. Deléglise, E. Gavartin, O. Arcizet, A. Schliesser, and T. J. Kippenberg, “Optomechanically induced transparency.,” *Science*, vol. 330, no. 6010, pp. 1520–3, Dec. 2010.

[23] A. H. Safavi-Naeini, T. P. Mayer Alegre, J. Chan, M. Eichenfield, M. Winger, Q. Lin, J. T. Hill, D. E. Chang, and O. Painter, “Electromagnetically induced transparency and slow light with optomechanics.,” *Nature*, vol. 472, no. 7341, pp. 69–73, Apr. 2011.

[24] M. Bagheri, M. Poot, M. Li, W. P. H. Pernice, and H. X. Tang, “Dynamic manipulation of nanomechanical resonators in the high-amplitude regime and non-volatile mechanical memory operation.,” *Nat. Nanotechnol.*, vol. 6, no. 11, pp. 726–32, Nov. 2011.

[25] M. Zhang, G. S. Wiederhecker, S. Manipatruni, A. Barnard, P. McEuen, and M. Lipson, “Synchronization of Micromechanical Oscillators Using Light,” *Phys. Rev. Lett.*, vol. 109, no. 23, p. 233906, Dec. 2012.

[26] E. Verhagen, S. Deléglise, S. Weis, A. Schliesser, and T. J. Kippenberg, “Quantum-coherent coupling of a mechanical oscillator to an optical cavity mode.,” *Nature*, vol. 482, no. 7383, pp. 63–7, Feb. 2012.

[27] A. H. Safavi-Naeini, S. Gröblacher, J. T. Hill, J. Chan, M. Aspelmeyer, and O. Painter, “Squeezed light from a silicon micromechanical resonator.,” *Nature*, vol. 500, no. 7461, pp. 185–9, Aug. 2013.

[28] A. B. Shkarin, N. E. Flowers-Jacobs, S. W. Hoch, A. D. Kashkanova, C. Deutsch, J. Reichel, and J. G. E. Harris, “Optically Mediated Hybridization between Two Mechanical Modes,” *Phys. Rev. Lett.*, vol. 112, no. 1, p. 013602, Jan. 2014.

[29] H. Li and M. Li, “Optomechanical photon shuttling between photonic cavities,” *Nat. Nanotechnol.*, vol. 9, no. 11, pp. 913–919, Sep. 2014.

[30] G. T. Reed and A. P. Knights, *Silicon Photonics: An Introduction*. John Wiley & Sons, Ltd, 2004.

[31] V. R. Almeida, C. A. Barrios, R. R. Panepucci, and M. Lipson, “All-optical control of light on a silicon chip.,” *Nature*, vol. 431, no. 7012, pp. 1081–4, Oct. 2004.

[32] M. Lipson, “Guiding, modulating, and emitting light on Silicon-challenges and opportunities,” *J. Light. Technol.*, vol. 23, no. 12, pp. 4222–4238, Dec. 2005.

[33] B. Jalali and S. Fathpour, “Silicon Photonics,” *J. Light. Technol.*, vol. 24, no. 12, pp. 4600–4615, Dec. 2006.

[34] H. Li, Y. Chen, J. Noh, S. Tadesse, and M. Li, “Multichannel cavity optomechanics for all-optical amplification of radio frequency signals.,” *Nat. Commun.*, vol. 3, p. 1091, Jan. 2012.

[35] H. Li, J. W. Noh, Y. Chen, and M. Li, “Enhanced optical forces in integrated hybrid plasmonic waveguides.,” *Opt. Express*, vol. 21, no. 10, pp. 11839–51, May 2013.

[36] S. M. Barnett and R. Loudon, “On the electromagnetic force on a dielectric medium,” *J. Phys. B At. Mol. Opt. Phys.*, vol. 39, no. 15, pp. S671–S684, Aug. 2006.

[37] A. R. Zakharian, P. Polynkin, M. Mansuripur, and J. V. Moloney, “Single-beam trapping of micro-beads in polarized light: Numerical simulations,” *Opt. Express*, vol. 14, no. 8, p. 3660, 2006.

[38] R. Loudon and S. M. Barnett, “Theory of the radiation pressure on dielectric slabs, prisms and single surfaces,” *Opt. Express*, vol. 14, no. 24, p. 11855, 2006.

[39] M. Mansuripur, A. R. Zakharian, and E. M. Wright, “Electromagnetic-force distribution inside matter,” *Phys. Rev. A*, vol. 88, no. 2, p. 023826, Aug. 2013.

[40] J. D. Jackson, *Classical Electrodynamics*, 3rd ed. John Wiley & Sons, 1999.

[41] S. M. Barnett and R. Loudon, “The enigma of optical momentum in a medium.,” *Philos. Trans. A. Math. Phys. Eng. Sci.*, vol. 368, no. 1914, pp. 927–39, Mar. 2010.

[42] C. Baxter and R. Loudon, “Radiation pressure and the photon momentum in dielectrics,” *J. Mod. Opt.*, vol. 57, no. 10, pp. 830–842, Jun. 2010.

[43] L. D. Landau, E. M. Lifshitz, and L. P. Pitaevskii, *Electrodynamics of Continuous Media*, 2nd ed. Pergamon Press, 1984.

[44] P. T. Rakich, M. A. Popović, and Z. Wang, “General treatment of optical forces and potentials in mechanically variable photonic systems.,” *Opt. Express*, vol. 17, no. 20, pp. 18116–35, Sep. 2009.

[45] P. T. Rakich, Z. Wang, and P. Davids, “Scaling of optical forces in dielectric waveguides: rigorous connection between radiation pressure and dispersion.,” *Opt. Lett.*, vol. 36, no. 2, pp. 217–9, Jan. 2011.

[46] J. Rosenberg, Q. Lin, and O. Painter, “Static and dynamic wavelength routing via the gradient optical force,” *Nat. Photonics*, vol. 3, no. 8, pp. 478–483, Jul. 2009.

[47] F. Marquardt and S. Girvin, “Optomechanics,” *Physics (College. Park. Md).*, vol. 2, p. 40, May 2009.

[48] A. Nunnenkamp, K. Børkje, and S. M. Girvin, “Single-Photon Optomechanics,” *Phys. Rev. Lett.*, vol. 107, no. 6, p. 063602, Aug. 2011.

[49] M. Li, W. H. P. Pernice, and H. X. Tang, “Broadband all-photonic transduction of nanocantilevers.,” *Nat. Nanotechnol.*, vol. 4, no. 6, pp. 377–82, Jun. 2009.

[50] K. Srinivasan, H. Miao, M. T. Rakher, M. Davanço, and V. Aksyuk, “Optomechanical transduction of an integrated silicon cantilever probe using a microdisk resonator.,” *Nano Lett.*, vol. 11, no. 2, pp. 791–7, Feb. 2011.

[51] K. Y. Fong, W. H. P. P. Pernice, M. Li, and H. X. Tang, “Tunable optical coupler controlled by optical gradient forces.,” *Opt. Express*, vol. 19, no. 16, pp. 15098–108, Aug. 2011.

[52] C. Xiong, W. H. P. Pernice, X. Sun, C. Schuck, K. Y. Fong, and H. X. Tang, “Aluminum nitride as a new material for chip-scale optomechanics and nonlinear optics,” *New J. Phys.*, vol. 14, no. 9, p. 095014, Sep. 2012.

[53] S. A. Maier, *Plasmonics: Fundamentals and Applications*. Springer, 2007.

[54] D. K. Gramotnev and S. I. Bozhevolnyi, “Plasmonics beyond the diffraction limit,” *Nat. Photonics*, vol. 4, no. 2, pp. 83–91, Jan. 2010.

[55] X. Yang, Y. Liu, R. F. Oulton, X. Yin, and X. Zhang, “Optical forces in hybrid plasmonic waveguides.,” *Nano Lett.*, vol. 11, no. 2, pp. 321–8, Feb. 2011.

[56] X. Yang, A. Ishikawa, X. Yin, and X. Zhang, “Hybrid photonic-plasmonic crystal nanocavities.,” *ACS Nano*, vol. 5, no. 4, pp. 2831–8, Apr. 2011.

[57] C. Huang and L. Zhu, “Enhanced optical forces in 2D hybrid and plasmonic waveguides.,” *Opt. Lett.*, vol. 35, no. 10, pp. 1563–5, May 2010.

[58] V. J. Sorger, Z. Ye, R. F. Oulton, Y. Wang, G. Bartal, X. Yin, and X. Zhang, "Experimental demonstration of low-loss optical waveguiding at deep sub-wavelength scales," *Nat. Commun.*, vol. 2, p. 331, May 2011.

[59] M. Liu, T. Zentgraf, Y. Liu, G. Bartal, and X. Zhang, "Light-driven nanoscale plasmonic motors.," *Nat. Nanotechnol.*, vol. 5, no. 8, pp. 570–3, Aug. 2010.

[60] M. L. Povinelli, M. Loncar, M. Ibanescu, E. J. Smythe, S. G. Johnson, F. Capasso, and J. D. Joannopoulos, "Evanescent-wave bonding between optical waveguides," *Opt. Lett.*, vol. 30, no. 22, p. 3042, Nov. 2005.

[61] W. H. P. Pernice, M. Li, and H. X. Tang, "Theoretical investigation of the transverse optical force between a silicon nanowire waveguide and a substrate," *Opt. Express*, vol. 17, no. 3, p. 1806, Jan. 2009.

[62] R. F. Oulton, V. J. Sorger, D. A. Genov, D. F. P. Pile, and X. Zhang, "A hybrid plasmonic waveguide for subwavelength confinement and long-range propagation," *Nat. Photonics*, vol. 2, no. 8, pp. 496–500, Jul. 2008.

[63] P. Nagpal, N. C. Lindquist, S.-H. Oh, and D. J. Norris, "Ultrasmooth patterned metals for plasmonics and metamaterials.," *Science*, vol. 325, no. 5940, pp. 594–7, Jul. 2009.

[64] L. Yin, V. K. Vlasko-Vlasov, J. Pearson, J. M. Hiller, J. Hua, U. Welp, D. E. Brown, and C. W. Kimball, "Subwavelength Focusing and Guiding of Surface Plasmons," *Nano Lett.*, vol. 5, no. 7, pp. 1399–1402, Jul. 2005.

[65] M. Kuttge, E. J. R. Vesseur, J. Verhoeven, H. J. Lezec, H. A. Atwater, and A. Polman, "Loss mechanisms of surface plasmon polaritons on gold probed by cathodoluminescence imaging spectroscopy.," *Appl. Phys. Lett.*, vol. 93, no. 11, p. 113110, Sep. 2008.

[66] P. B. Johnson and R. W. Christy, "Optical Constants of the Noble Metals," *Phys. Rev. B*, vol. 6, no. 12, pp. 4370–4379, Dec. 1972.

[67] M. V. Salapaka, H. S. Bergh, J. Lai, A. Majumdar, and E. McFarland, "Multi-mode noise analysis of cantilevers for scanning probe microscopy," *J. Appl. Phys.*, vol. 81, no. 6, p. 2480, Mar. 1997.

[68] S. Timoshenko, *Vibration Problems in Engineering*, 2nd ed. New York: D. Van Nostrand company, inc., 1937.

[69] M. A. Mohammad, K. Koshelev, T. Fito, D. A. Z. Zheng, M. Stepanova, and S. Dew, “Study of Development Processes for ZEP-520 as a High-Resolution Positive and Negative Tone Electron Beam Lithography Resist,” *Jpn. J. Appl. Phys.*, vol. 51, no. 6, p. 06FC05, Jun. 2012.

[70] P. T. Rakich, M. A. Popović, M. Soljačić, and E. P. Ippen, “Trapping, corralling and spectral bonding of optical resonances through optically induced potentials,” *Nat. Photonics*, vol. 1, no. 11, pp. 658–665, Nov. 2007.

[71] M. Notomi, H. Taniyama, S. Mitsugi, and E. Kuramochi, “Optomechanical Wavelength and Energy Conversion in High-Q Double-Layer Cavities of Photonic Crystal Slabs,” *Phys. Rev. Lett.*, vol. 97, no. 2, p. 023903, Jul. 2006.

[72] R. Chatterjee, M. Yu, A. Stein, D.-L. Kwong, L. C. Kimerling, and C. W. Wong, “Demonstration of a hitless bypass switch using nanomechanical perturbation for high-bitrate transparent networks.,” *Opt. Express*, vol. 18, no. 3, pp. 3045–58, Feb. 2010.

[73] A. Schliesser, O. Arcizet, R. Rivière, G. Anetsberger, and T. J. Kippenberg, “Resolved-sideband cooling and position measurement of a micromechanical oscillator close to the Heisenberg uncertainty limit,” *Nat. Phys.*, vol. 5, no. 7, pp. 509–514, Jun. 2009.

[74] J. D. Teufel, T. Donner, D. Li, J. W. Harlow, M. S. Allman, K. Cicak, A. J. Sirois, J. D. Whittaker, K. W. Lehnert, and R. W. Simmonds, “Sideband cooling of micromechanical motion to the quantum ground state.,” *Nature*, vol. 475, no. 7356, pp. 359–63, Jul. 2011.

[75] S. Gröblacher, K. Hammerer, M. R. Vanner, and M. Aspelmeyer, “Observation of strong coupling between a micromechanical resonator and an optical cavity field.,” *Nature*, vol. 460, no. 7256, pp. 724–7, Aug. 2009.

[76] M. Hossein-Zadeh and K. J. Vahala, “An Optomechanical Oscillator on a Silicon Chip,” *IEEE J. Sel. Top. Quantum Electron.*, vol. 16, no. 1, pp. 276–287, 2010.

[77] M. Hossein-Zadeh and K. J. Vahala, “Observation of injection locking in an optomechanical rf oscillator,” *Appl. Phys. Lett.*, vol. 93, no. 19, p. 191115, Nov. 2008.

[78] G. Anetsberger, O. Arcizet, Q. P. Unterreithmeier, R. Rivière, A. Schliesser, E. M. Weig, J. P. Kotthaus, and T. J. Kippenberg, "Near-field cavity optomechanics with nanomechanical oscillators," *Nat. Phys.*, vol. 5, no. 12, pp. 909–914, Oct. 2009.

[79] M. Li, W. H. P. Pernice, and H. X. Tang, "Reactive Cavity Optical Force on Microdisk-Coupled Nanomechanical Beam Waveguides," *Phys. Rev. Lett.*, vol. 103, no. 22, p. 223901, Nov. 2009.

[80] M. Oxborrow, "Traceable 2-D Finite-Element Simulation of the Whispering-Gallery Modes of Axisymmetric Electromagnetic Resonators," *IEEE Trans. Microw. Theory Tech.*, vol. 55, no. 6, pp. 1209–1218, Jun. 2007.

[81] M. L. Gorodetsky, A. Schliesser, G. Anetsberger, S. Deleglise, and T. J. Kippenberg, "Determination of the vacuum optomechanical coupling rate using frequency noise calibration.," *Opt. Express*, vol. 18, no. 22, pp. 23236–46, Oct. 2010.

[82] D. Kleckner and D. Bouwmeester, "Sub-kelvin optical cooling of a micromechanical resonator.," *Nature*, vol. 444, no. 7115, pp. 75–8, Nov. 2006.

[83] R. Lifshitz and M. C. Cross, "Nonlinear Dynamics of Nanomechanical Resonators," in *Nonlinear Dynamics of Nanosystems*, G. Radons, B. Rumpf, and H. G. Schuster, Eds. Weinheim, Germany: Wiley-VCH Verlag GmbH & Co. KGaA, 2010.

[84] A. H. Nayfeh and D. T. Mook, *Nonlinear oscillations*. New York: Wiley, 1979.

[85] N. Kacem, J. Arcamone, F. Perez-Murano, and S. Hentz, "Dynamic range enhancement of nonlinear nanomechanical resonant cantilevers for highly sensitive NEMS gas/mass sensor applications," *J. Micromechanics Microengineering*, vol. 20, no. 4, p. 045023, Apr. 2010.

[86] R. B. Karabalin, R. Lifshitz, M. C. Cross, M. H. Matheny, S. C. Masmanidis, and M. L. Roukes, "Signal Amplification by Sensitive Control of Bifurcation Topology," *Phys. Rev. Lett.*, vol. 106, no. 9, p. 094102, Feb. 2011.

[87] M. Cross, A. Zumdieck, R. Lifshitz, and J. Rogers, "Synchronization by Nonlinear Frequency Pulling," *Phys. Rev. Lett.*, vol. 93, no. 22, p. 224101, Nov. 2004.

[88] J. S. Aldridge and A. N. Cleland, “Noise-Enabled Precision Measurements of a Duffing Nanomechanical Resonator,” *Phys. Rev. Lett.*, vol. 94, no. 15, p. 156403, Apr. 2005.

[89] M. Dykman and D. Ryvkine, “Activated Escape of Periodically Modulated Systems,” *Phys. Rev. Lett.*, vol. 94, no. 7, p. 070602, Feb. 2005.

[90] J.-P. Raskin, A. R. Brown, B. Khuri-Yakub, and G. M. Rebeiz, “A novel parametric-effect MEMS amplifier,” *J. Microelectromechanical Syst.*, vol. 9, no. 4, pp. 528–537, Dec. 2000.

[91] F. Massel, T. T. Heikkilä, J.-M. Pirkkalainen, S. U. Cho, H. Saloniemi, P. J. Hakonen, and M. A. Sillanpää, “Microwave amplification with nanomechanical resonators.,” *Nature*, vol. 480, no. 7377, pp. 351–4, Dec. 2011.

[92] M. Soltani, S. Yegnanarayanan, and A. Adibi, “Ultra-high Q planar silicon microdisk resonators for chip-scale silicon photonics,” *Opt. Express*, vol. 15, no. 8, p. 4694, 2007.

[93] M. Li, H. X. Tang, and M. L. Roukes, “Ultra-sensitive NEMS-based cantilevers for sensing, scanned probe and very high-frequency applications.,” *Nat. Nanotechnol.*, vol. 2, no. 2, pp. 114–20, Feb. 2007.

[94] X. L. Feng, C. J. White, A. Hajimiri, and M. L. Roukes, “A self-sustaining ultrahigh-frequency nanoelectromechanical oscillator.,” *Nat. Nanotechnol.*, vol. 3, no. 6, pp. 342–6, Jun. 2008.

[95] V. Pott, H. Kam, R. Nathanael, J. Jeon, E. Alon, and T.-J. King Liu, “Mechanical Computing Redux: Relays for Integrated Circuit Applications,” *Proc. IEEE*, vol. 98, no. 12, pp. 2076–2094, Dec. 2010.

[96] T.-H. Lee, S. Bhunia, and M. Mehregany, “Electromechanical computing at 500 degrees C with silicon carbide.,” *Science*, vol. 329, no. 5997, pp. 1316–8, Sep. 2010.

[97] J. Ma and M. L. Povinelli, “Large tuning of birefringence in two strip silicon waveguides via optomechanical motion.,” *Opt. Express*, vol. 17, no. 20, pp. 17818–28, Sep. 2009.

[98] S. Johnson, M. Ibanescu, M. Skorobogatiy, O. Weisberg, J. Joannopoulos, and Y. Fink, "Perturbation theory for Maxwell's equations with shifting material boundaries," *Phys. Rev. E*, vol. 65, no. 6, p. 066611, Jun. 2002.

[99] K. J. Vahala, "Optical microcavities.," *Nature*, vol. 424, no. 6950, pp. 839–46, Aug. 2003.

[100] S. Noda, M. Fujita, and T. Asano, "Spontaneous-emission control by photonic crystals and nanocavities," *Nat. Photonics*, vol. 1, no. 8, pp. 449–458, Aug. 2007.

[101] J. L. O'Brien, A. Furusawa, and J. Vučković, "Photonic quantum technologies," *Nat. Photonics*, vol. 3, no. 12, pp. 687–695, Dec. 2009.

[102] K. Nozaki, T. Tanabe, A. Shinya, S. Matsuo, T. Sato, H. Taniyama, and M. Notomi, "Sub-femtojoule all-optical switching using a photonic-crystal nanocavity," *Nat. Photonics*, vol. 4, no. 7, pp. 477–483, May 2010.

[103] A. Yariv, Y. Xu, R. K. Lee, and A. Scherer, "Coupled-resonator optical waveguide: a proposal and analysis," *Opt. Lett.*, vol. 24, no. 11, p. 711, Jun. 1999.

[104] Y. Vlasov, W. M. J. Green, and F. Xia, "High-throughput silicon nanophotonic wavelength-insensitive switch for on-chip optical networks," *Nat. Photonics*, vol. 2, no. 4, pp. 242–246, Mar. 2008.

[105] X. Yang, M. Yu, D.-L. Kwong, and C. Wong, "All-Optical Analog to Electromagnetically Induced Transparency in Multiple Coupled Photonic Crystal Cavities," *Phys. Rev. Lett.*, vol. 102, no. 17, p. 173902, Apr. 2009.

[106] P. B. Deotare, M. W. McCutcheon, I. W. Frank, M. Khan, and M. Lončar, "Coupled photonic crystal nanobeam cavities," *Appl. Phys. Lett.*, vol. 95, no. 3, p. 031102, 2009.

[107] Y. Sato, Y. Tanaka, J. Upham, Y. Takahashi, T. Asano, and S. Noda, "Strong coupling between distant photonic nanocavities and its dynamic control," *Nat. Photonics*, vol. 6, no. 1, pp. 56–61, Dec. 2011.

[108] D. Wilson, C. Regal, S. Papp, and H. Kimble, "Cavity Optomechanics with Stoichiometric SiN Films," *Phys. Rev. Lett.*, vol. 103, no. 20, p. 207204, Nov. 2009.

[109] Y.-S. Park and H. Wang, “Resolved-sideband and cryogenic cooling of an optomechanical resonator,” *Nat. Phys.*, vol. 5, no. 7, pp. 489–493, Jun. 2009.

[110] L. Ding, C. Baker, P. Senellart, A. Lemaitre, S. Ducci, G. Leo, and I. Favero, “High Frequency GaAs Nano-Optomechanical Disk Resonator,” *Phys. Rev. Lett.*, vol. 105, no. 26, p. 263903, Dec. 2010.

[111] M. Bagheri, M. Poot, L. Fan, F. Marquardt, and H. X. Tang, “Photonic Cavity Synchronization of Nanomechanical Oscillators,” *Phys. Rev. Lett.*, vol. 111, no. 21, p. 213902, Nov. 2013.

[112] G. Heinrich, J. G. E. Harris, and F. Marquardt, “Photon shuttle: Landau-Zener-Stückelberg dynamics in an optomechanical system,” *Phys. Rev. A*, vol. 81, no. 1, p. 011801, Jan. 2010.

[113] Q. Quan, P. B. Deotare, and M. Loncar, “Photonic crystal nanobeam cavity strongly coupled to the feeding waveguide,” *Appl. Phys. Lett.*, vol. 96, no. 20, p. 203102, May 2010.

[114] Q. Quan and M. Loncar, “Deterministic design of wavelength scale, ultra-high Q photonic crystal nanobeam cavities.,” *Opt. Express*, vol. 19, no. 19, pp. 18529–42, Sep. 2011.

[115] D. A. Fuhrmann, S. M. Thon, H. Kim, D. Bouwmeester, P. M. Petroff, A. Wixforth, and H. J. Krenner, “Dynamic modulation of photonic crystal nanocavities using gigahertz acoustic phonons,” *Nat. Photonics*, vol. 5, no. 10, pp. 605–609, Sep. 2011.

[116] D. Bouwmeester, N. Dekker, F. Dorsselaer, C. Schrama, P. Visser, and J. Woerdman, “Observation of Landau-Zener dynamics in classical optical systems,” *Phys. Rev. A*, vol. 51, no. 1, pp. 646–654, Jan. 1995.

[117] J. A. J. Burgess, A. E. Fraser, F. F. Sani, D. Vick, B. D. Hauer, J. P. Davis, and M. R. Freeman, “Quantitative magneto-mechanical detection and control of the Barkhausen effect.,” *Science*, vol. 339, no. 6123, pp. 1051–4, Mar. 2013.

[118] P. H. Kim, C. Doolin, B. D. Hauer, A. J. R. MacDonald, M. R. Freeman, P. E. Barclay, and J. P. Davis, “Nanoscale torsional optomechanics,” *Appl. Phys. Lett.*, vol. 102, no. 5, p. 053102, Feb. 2013.

[119] A. G. Krause, M. Winger, T. D. Blasius, Q. Lin, and O. Painter, "A high-resolution microchip optomechanical accelerometer," *Nat. Photonics*, vol. 6, no. 11, pp. 768–772, Oct. 2012.

[120] J. D. Joannopoulos, S. G. Johnson, J. N. Winn, and R. D. Meade, *Photonic Crystals: Molding the Flow of Light*, 2nd ed. Princeton University Press, 2008.

[121] H. A. Haus, *Waves and Fields in Optoelectronics*. Englewood Cliffs: Prentice-Hall, Inc., Englewood Cliffs, New Jersey, 1984.

[122] S. Fan, W. Suh, and J. D. Joannopoulos, "Temporal coupled-mode theory for the Fano resonance in optical resonators," *J. Opt. Soc. Am. A*, vol. 20, no. 3, p. 569, Mar. 2003.

[123] F. Tian, G. Zhou, Y. Du, F. S. Chau, J. Deng, X. Tang, and R. Akkipeddi, "Energy-efficient utilization of bipolar optical forces in nano-optomechanical cavities.," *Opt. Express*, vol. 21, no. 15, pp. 18398–407, Jul. 2013.

[124] C. Lehrer, L. Frey, S. Petersen, M. Mizutani, M. Takai, and H. Ryssel, "Defects and gallium-contamination during focused ion beam micro machining," in *2000 International Conference on Ion Implantation Technology Proceedings. Ion Implantation Technology - 2000 (Cat. No.00EX432)*, pp. 695–698.

Appendix A. EBL and Dry Etching Processes

The EBL and dry etching processes have been finalized and elaborated below, although there is still room for future resolution optimization, if necessary. Minor adjustments are sometimes needed, such as the priming method and EBL thermal drift calibration interval.

1. Cleave and rinse the sample: standard SOI with 220 nm Si on top of 3 μm SiO_2.
2. Clean the sample in Pirahna (H_2SO_4:H_2O_2 = 1vol:1vol, 150 °C) for 15 min.
3. **Thoroughly** rinse the sample in flowing DI water for 1 min or more. Any residue H_2SO_4 will ruin the following spin-coating process. Blow dry with N_2.
4. Dehydrate the sample on a hot plate at 200 °C for 5 min.
5. Take the sample off the hot plate, quickly put it on a clean aluminum film and blow it cool with N_2. Immediately put the sample in the spinner and spin-coat HMDS at 2000 rpm for 1 min. The ramping-up is 1000 rpm/sec. The key to this step is to prime the surface native oxide before moisture in the air adsorbs on it.
6. Spin-coat diluted ZEP520A (ZEP520A:Anisole = 1vol:1vol) with the same process above. The diluted ZEP520A should be prepared at least 24 hours before spin-coating to ensure that thermal equilibrium is reached.
7. Wipe away any resist residue with a clean room towel. Use small amount of acetone if necessary. This will ensure that the sample will be well grounded in the EBL writing. This should also help to ensure the uniformity and repeatability of the dry etching process.

8. Bake the sample on a hot plate at 200 °C for 2.5 min.
9. Level the sample on the piece part holder as perfectly as possible. Ground it well.
10. Write the sample with Vistec EBPG 5000+ at 100 kV, with 300 μm aperture. The most critical features, such as the holes in the photonic crystal slab or the edges of the disk resonators, should be written with beam step size of 1 nm and resolution of 0.5 nm. For these critical features, in the Layout Beamer PEC module, the beam spot size should be 5 nm while all the other PEC settings should use the default. Accordingly, the beam current used should be less than 2 nA, so that the beam spot size is 5 nm. To save writing time, use bulk-and-sleeve method. The recommended dose for photonic crystal slab is 800 $\mu C/cm^2$. Together with the dry etching process below, this high dose with over expose the holes and enlarge them by 50 nm, but the shape of holes will be more circular and uniform. The changes in the sizes of the holes should be compensated in the GDS files or Layout Beamer.
11. Develop the sample at −15 °C for 30 sec in Amyl Acetate, immediately rinse it at −15 °C for 20 sec in MIBK and then immediately blow the sample dry with N_2 for at least 1 min. Begin the preparation of the developer and cold plate 2 hours in advance. Be sure to use cool grease between the cold plate and the aluminum tube holder to facilitate heat transfer.
12. Inspect the sample.
13. Measure the step height of the developed large features with P-16 surface profiler, or any features with AFM. The results should be about 160 nm, usually 158±3 nm.

14. On deep trench etcher, run the warm up process “warmup.bch” until the Step 6 in Cycle 13, if the etcher has not been used for 4 hours. Or just simply run it every time to ensure process repeatability. Use dedicated carrier wafer.
15. Season the deep trench etcher chamber for 3 min with the process “cnf-14-v.bch”. (Stop after 3 min in Step 5.) Use the same carrier wafer.
16. Put the sample directly on the same carrier wafer without any cool grease or photoresist. Stop after 65 sec in Step 5 of the process “cnf-14-v.bch”.
17. Measure the step height of the etched large features with P-16 surface profiler, or any features with AFM. The results should be about 305 nm, usually 307±8 nm.
18. Strip ZEP in Pirahna (H_2SO_4:H_2O_2 = 1vol:1vol, 150 °C) for 1 hr.
19. Measure the step height of the large features with P-16 surface profiler, or any features with AFM. The results should be about 230 nm, usually 230±5 nm.
20. Measure the critical feature sizes in SEM.

Appendix B. Photolithography and Wet Etching Processes

The photolithography and wet etching processes for releasing the silicon structures have been finalized and elaborated below. Minor adjustments are sometimes needed.

1. In most cases, this photolithography process follows immediately the ZEP removal, 1 hour Pirahna cleaning and thorough Di water rinsing at the end of the EBL and dry etching processes. Therefore the cleaning steps here before the dehydration bake can be skipped. Otherwise, follow the cleaning steps closely.
2. Clean the sample in ultrasonic acetone bath, if necessary.
3. Rinse the sample well with acetone, methanol, IPA and DI water.
4. Clean the sample in Pirahna (H_2SO_4:H_2O_2 = 1vol:1vol, 150 °C) for 15 min.
5. Thoroughly rinse the sample in flowing DI water for 1 min or more. Any residue H_2SO_4 will ruin the following spin-coating process. Blow dry with N_2.
6. Dehydrate the sample on a hot plate at 200 °C for 5 min.
7. Turn down the hotplate temperature to 120 °C without taking the sample off. Wait until the temperature reaches the set point. This will supposedly (but not sure) minimize water adsorption compared with moving the sample from a hotplate at 200 °C to another at 120 °C.
8. Use aluminum foil to make a small bowl with a diameter of about 2 cm, which should be enough to hold 5 drops of HMDS. Use another piece of aluminum foil to make a small roll about 5 cm long with a diameter of about 1 cm.

9. Put the aluminum roll vertically near the sample on top of the hotplate. Fill the aluminum bowl with about 5 drops of HMDS, quickly put it on top of the aluminum roll and immediately use a Pyrex glass beaker large enough to cover the sample, the bowl and the roll. This will allow the HMDS to vaporize gradually inside the beaker and prime the sample surface, which is at 120 °C. The aluminum roll is necessary in that it holds the HMDS liquid away from the hotplate surface to prevent violent boil. Wait for 3 min and then remove the beaker. This way of priming the sample is supposedly (but not sure) better than simply put the sample in saturated HMDS vapor at room temperature. If possible and necessary, a specially designed oven, such as YES, should be used to prime the sample.
10. Wait for another 1 min with the sample on top of the same hotplate at 120 °C.
11. Take the sample off the hotplate and put it inside another aluminum bowl, cover the sample surface with S1805 PR liquid.
12. Put the bowl with the sample covered by S1805 liquid under the bell jar of the desiccator in Chase 2. Turn on the pump and wait for the pressure difference to rise above 80 mBar. Wait for 2 min, then turn off the pump and vent the bell jar. This step is to make sure that the PR flows into and fill the holes of the PCSs to improve adhesion and help to prevent undesired HF solution penetration and undercut.
13. Mount the sample covered by liquid S1805 on the chuck of the spinner. Replenish S1805 on the sample surface and spin-coat at 3000 rpm for 30 sec, with a ramping rate of 3000 rpm/sec. It is important to replenish S1805 because the solvent in the liquid

S1805 on the sample surface has evaporated a lot during the desiccation, leaving the PR more concentrated than supposed to be.

14. Bake the sample at 115 °C for 1min.
15. Spin-coat S1813 at 3000 rpm for 30 sec, with a ramping rate of 3000 rpm/sec.
16. Bake the sample at 115 °C for 1min.
17. Expose the sample on the MA6 or MABA6 for 6~60 sec. The actual exposure time can be adjusted according to the specific needs for each sample.
18. Develop in MF-319 or CD-26 for 20~40 sec. The actual development time can be adjusted according to the specific needs for each sample.
19. Rinse the sample with flowing DI water briefly and gently blow dry.
20. Inspect the development results. If more development is needed, go back to the development step. If the alignment is off or some other tragic things have happened, rinse the PR off with acetone and start all over again from the very beginning. If everything is right, thoroughly rinse the sample in flowing DI water for 1 min or more. Gently blow dry with N_2.
21. Bake at 125 °C for 3 min.
22. Etch the sample in diluted HF solution for the time needed. Wear all the recommended protection gears in this step. The recommended dilution ratio is 1 volume of 49 % concentrated HF solution to 4 volumes of DI water, which etches the SiO_2 substrate at 62 nm/min at room temperature. If everything is done right, this etching rate should be quite accurately reproducible. The dilution should be done well in advance to make

sure that thermal equilibrium is reached. One day in advance should be enough for this purpose. The container should have very good chemical compatibility with HF acid and should be air-tight. The container should be stored inside the acid cabinet in the cleanroom to be maintained at a constant temperature. Right before etching, prepare two clean plastic beakers, fill them with DI water, label them as A and B respectively and put them right next to the plastic container that will be used for etching. Again, make sure that any container in this step has good chemical compatibility with HF acid. To minimize the exposure of tweezers to the HF, put the sample inside the container used for etching first, then pour in sufficient diluted HF. Start timing and cover the container to further prevent HF vapor inhalation.

23. When the time is nearly up, put on all the recommended protection gears, put the tweezers inside the etchant, hold the sample and wait. When time is up, gently take the sample out of the etchant and quickly transfer it to DI water beaker A. Dump the etchant into the drain of the Bay 3 wet bench and rinse the etchant container well. From here on, only eye protection is necessary. It is preferred that during the transfers between the containers, the devices on the sample are covered by a drop of water. However, often times this is very difficult to do because at this point the sample surface is covered by PR and is quite hydrophobic. It is OK if the surface seems no water coverage when taken out of the etchant or DI water, as long as the transfer is quick enough.
24. Gently move the sample around inside the DI water in beaker A to rinse off the HF as much as possible. Then quickly transfer the sample to DI water beaker B. Dump the DI

water in beaker A, rinse it well with Di water and fill it with DI water again. Repeat this transfer and rinse process three times or more, from B to A, then A to B, then B to A… The key point in this step is to gently and completely rinse away any residue HF.

25. Prepare two clean glass beakers, fill them with acetone and label them as A and B respectively. Gently and quickly transfer the sample from the DI water beaker to acetone beaker A. Gently move the sample around inside the acetone in beaker A to rinse off the DI water and PR as much as possible. Then quickly transfer the sample to acetone beaker B. Dump the acetone in beaker A, rinse it well with acetone and fill it with acetone again. Repeat this transfer and rinse process three times or more, from B to A, then A to B, then B to A… The key point in this step is to gently and completely rinse away any residue water and remove most of the PR.
26. Use the same transfer and rinse processes to transfer the sample from acetone into 1165 PR remover and rinse away residue acetone in glass beakers. One transfer from 1165 beaker A to B followed by another transfer from B to A should be enough.
27. Cover the 1165 beaker A and soak the sample in it for 1 hour or more. Higher temperature helps the removal but the actual temperature (not the set point of the hot plate) should not exceed 80 °C, otherwise the 1165 may be ignited. For long time heated soaking, it is very important to cover the beaker to prevent evaporation, otherwise the 1165 will run dry and the sample will be ruined.
28. Use the same transfer and rinse processes to transfer the sample from 1165 PR remover into IPA and rinse away any residue 1165 PR remover in glass beakers. A total of 4 or

more transfer and rinse processes should be done in this step. The residue of 1165 may be detrimental to the CPD process.

29. Lastly, use CPD to dry the sample. Follow the SOP of the CPD closely.